



# *Soliton Generation and Control in Engineered Materials*

Olga Borovkova

Supervisors: Prof. Lluis Torner,
Dr. Yaroslav Kartashov

ICFO – The Institute of Photonic Sciences
Universitat Politècnica de Catalunya

2013

# Abstract

Optical solitons provide unique opportunities for the control of light-by-light. Today, the field of soliton formation in natural materials is mature, as the main properties of the possible soliton states are well understood. In particular, optical solitons have been observed experimentally in a variety of materials and physical settings, including media with cubic, quadratic, photorefractive, saturable, nonlocal and thermal nonlinearities.

New opportunities for soliton generation, stability and control may become accessible in complex engineered, artificial materials, whose properties can be modified at will by, e.g., modulations of the material parameters or the application gain and absorption landscapes. In this way one may construct different types of linear and nonlinear optical lattices by transverse shallow modulations of the linear refractive index and the nonlinearity coefficient or complex amplifying structures in dissipative nonlinear media. **The exploration of the existence, stability and dynamical properties of conservative and dissipative solitons in settings with spatially inhomogeneous linear refractive index, nonlinearity, gain or absorption, is the subject of this PhD Thesis.**

We address stable conservative fundamental and multipole solitons in complex engineered materials with an inhomogeneous linear refractive index and nonlinearity. We show that stable two-dimensional solitons may exist in nonlinear lattices with transversally alternating domains with cubic and saturable nonlinearities. We consider multicomponent solitons in engineered materials, where one field component feels the modulation of the refractive index or nonlinearity while the other component propagates as in a uniform nonlinear medium. We study whether the cross-phase-modulation between two components allows the stabilization of the whole soliton state.

Media with defocusing nonlinearity growing rapidly from the center to the periphery is another example of a complex engineered material. We study such systems and, in contrast to the common belief, we have found that stable bright solitons do exist when defocusing nonlinearity grows towards the periphery rapidly enough. We consider different nonlinearity landscapes and analyze the types of soliton solution available in each case.

Nonlinear materials with complex spatial distributions of gain and losses also provide important opportunities for the generation of stable one- and multidimensional fundamental, multipole, and vortex solitons. We study one-dimensional solitons in focusing and defocusing nonlinear dissipative materials with single- and double-well absorption landscapes. In two-dimensional geometries, stable vortex solitons and complexes of vortices could be observed. We not only address stationary vortex structures, but also steadily rotating vortex

solitons with azimuthally modulated intensity distributions in radially symmetric gain landscapes.

Finally, we study the possibility of forming stable topological light bullets in focusing nonlinear media with inhomogeneous gain landscapes and uniform two-photon absorption.

# Thesis publications


1. O.V. Borovkova, V.E. Lobanov, Y.V. Kartashov, and L. Torner, “Stable vortex-soliton tori with multiple nested phase singularities in dissipative media,” Phys. Rev. A **85**, 023814 (2012).

2. O.V. Borovkova, Y.V. Kartashov, V.A. Vysloukh, V.E. Lobanov, B.A. Malomed, and L. Torner, “Solitons supported by spatially inhomogeneous nonlinear losses,” Opt. Express **20**, 2657-2667 (2012).

3. V.E. Lobanov, O.V. Borovkova, Y.V. Kartashov, V.A. Vysloukh, and L. Torner, “Topological light bullets supported by spatiotemporal gain,” Phys. Rev. A **85**, 023804 (2012).

4. V.E. Lobanov, O.V. Borovkova, Y.V. Kartashov, B.A. Malomed, and L. Torner “Stable bright and vortex solitons in photonic crystal fibers with inhomogeneous defocusing nonlinearity,” Opt. Lett. **37**, 1799-1801 (2012).

5. O.V. Borovkova, V.E. Lobanov, and B.A. Malomed, “Stable nonlinear amplification of solitons without gain saturation,” Europhys. Lett. **97**, 44003 (2012).

6. O.V. Borovkova, Y.V. Kartashov, V.E. Lobanov, V.A. Vysloukh, and L. Torner, “Vortex twins and anti-twins supported by multiring gain landscapes,” Opt. Lett. **36**, 3783-3785 (2011).

7. O.V. Borovkova, Y.V. Kartashov, L. Torner, and B.A. Malomed, “Bright solitons from defocusing nonlinearities,” Phys. Rev. E **84**, 035602 (2011).

8. O.V. Borovkova, Y.V. Kartashov, B.A. Malomed, and L. Torner, “Algebraic bright and vortex solitons in defocusing media,” Opt. Lett. **36**, 3088-3090 (2011).

9. O.V. Borovkova, Y.V. Kartashov, V.E. Lobanov, V.A. Vysloukh, and L. Torner, “General quasi-nonspreading linear three-dimensional wave packets,” Opt. Lett. **36**, 2176-2178 (2011).

10. O.V. Borovkova, V.E. Lobanov, Y.V. Kartashov, and L. Torner, “Rotating vortex solitons supported by localized gain,” Opt. Lett. **36**, 1936-1938 (2011).

11. O.V. Borovkova, B.A. Malomed, and Y.V. Kartashov, “Two-dimensional vector solitons stabilized by a linear or nonlinear lattice acting in one component” Europhys. Lett. **92**, 64001 (2010).

12. O.V. Borovkova, Y.V. Kartashov, and L. Torner, “Stabilization of two-dimensional solitons in cubic-saturable nonlinear lattices,” Phys. Rev. A **81**, 063806 (2010).

# Acknowledgements

First of all, I would like to express my deep gratitude to my PhD supervisor Prof. Lluis Torner for an opportunity to work at such excellent scientific center, for inspiring and guiding me, for the attention and academic support.

I would like to appreciate greatly my co-supervisor Dr. Yaroslav Kartashov, who taught me a lot, for his ability to explain everything with ease and clarity, for interesting topics he proposed, for his patience and immutable encouragement.

I also would like to thank Dr. Valery Lobanov, Prof. Boris Malomed and Prof. Victor Vysloukh for the professional help, advises, fruitful discussions, and valuable comments.

I acknowledge financial support from ICFO, as well as the scholarship from the Spanish Ministry of Education.

I am grateful to Prof. David Artigas, Laia Miralles i Puig, Manuela Furkert, Anna Gstöttner, Mery Gil, Christina Garcia, who helped me with various official issues.

I would like to thank my colleagues I have met at ICFO, Dr. Osamy Takayama, Taisuke Minagawa, Federica Beduini, Jan Gieseler, Marina Mariano Juste, Rafael Betancur, and Parisa Farzam for their friendship and support.

My work would not have been possible without love, understanding, and support of my family, and especially of my daughter Sofia.

# Table of contents

# Chapter 1. Introduction

### *1.1. Historical Background*

Nonlinearity is an inherent feature of many materials. In optics it may dramatically affect the propagation of light at high input intensities. It engenders a variety of interesting effects related to the generation, properties and propagation dynamics of light in suitable media. One of the most intriguing phenomena that is connected with wave propagation in a nonlinear medium is the *formation of optical soliton*. Namely, a solitary wave that preserves its shape in the course of propagation, even under the effect of reasonable perturbations.

The first known record of solitons in scientific literature goes back to the observations of John Scott Russell on wave propagation in a Scottish channel, published in 1844 [1]: *"I was observing the motion of a boat which was rapidly drawn along a narrow channel by a pair of horses, when the boat suddenly stopped – not so the mass of water in the channel which it had put in motion; it accumulated round the prow of the vessel in a state of violent agitation, then suddenly leaving it behind, rolled forward of a large solitary elevation, a rounded, smooth and well-defined heap of water, which continued its course along the channel apparently without change of the form or diminution of speed. I followed it on horse-back, and overtook it still rolling on at a rate of some eight or nine miles an hour, preserving its original figure some thirty feet long and a foot to a foot and a half in height. Its height gradually diminished, and after a chase of one or two miles I lost it in the windings of the channel. Such, in the month of August 1834, was my first chance interview with that singular and beautiful phenomenon which I have called the Wave of Translation…".*

The next important step in the development of soliton theory was the work of D.J. Korteweg (1848–1941) and G. de Vries (1866–1934) published in 1895 [2]. They derived an equation governing the propagation of waves in wide

channels with an invariable cross-section, i.e. the so-called Korteweg-de Vries equation. The solution to this equation was the solitary wave revealed earlier by J.S. Russell. The term 'soliton' was coined in 1965 in the paper of N.J. Zabusky and M.D. Kruskal [3], in which the particle-like behavior of solitons upon their interaction was pointed out. Besides, the papers stresses that the absence of secondary waves in the course of propagation shows that the soliton energy is localized in space and/or time, again indicating the particle-like nature of solitons.

The key ability of solitons to preserve their form in the course of propagation could be explained by the simultaneous action of two opposite processes. On the one hand, the amplitude of a wave packet propagating in a nonlinear medium tends to increase in the area in which the nonlinear contribution to the refractive index is higher, i.e. in the case of focusing medium in the domain with the larger field intensity. On the other hand, in dispersive media different parts of the wave packet move with different velocities and, therefore, the wave packet spreads (a similar spreading is caused by diffraction in the spatial domain). Under appropriate conditions, the spreading due to dispersion or diffraction can be compensated by nonlinearity and thus the wave packet shape may remain unchanged during the course of propagation.

Over the years, the concept of soliton formation has found applications in many different areas of physics and technology, including optics, plasma physics, biology, chemistry and applied mathematics, to name just a few [4–7]. In nonlinear optics solitons attracted attention because the invariance of the pulse shape is an important feature in long-distance data transmission, where solitons may play the role of information bits. Another potential application of optical solitons is related to the possibility of controlling light-by-light, and on all-optical routing and switching or beam shaping and steering.

In the Thesis we address solitons in cubic nonlinear media, thus from now on we focus on such cases. Note, however, that solitons have also been studied in great detail in quadratic, thermal and photorefractive media.

### *1.2. Mathematical Model of Nonlinearity and Beam Propagation in Nonlinear Media*

Solitons may exist thanks to the fact that the response of a medium to an applied optical field may be nonlinear [8]. The electric field $\vec{E}\left(\vec{r},t\right)$ associated with an optical wave propagating in a rather general medium obeys the following wave equation:

$$\nabla^2\vec{E}-\frac{1}{c^2}\frac{\partial^2\vec{E}}{\partial t^2}=\frac{1}{\varepsilon_0 c^2}\frac{\partial^2\vec{P}}{\partial t^2}, \qquad (1.1)$$

where $c$ is the speed of light in a vacuum, $\varepsilon_0$ is the permittivity of a vacuum, and $\vec{P}\left(\vec{r},t\right)$ is the polarization field. The dependence of the polarization field on the strength of the applied field $\vec{E}\left(\vec{r},t\right)$ can be written as

$$\vec{P}\left(\vec{r},t\right)=\varepsilon_0\chi^{(1)}\vec{E}\left(\vec{r},t\right)+\varepsilon_0\chi^{(2)}\vec{E}^2\left(\vec{r},t\right)+\varepsilon_0\chi^{(3)}\vec{E}^3\left(\vec{r},t\right)+\ldots, \qquad (1.2)$$

where and $\chi^{(1)},\chi^{(2)},\chi^{(3)}$ are the susceptibilities of the first, second and third orders, respectively.

Linear optics limits itself to the first term in Eq. (1.2). The second term describes the second-order nonlinear interactions, and it is nonzero in noncentrosymmetric crystals (that do not display inversion symmetry). Liquids, gases, glasses, and even some crystals display inversion symmetry, and thus the $\chi^{(2)}$ susceptibility vanishes in such materials and the second term in Eq. (1.2) can be omitted. The third-order nonlinear response is the most common, and it appears in both centrosymmetric and noncentrosymmetric media. In the simplest situation the refractive index of a local conservative centrosymmetric material may be written in the following form:

$$n=n_0+n_{nl}\left(I\right), \qquad (1.3)$$

where $n_0$ is the linear refractive index, $n_{nl}$ is the nonlinear part of the refractive index, and $I$ is the intensity of the wave.

A medium in which third-order nonlinearity prevails over all other types of nonlinearity is called *cubic*. There the nonlinear contribution to the refractive index can be represented as

$$n=n_0+n_2I, \qquad (1.4)$$

where $n_2$ is the nonlinear refractive index. It is one of the most abundant and well-studied nonlinearities. If $n_2$ is positive, the material effectively acts as a positive lens, which causes the rays to curve towards each other, and leads to the focusing of the light beam. Liquid $CS_2$, and waveguides made of silicate glass are examples of focusing Kerr media. If the nonlinear refractive index is negative, the material behaves as a negative lens and disperses incident light. Therefore it is a defocusing Kerr medium. Sodium vapor could be a focusing or defocusing medium depending on the frequency of the propagating light exceeding 589 nm [9].

As the intensity of the light beam increases the nonlinearity may saturate and at such intensities it is necessary to introduce another model for the adequate description of light propagation – a model with *saturable* nonlinearity. Saturable materials are also well-known and widely used in nonlinear optics. The effect of

nonlinearity saturation was observed in various media, for instance in semiconductor-doped glass. The dependence of the refractive index on light intensity in saturable media may be rather complex, but here we will use the simplest model (it was mentioned in particular upon the analysis of the response of two-level systems [10, 11]):

$$n = \frac{n_0}{1 + I/I_s}, \tag{1.5}$$

where $I_s$ is the saturation intensity. Photorefractive materials may also be described as saturable under suitable conditions.

Until now we have used physical values in the equations, but in the numerical modeling in the Thesis we will employ dimensionless equations. The procedures for the transition from physical equations to dimensionless ones are well-known. As an example we give the simple equation describing the propagation of the optical beam in a focusing Kerr medium.

The spatiotemporal paraxial wave equation for the envelope of the optical beam has the form

$$2ik\left(\frac{\partial E}{\partial z} + \frac{1}{\mathrm{v}_g}\frac{\partial E}{\partial t}\right) + \frac{\partial^2 E}{\partial x^2} + \frac{\partial^2 E}{\partial y^2} - k\frac{\partial^2 k}{\partial \omega^2}\frac{\partial^2 E}{\partial t^2} + 2k^2\frac{n_2}{n_0}\left|E\right|^2 E = 0, \tag{1.6}$$

where the refractive index is given by Eq. (1.4), $\mathrm{v}_g$ is the group velocity, an $\omega$ and $k$ are the frequency and wave vector, respectively. Using the substitutions $\tau = \left(t - z/\mathrm{v}_g\right)\sqrt{k/D}$, $D = -\partial^2 k/\partial\omega^2$, $\left(\zeta,\eta,\xi\right) = k\times\left(x,y,z\right)$, $q = \sqrt{n_2/n_0}E$, Eq. (1.6) becomes:

$$i\frac{\partial q}{\partial \xi} = -\frac{1}{2}\left(\frac{\partial^2 q}{\partial \zeta^2} + \frac{\partial^2 q}{\partial \eta^2} + \frac{\partial^2 q}{\partial \tau^2}\right) - \left|q\right|^2 q, \tag{1.7}$$

This is the normalized dimensionless Schrödinger equation. We will use several versions of this equation.

### *1.3. Soliton Diversity*

Optical solitons can be *temporal, spatial*, and *spatiotemporal,* depending on whether the confinement of light takes place in time, space, or in both space and time during wave propagation [4, 12–15]. Temporal solitons are optical pulses that maintain their temporal shape, and spatial solitons represent self-trapped beams that remain confined in the transverse direction, orthogonal to the direction of propagation. As was mentioned above, in temporal cases solitons form because self-phase modulation compensates for the natural dispersion-induced broadening of an optical pulse, whereas spatial solitons exist due to the balance

between spatial self-focusing and diffraction-induced spreading. In Fig. 1.1 it is shown how the beam profile and phase front change under the independent impact of self-focusing and diffraction, and under their simultaneous influence. The simplest spatial solitons in focusing media have a bell-shaped profile. In contrast, if the nonlinear refractive index of the medium is negative, dark or grey solitons may form which represent localized 'holes' in the extended background.

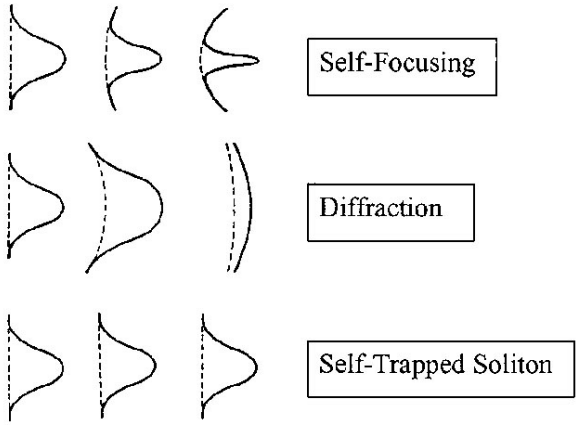


Figure 1.1. Schematic showing spatial beam profiles (solid line) and phase fronts (dashed line) for (a) beam self-focusing, (b) normal beam diffraction, and (c) soliton propagation [12].

Spatiotemporal optical solitons are pulses localized in all transverse directions in space, as well as in time. These optical structures are often called light bullets. Spatiotemporal optical solitons become conceivable when nonlinear self-action simultaneously compensates diffraction and group velocity dispersion of the localized wave packet. Figure 1.2 illustrates the formation of a light bullet.

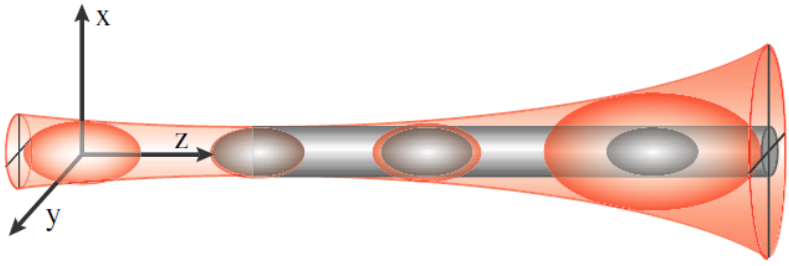


Figure 1.2. Formation of a spatiotemporal soliton due to the simultaneous balance of diffraction and dispersion by nonlinear self-focusing [14].

The fundamental soliton shown in Fig. 1.1 has the simplest structure – its intensity profile is bell-shaped. More complex *multipole solitons* have several intensity peaks and in many cases they can be considered as specific nonlinear

combinations of several fundamental solitons with alternating phases (Fig. 1.3 shows the typical profile and phase distribution of a two-dimensional dipole soliton). Scalar multipole solitons do not exist in local Kerr media because the $\pi$ phase difference between the humps forming the multipole state causes their repulsion.

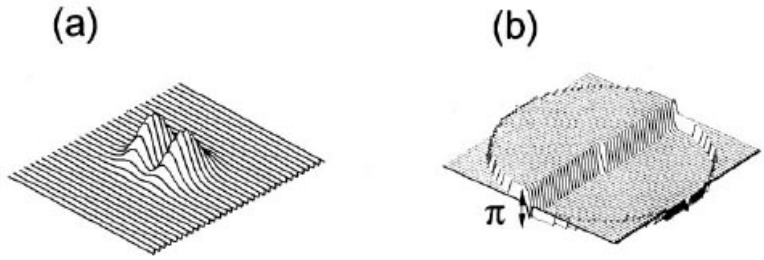


Figure 1.3. (a) Intensity and (b) phase distributions of two-dimensional dipole mode [16].

Another fascinating example of an optical soliton that will often be discussed in this Thesis is the vortex soliton – a self-sustained beam carrying a nonzero angular momentum via topological phase singularities nested in the beam [17]. In uniform local media vortex solitons exhibit ring-like intensity distributions with a phase singularity in the center (Fig. 1.4).

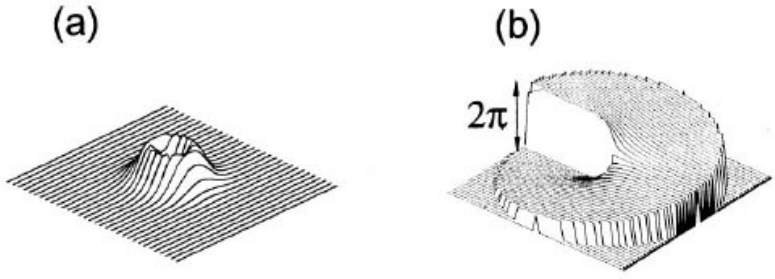


Figure 1.4. (a) Intensity and (b) phase distributions of two-dimensional vortex soliton [17].

Several light beams can be mutually coupled due to nonlinearity and form *multicomponent or vector* solitons. The simplest vector solitons include two components (optical beams with different polarizations or carrier wavelengths) that feel each other due to cross-phase-modulation. The study of such solitons was motivated by Manakov's related discovery [18]. As opposed to scalar solitons that can be considered the fundamental mode of the waveguide that they induce, vector solitons contain higher-order modes of the corresponding waveguide.

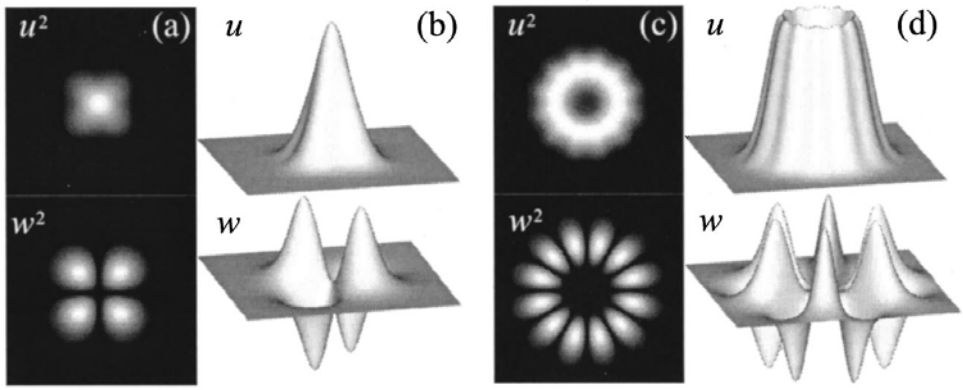


Figure 1.5. Examples of two-component vector solitons, (a, b) intensity and envelope of first and second components of a quadrupole, and (c, d) intensity and envelope of first and second components of a dodecagon multipole [16].

Vector solitons may form due to the mutual coupling of fundamental and multipole components. In general, vector solitons can include an arbitrary number of interacting components (two examples of vector solitons are presented in Fig. 1.5).

### *1.4. Solitons in Conservative Homogeneous Media*

Mathematically, the evolution of the dimensionless amplitude $q\left(\zeta,\eta,\xi,\tau\right)$ of a wave packet propagating in a conservative homogeneous nonlinear medium can be described by the nonlinear Schrödinger equation, which can be derived from the wave equation (1.1) and that in its most general form reads as:

$$i\frac{\partial q}{\partial \xi}=-\frac{\nu}{2}\left(\frac{\partial^2 q}{\partial \eta^2}+\frac{\partial^2 q}{\partial \zeta^2}\right)-\frac{\beta}{2}\frac{\partial^2 q}{\partial \tau^2}+\Sigma\left(q\right), \qquad (1.8)$$

Here we took into account the diffraction of the beam described by the first term enclosed in brackets on the right-hand side of Eq. (1.8), group-velocity dispersion described by the second term, and the nonlinearity of the medium described by function $\Sigma(q)$, which accounts for the specific type of nonlinear response of the material [for example, in cubic medium $\Sigma=\pm q\left|q\right|^2$, see Eq. (1.7)]. In Eq. (1.8) $\zeta,\eta$ are dimensionless transverse coordinates, $\xi$ is the longitudinal coordinate, and $\tau$ is the normalized running time.

Temporal solitons, whose evolution is governed by Eq. (1.6) with $\nu=0$, were the first optical solitons observed experimentally. They were predicted theoretically in optical fibers in 1973 [19], and were observed experimentally in 1980 [20]. Many attempts to use solitons in transmission systems were quickly

undertaken. Hasegawa suggested an idea for an all-optical transmission system in which attenuation was compensated by Raman gain [21]. This effect was demonstrated in experiments in 1985 and 1988 by Mollenauer and co-authors [22, 23]. In the 1990s, dispersion-managed temporal solitons in fibers with alternating in propagation direction dispersion and nonlinearity drew considerable attention. The first 3000 km long commercial fiber telecommunication link, whose operation was based on dispersion-managed solitons, was introduced in Australia in 2002.

Spatial solitons, whose formation is described by Eq. (1.8) with $\beta = 0$, have been studied in various media and systems. The idea that an optical beam can change the refractive index of the medium and thereby induce a waveguide emerged in 1962 [24]. Light propagation governed by Eq. (1.8) in media with third-order nonlinearity was analyzed in both one and two transverse dimensions [25–27]. It was shown that in a cubic nonlinear medium, the two-dimensional self-sustained solutions of Eq. (1.8) experience catastrophic collapse and, thus, they are unstable [27, see also for an extended review 28]. Quasi-one-dimensional solitons in bulk nonlinear medium with third-order nonlinearity were also found to be unstable with respect to modulations in one transverse direction, leading to a breakup in the multiple filaments [29]. To stabilize spatial solitons it was necessary to arrest the diffraction in one transverse direction, for example by means of a slab waveguide. A landmark experiment on diffraction-arrested light propagation was reported in 1974 [9], using a cell filled with sodium vapor. Later, one-dimensional bright solitons were generated in glass, semiconductors, polymers, etc.

It was demonstrated in a number of works that the medium with saturable nonlinearity stabilizes two-dimensional fundamental solitons against collapse [30–32]. At the same time, higher-order solitons possessing nodes in a radial direction remain unstable, even in saturable medium, and break into several fundamental solitons under the action of azimuthal instabilities [33, 34]. Two-dimensional settings allow the observation of vortex solitons. Such solitons exhibit ring-like profiles, and in most conservative local uniform materials (including saturable media) they are prone to azimuthal modulation instabilities. Such instabilities may be eliminated in materials with competing nonlinearities [35], in nonlocal materials [36], or in the presence of optical lattices as will be discussed below.

The experimental observation of spatial vector solitons was reported in 1996 [37]. Two years later the concept of vector solitons was extended to two transverse dimensions [38]. The mutual interaction of several field components forming vector solitons significantly affects their stability [39–41].

Spatiotemporal solitons in cubic nonlinear media were addressed by Silberberg [42] in a seminal paper on the spatiotemporal compression of optical pulses. Spatiotemporal self-focusing was observed in planar waveguides with Kerr nonlinearity [43]. The simultaneous contraction of the pulses in space and time was only achieved in the anomalous dispersion regime, while in the normal and zero dispersion regimes pulses always exhibited broadening in time. Several

methods were proposed to arrest the collapse of spatiotemporal solitons, that included nonlinearity saturation [44], nonlocality of the nonlinear response [45], non-paraxiality and high-order dispersion [46, 47], as well as wave rectification [48]. Minardi et al [49] reported the first experimental observation on the transient formation of a nonlinear light bullet in a two-dimensional array of coupled waveguides. Despite all these achievements and the fact that to date light bullets have been predicted to exist in various nonlinear materials, stable long-lived light bullets have not yet been experimentally observed.

### *1.5. Solitons in Dissipative Homogeneous and Inhomogeneous Media*

While in conservative settings solitons exist due to the balance between dispersion, diffraction, and nonlinearity, in nonconservative media the formation of stationary soliton solutions also requires an exact balance between gains and losses. The propagation of light in such media can be described by the variant of the nonlinear Schrödinger equation, which is frequently termed the Ginzburg-Landau equation:

$$i\frac{\partial q}{\partial \xi} = -\frac{1}{2}\left(\frac{\partial^2 q}{\partial \eta^2} + \frac{\partial^2 q}{\partial \zeta^2}\right) - \frac{\beta}{2}\frac{\partial^2 q}{\partial \tau^2} + \Sigma\left(q\right) + iP\left(q\right) - i\Gamma\left(q\right), \qquad (1.9)$$

where term $P\left(q\right)$ describes the amplification, and term $\Gamma\left(q\right)$ is responsible for the losses (that can be linear and nonlinear). Within the framework of this model, solitary wave solutions can also be found in the form of so-called *dissipative* solitons [7, 50]. Figure 1.6 illustrates the complex formation of a dissipative soliton by the balance of all the effects at play.

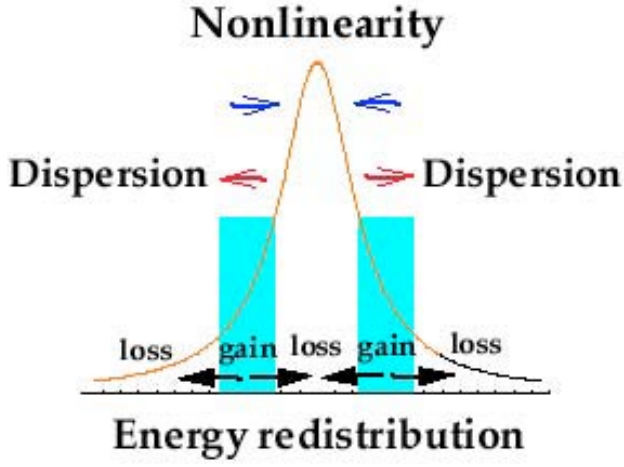


Figure 1.6. Qualitative description of the simultaneous action of nonlinearity and dispersion, amplification and absorption in dissipative solitons [7].

The simplest one-dimensional complex Ginzburg-Landau equation admits well-known exact analytical solutions [51], although all of them were shown to be unstable. The competition between linear losses, cubic gain, and quintic losses in the complex Ginzburg-Landau equation can stabilize dissipative solitons in 1D [52, 53] and 2D settings [54–56]. Stable dissipative light bullets were predicted in laser systems with saturable gain and absorption [57, 58]. Besides, stable fundamental light bullets [59–62] and three-dimensional vortex bullets [63–65] also exist in uniform dissipative systems governed by the complex cubic-quintic Ginzburg-Landau equation.

Experimental observation of dissipative solitons was reported, for example, in semiconductor microcavities [66], and electrically-pumped semiconductor amplifiers [67]. Another possible way to stabilize dissipative solitons is the application of various schemes with spatially-inhomogeneous linear gain [68–75], including dual-core couplers with linear gain and losses acting on different cores [68, 69], or systems with one or several amplifying channels created in a medium with nonlinear absorption [71–74]. Physically, such localized gains can be achieved using an appropriate profile of the concentration of gain-inducing dopants in the medium, or illuminating a uniformly doped waveguide by a properly focused pump beam. In such media stable dissipative solitons may be supported by the balance between the localized amplification and uniform nonlinear dissipation. In models with gain landscapes of finite width, various soliton solutions were found in numerical form [71–74], including fundamental and two-dimensional vortex solitons supported by ring-like gain profiles [75]. Vortex solitons may also exist and experience considerable dynamical shape deformations in laser amplifiers [76]. Models incorporating localized gain were introduced for solitons in lasing media [77] and materials with periodic refractive index modulations [78, 79].

### *1.6. Solitons in Microstructured Materials*

The properties of solitons in uniform nonlinear materials are reasonably well studied. In such media the possibilities for soliton stabilization and control are determined exclusively by the character of the nonlinear response. However, modern microstructured materials provide new opportunities for the generation and manipulation of novel types of solitons. Photonic crystals or photonic crystal fibers, various linear and nonlinear photonic lattices, and metamaterials are examples of microstructured materials with complex linear and nonlinear refractive index landscapes.

Photonic crystals are structures with deep periodic modulation of dielectric constants [80–83]. Optical properties of photonic crystals may depart considerably from the optical properties of uniform media. Due to the periodicity of the material the dynamics of the propagation of the electromagnetic wave in photonic crystal resembles the electron motion inside the usual crystal. The main

feature of the photonic crystals is the existence of photonic band gaps. The light with the wavelength from the band gap cannot travel through the crystal. If one introduces a defect into a perfectly periodic photonic crystal, the localized mode may appear in the band gap of the photonic crystal. In photonic crystal fibers the light is concentrated on a set of coupled defects that may support localized modes with the wavelength inside the band gap [84]. In contrast to usual optical fibers, where light localization is achieved due to total internal reflection, photonic crystal fibers can be strongly curved and allow changes to the trajectory of light propagation on very small spatial scales, which is of great importance for practical applications. Another aspect that is of thechnological significance is the reconfigurability of the transmission spectrum of the photonic crystal fibers [85, 86].

In contrast to photonic crystals or photonic crystal fibers, in photonic lattices the modulation of refractive index is shallow, which nevertheless even broadens the opportunities for the control of the flow of light because in such media the nonlinear contribution to the refractive index can be of the order of the depth of the linear refractive index modulation. The refractive index of the optical lattice is usually modulated (a typical modulation depth is about $10^{-3}$) in the plane orthogonal to the direction of the light beam propagation [87–92]. Linear lattices can be created in fused silica by the direct writing with powerful laser beams [93, 94] (see Fig. 1.7), or by non-uniform in-diffusion of dopants into the surface of an otherwise uniform material, such as doped photorefractive $LiNbO_3$ [95] crystal. Lattices can also be etched on the surface of semiconductor materials [96].

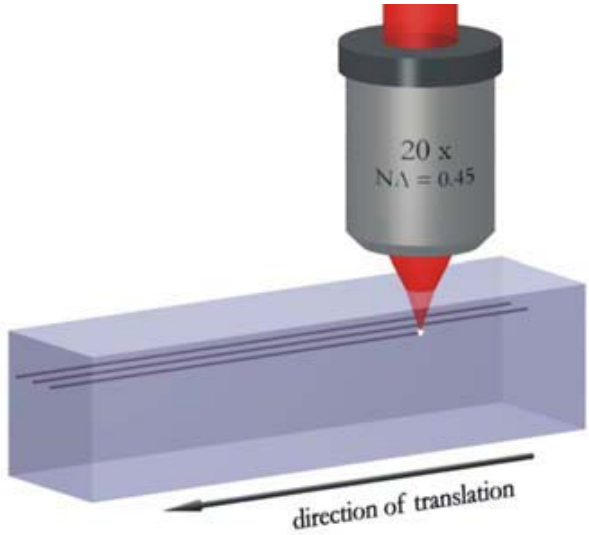


Figure 1.7. Scheme of writing process in transparent bulk material using femtosecond laser pulses [94].

A powerful and flexible technique to create linear lattices is so-called optical induction [88, 97, 98], in which the lattice is created by the interference of multiple plane waves in suitable material (usually it is a photorefractive crystal), launched at an angle with respect to the sample axis (Fig. 1.8). The technique of optical induction allows the creation of optical lattices featuring unusual symmetries reflecting the intensity distributions of the corresponding nondiffracting light patterns that are used for lattice induction.

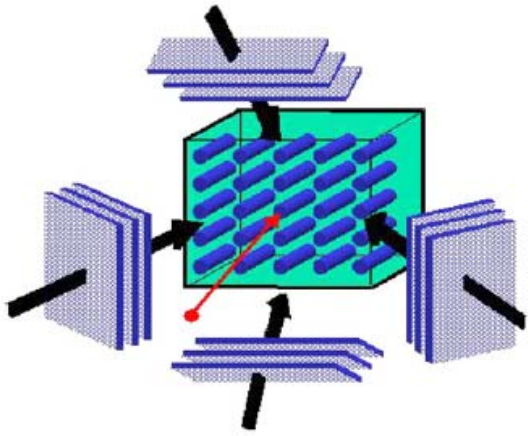

Figure 1.8. Four interfering beams forming an optical lattice structure [91].

In linear lattices, under appropriate conditions, the transverse modulation of refractive index, diffraction, and nonlinearity may compete on a similar footing, resulting in the formation of soliton states whose shapes are strongly modulated and usually reflect the symmetry of the corresponding refractive index landscapes. Among the various types of optical lattices, those ones with periodic refractive index modulation have attracted considerable attention. Periodic transverse refractive index modulation is known to play a strong stabilizing action in two- and three-dimensional solitons [91, 92]. Such lattices may not only support fundamental two-dimensional solitons, but also more complex states like vortex or multipole lattice solitons [88, 99–105]. The symmetry and intensity distributions of such states strongly depend on the structure of the refractive index landscape.

Linear lattices enable the observation of all-optical switching and routing of spatial solitons. Unlike in a uniform medium where the soliton can travel in the transverse direction whilst retaining its initial shape and propagation angle, a soliton travelling across the linear lattice slowly radiates and may be trapped inside one of the lattice channels. Thus the output soliton's position can be effectively controlled by variations in the incidence angle and lattice parameters. Fig. 1.9 shows how in two-dimensional linear lattices (or two-dimensional waveguide networks) solitons can be effectively routed or blocked when interactions with additional solitons are utilized.

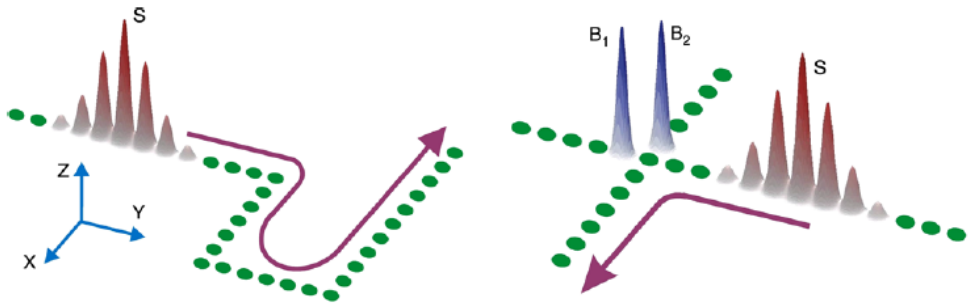


Figure 1.9. Navigating a discrete soliton through bends (left panel) and array junctions (right panel), "S" denotes moving soliton beam, while "$B_1$" and "$B_2$" denote immobile "blocking" solitons [91].

Another interesting type of optical lattice is the nonlinear lattice – a structure with a spatially inhomogeneous nonlinearity, rather than refractive index. Such lattices can be fabricated by using suitable combinations of different materials. The main qualitative difference between linear and nonlinear lattices is that the nonlinear lattice is in fact self-induced and vanishes when the intensity of the laser beam becomes small, while the linear lattice affects the propagation of even low-power laser beams. The properties of one-dimensional solitons in nonlinear lattices are particularly intriguing [106-115] and they may depart considerably from the properties of solitons in conventional linear lattices. The dynamics of soliton formation in one- and two-dimensional nonlinear lattices is the subject of intense investigations. In particular, it was already shown that while smooth variations of the cubic nonlinearity in the transverse plane may stabilize two-dimensional solitons only in a very limited parameter range [107], structures with sharp step-like variations in cubic nonlinearity do support stable two-dimensional solitons in wide range of parameters as it was predicted in Ref. [116], where stable radially symmetric solitons were obtained inside a nonlinear circle or annular ring embedded in a linear medium. More recently, the stability of two-dimensional solitons was demonstrated in a truly periodic nonlinear lattice in the form of an array of nonlinear circles [113].

Even more exotic properties may be observed for solitons in mixed lattices with the simultaneous transverse modulation of the linear refractive index and nonlinearity coefficient. It should be stressed that the current technological state-of-art already allows the relatively deep simultaneous modulation of the linear refractive index and the nonlinearity coefficient of the material. Thus, one can readily fabricate optical lattices with out-of-phase modulations of the refractive index and nonlinearity. Mixed lattices were demonstrated in photonic crystal fibers, where the refractive index and nonlinearity coefficient jumped between the material and the voids filled with air or distinct substances [117, 118]. The competition between refractive index modulation and nonlinearity in mixed

lattices results in new soliton properties, such as power-dependent shape transformations and mobility enhancement [111, 112, 119, 120].

As mentioned above, photonic lattices allow new types of soliton to be generated that do not exist in uniform media. For instance, one way to generate bright self-sustained modes in media with defocusing nonlinearity is to employ periodic linear potentials [91, 92, 121] or the modulation of nonlinearity [90, 115, 122]. Thus the periodic transverse modulation of the refractive index affects the strength and sign of the effective diffraction for the propagating waves and results in bright soliton formation, even in defocusing medium. A defocusing nonlinearity landscape with a minimum in one point combined with a linear trapping potential was used to create bright solitons in defocusing media [123]. Note that the nonlinearity or linear refractive index of the material may be modulated (sometimes deeply), not only in the transverse plane but also in the direction of light propagation. In this case one deals with nonlinearity or refractive index management [90, 124, 125], a technique that also permits the stabilization of multidimensional solitons.

Materials whose properties and parameters are modulated in the transverse plane or in the direction of light propagation may be termed “engineered materials”. They may include various modulations of the linear refractive index, magnitude and sign of the nonlinearity, gain, or linear and nonlinear absorption.

### *1.7. Overview of the Thesis*

In this Thesis we address optical solitons in several engineered materials. We study their generation, properties and stability.

In Chapter 2 the stabilization of scalar and multicomponent solitons in engineered materials with linear and nonlinear lattices is addressed. The first section refers to scalar one- and two-dimensional solitons in the medium composed from transversally alternating domains with cubic (Kerr) and saturable nonlinearities. It is shown that solitons with the center in the Kerr domain could be stable, even in the two-dimensional case where they are usually unstable. In contrast, solitons centered on saturable domains are strongly unstable in both one- and two-dimensional cases. The second section of this chapter is devoted to the stabilization of vector solitons due to the linear or nonlinear lattice acting on only one of field components. The cross-phase-modulation between field components experiencing the modulation of the refractive index/nonlinearity and propagating in effectively uniform medium results in the stabilization of the entire soliton complex.

In Chapter 3 it is shown that bright solitons can even exist in purely defocusing medium without the help of a linear potential, which earlier was commonly considered impossible. The first section deals with the engineered

material with nonlinearity increasing exponentially from the center to the periphery. This medium supports both fundamental and higher-order modes of one and two dimensions and also vortex rings. Solitons in power-law defocusing nonlinearity landscapes are considered in the second section. In this case, fundamental and vortex solitons are found in one and two dimensions, respectively. The third section describes stable bright and vortex solitons in hexagonal photonic crystal fiber where the core material is linear or focusing, while voids are filled with a defocusing material whose nonlinearity grows towards the photonic crystal periphery.

Chapters 4, 5 and 6 propose the concept that focusing and defocusing media with inhomogeneous gain and absorption landscapes can support diverse stable solitons in one-, two-, and three-dimensional geometries.

In Chapter 4, stable fundamental and multipole one-dimensional solitons in both focusing and defocusing nonlinear dissipative materials with inhomogeneous gain are considered. Solitons in single-well and double-well absorption landscapes and their bifurcations are discussed in the first section. The second section is devoted to solitons and their properties in the medium with cubic-quintic nonlinearity, linear loss, and localized cubic gain.

Chapter 5 addresses vortex solitons in focusing cubic nonlinear media with two-photon uniform absorption and various gain landscapes – ring-like, elliptic or composed from several amplifying rings. It is shown that a single amplifying ring supports rotating vortex solitons with multiple phase singularities nested in a common vortex core. In this setting the vortex states are asymmetric, despite the fact that all parameters in the system are radially symmetric or uniform. The second section considers the modification of the vortex solitons upon stretching of the gain ring along one transverse direction. The initial vortex with one charge-m dislocation transforms in such a structure into a complex state with m separated single-charge dislocations. We show that families of multivortex solitons in gain landscapes composed of several amplifying rings may be stable. Symmetric and asymmetric vortex twins and anti-twins are addressed.

In Chapter 6, stable three-dimensional spatiotemporal fundamental and vortex solitons supported by localized spatiotemporal gain landscapes are presented. The collapse and azimuthal modulation instability that usually prevent the formation of light bullets in three-dimensional geometries are suppressed in the cubic nonlinear dissipative media with proper gain landscape.

Chapter 7 presents a method of generation of quasi-nondiffracting linear light bullets by the proper engineering of their spatiotemporal angular spectrum. The corresponding wave packets can propagate undistorted over considerable distances.

# Chapter 2. Stable Spatial Solitons in Engineered Materials with Periodic Linear and Nonlinear Potentials

Starting in 1965, when Kelley [27] showed that two-dimensional light self-focusing in Kerr nonlinear media is unstable; many efforts have been made to stabilize bulk solitary waves in media with third-order nonlinearity. We dwelt upon them in the Introduction, where it was mentioned that such stabilization may be achieved, for example, by adding optical lattices. In this Chapter we present two novel types of optical lattices that could stabilize solitons in bulk media.

### *2.1. Stabilization of Scalar Solitons by a Nonlinear Lattice*

Stabilization of two-dimensional solitons in materials with inhomogeneous nonlinearity landscapes has been studied in settings where domains with cubic nonlinearity are embedded into a linear medium. In this Section we show that two-dimensional solitons can also be stabilized in settings where cubic domains are embedded into materials with other types of nonlinearity, for example, into materials with saturable nonlinearity. Two cases are addressed: solitons centered in the domain with cubic nonlinearity, and solitons centered in the domain with saturable nonlinearity. As a byproduct, we also address the dynamics and stability of one-dimensional solitons in the planar settings with alternating domains with cubic and saturable nonlinearities.

The propagation of a light beam along the $\xi$-axis of a medium composed of alternating (in the transverse direction) domains with cubic and saturable

nonlinearities can be described by the spatial version of the nonlinear Schrödinger equation for the dimensionless field amplitude $q$ in conservative media [see Eq. (1.8)]. Namely:

$$i\frac{\partial q}{\partial \xi} = -\frac{1}{2}\Delta q - \frac{\left|q\right|^2 q}{1+S(\eta,\zeta)\left|q\right|^2}, \qquad (2.1)$$

where the Laplace operator can be written as $\Delta = \partial^2 / \partial\eta^2 + \partial^2 / \partial\zeta^2$ in the case of two transverse dimensions and takes on the form $\Delta = \partial^2 / \partial\eta^2$ in the case of a single transverse dimension. This equation can be obtained from Eq. (1.8) when $\Sigma(q) = \dfrac{\left|q\right|^2 q}{1+S\left|q\right|^2}$. The saturation parameter amounts to $S = 0$ in the domains with pure Kerr nonlinearity and $S = 1$ in domains with saturable nonlinearity.

We consider two different configurations: In the setting of first type in 2D the domains with saturating nonlinearity having square cross-sections with width $\rho_s$ are arranged into a square array with period $\rho_c + \rho_s$, so that square saturable domains are separated by backbone-shaped cubic regions of width $\rho_c$ [Fig. 2.1(a)]. In the second setting, cubic and saturable domains are exchanged, i.e. in this case square cubic domains with width $\rho_c$ are arranged into square array and separated by backbone-shaped saturable regions [Fig. 2.1(b)]. In both cases we assume that soliton resides in the point $\eta,\zeta = 0$. The cross-sections of such structures along either $\eta$ or $\zeta$ axes represent distribution of saturable and cubic domains in corresponding 1D lattices.

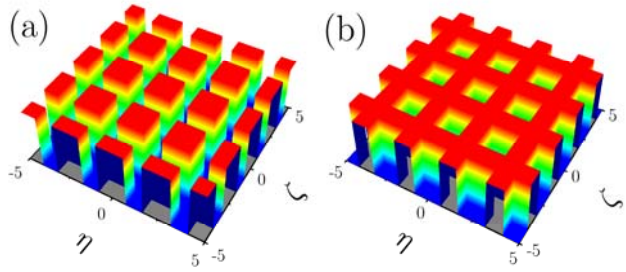


Figure 2.1. Distribution of saturation parameter in two-dimensional nonlinear lattice for the case when soliton with a center in the point $\eta,\zeta = 0$ resides on saturable domain (a) and on cubic domain (b).

First, we consider solitons in 1D nonlinear lattices. We search for soliton solutions of Eq. (2.1) in the form $q = w(\eta)\exp(ib\xi)$, where the function $w(\eta)$

describes the soliton profile and $b$ is the propagation constant. Representative profiles of solitons centered on the domain with cubic nonlinearity surrounded by domains with saturable nonlinearity are shown in Fig. 2.2(a). Such solitons always feature bell-like shapes with very weak oscillations on top of them due to the transverse modulation of the nonlinearity. Increasing the propagation constant results in the progressive localization of light inside the cubic domain. This is accompanied by a monotonic growth of the soliton energy flow $U = \int_{-\infty}^{+\infty} |q|^2 \, d\eta$, as shown by curve 1 in Fig. 2.2(c). Notice that the energy flow vanishes when $b \to 0$, since the role of the nonlinear lattice diminishes when the peak amplitude decreases. This is in contrast to soliton behavior in linear lattices, when only the refractive index is modulated, that impose restrictions on the available $b$ values.

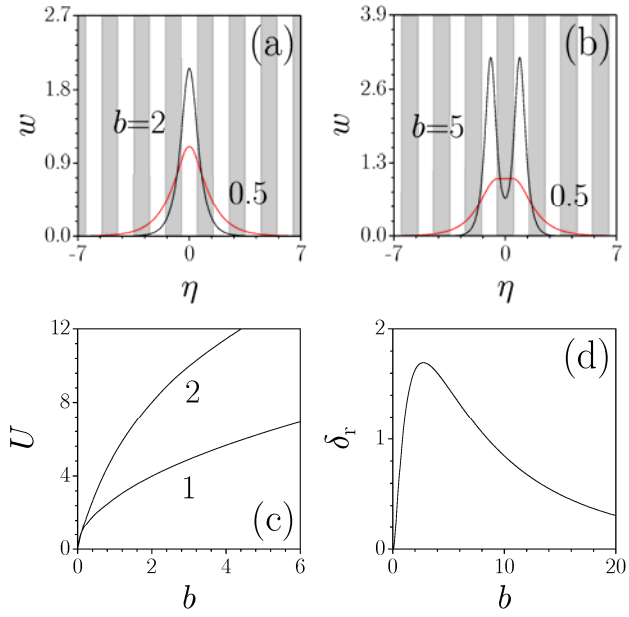


Figure 2.2. Profiles of solitons centered on (a) cubic and (b) saturable domains. Gray regions indicate saturable domains, while white regions indicate cubic domains. (c) $U$ versus $b$ for solitons residing on cubic domain (curve 1) and on saturable domain (curve 2). (d) $\delta_r$ versus $b$ for solitons centered on saturable domain. In all cases $\rho_c = 1$, $\rho_s = 1$.

The most interesting results occur for solitons centered on saturable domains. With increase of $b$ such solitons first develop flat-top field distributions inside the saturable domain, while the soliton tails inside neighboring cubic domains rapidly fade away. For even larger propagation constant values such solitons experience considerable reshaping because two humps tend to develop on the soliton profile in regions with cubic nonlinearity, so that at sufficiently high peak intensities the light concentrates almost entirely in two cubic domains

nearest to the central saturable domain [see Fig. 2.2(b)]. This situation takes place even for small widths of domains $\rho_{\mathrm{s}}, \rho_{\mathrm{c}}$, although with decrease of $\rho_{\mathrm{s}}, \rho_{\mathrm{c}}$ such shape transformations appear at progressively increasing power levels. The tendency for localization on cubic domains can be understood if one takes into account that the nonlinear contribution to refractive index in cubic domains $\sim \left|q\right|^2$ is higher than nonlinear contribution in saturable domains $\sim \left|q\right|^2 / (1 + S\left|q\right|^2)$. The energy flow of solitons centered on saturable domains also monotonically increases with $b$ [see curve 2 in Fig. 2.2(c)]. Interestingly, while $U(b)$ curves for solitons centered on different types of domains almost coincide for $b \to 0$, for large $b$ values the energy flow of soliton centered on saturable domain is approximately two times higher than that of soliton centered on cubic domain.

The key property of all solitons addressed here is their stability. We study whether the obtained states are stable or not by the well-known method of linear stability analysis. For this purpose we searched for the profiles of perturbed soliton solutions in the form $q = [w + u\exp(\delta\xi) + iv\exp(\delta\xi)]\exp(ib\xi)$, where $u, v \ll w$ are real and imaginary parts of small perturbation, while $\delta = \delta_{\mathrm{r}} + i\delta_{\mathrm{i}}$ is the perturbation growth rate that may be complex. Substitution of this expression into Eq. (2.1) and linearization around stationary unperturbed solution $w$ leads to the following eigenvalue problem:

$$\begin{aligned} \delta u &= \mathcal{L}_v v = -\frac{1}{2}\Delta v + bv - v\frac{w^2 + Sw^4}{(1+Sw^2)^2}, \\ \delta v &= \mathcal{L}_u u = +\frac{1}{2}\Delta u - bu + u\frac{3w^2 + Sw^4}{(1+Sw^2)^2}. \end{aligned} \qquad (2.2)$$

The analysis of Eqs. (2.2) for solitons centered on cubic and saturable domains reveals that the former type of solitons is always stable and may propagate undistorted over considerable distances even in the presence of strong perturbations, while the latter is unstable for all propagation constant values. In Fig. 2.2(d) we show the dependence of the real part of the perturbation growth rate on the propagation constant for solitons centered on saturable domains. The dependence $\delta_{\mathrm{r}}(b)$ is nonmonotonic and the growth rate asymptotically approaches zero when $b \to \infty$. In the presence of input perturbations such solitons quickly reshape into single-peak states centered on cubic domains that are stable.

Now we address two-dimensional solitons in settings with alternating cubic and saturable domains. Figure 2.3(a) shows typical intensity profiles of solitons centered on cubic domains, while Fig. 2.3(b) shows solitons centered on saturable domains. One can see that upon increase of the propagation constant, solitons residing on cubic domains gradually localize in them retaining a bell-shaped distribution, while their counterparts on saturable domains exhibit

considerable power-dependent shape transformations. Like in one-dimensional case, solitons in saturable domains first develop flat-top shapes, while further increase of $b$ results in appearance of four local maxima on otherwise smooth field distribution, whose positions coincide with positions of domains with cubic nonlinearity. For large $b$ values light field concentrates almost entirely in cubic regions, so that soliton profile resembles four well-localized bright spots. Notice that at low powers, when $b \to 0$, 2D solitons residing on both cubic and saturable domains extend dramatically across nonlinear lattice, without developing any noticeable shape oscillations.

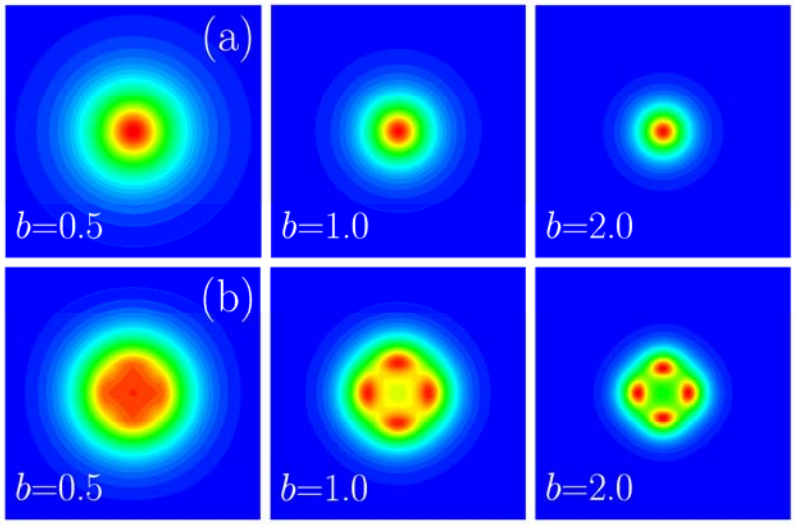


Figure 2.3. Profiles of solitons centered on (a) cubic domain when $\rho_c = 1.5$, $\rho_s = 1.0$ and (b) saturable domains when $\rho_c = 1.0$, $\rho_s = 2.0$.

In contrast to the one-dimensional geometry, the energy flow of two-dimensional solitons $U(b) = \int\int_{-\infty}^{+\infty} |q|^2 \, d\eta d\zeta$ in the nonlinear lattice is a non-monotonic function of $b$. In Fig. 2.4(a) we show the dependencies $U(b)$ for solitons centered on saturable domains, for different values of $\rho_s$. In this case, the energy flow first grows with $b$, reaches its maximal value, and then decreases. When $b \to \infty$ the energy flow asymptotically approaches $4U_T$, where $U_T \approx 5.85$ is the energy flow of the so-called Townes soliton in uniform cubic medium [14]. However, despite the fact that the dependence $U(b)$ is non-monotonic and that there exist an inflection point where the derivative $dU / db$ changes its sign, the linear stability analysis shows that solitons centered on saturable domains are always unstable. Note that we are dealing with a system where the Vakhitov-Kolokolov stability criterion may not give the correct prediction of stability

domains for fundamental solitons (for other examples see [107, 111]). The typical evolution of unstable perturbed solitons centered on saturable domain is shown in Fig. 2.5(a). After a rather short propagation distance, light tends to concentrate in one domain with cubic nonlinearity.

The linear stability analysis performed with the aid of Eq. (2.2) allowed us to obtain the dependence of the growth rate on the propagation constant, which is shown in Fig. 2.4(b). One can see that $\delta_r$ does not vanish in the entire soliton existence domain. The corresponding instability is of oscillatory character. Such behavior is in contrast to the well-established stability of 2D solitons in uniform saturable medium, where collapse is arrested.

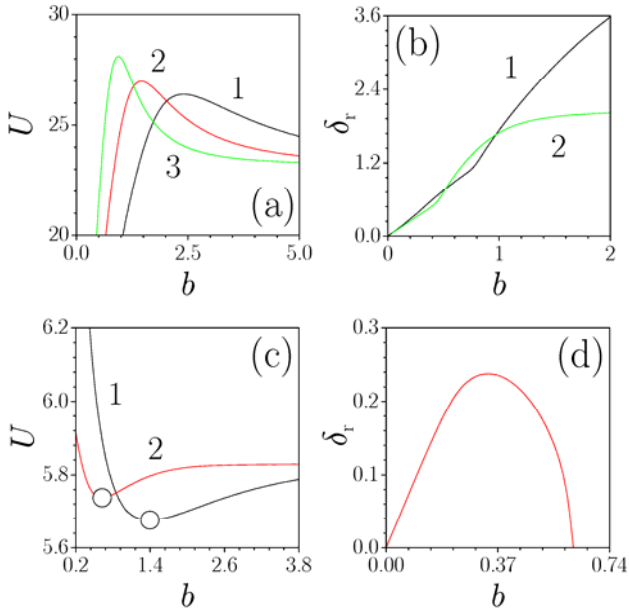


Figure 2.4. (a) $U$ versus $b$ for solitons centered on domain with saturable nonlinearity at $\rho_s = 1.5$ (curve 1), $2.0$ (curve 2), and $2.5$ (curve 3). (b) $\delta_r$ versus $b$ for solitons centered on domain with saturable nonlinearity at $\rho_s = 1.5$ (curve 1), $2.5$ (curve 2). In (a) and (b) $\rho_c = 1.0$. (c) $U$ versus $b$ for solitons centered on domain with cubic nonlinearity at $\rho_c = 1.0$ (curve 1) and $1.5$ (curve 2). Circles in (c) separate stable and unstable branches. (d) $\delta_r$ versus $b$ for solitons centered on domain with cubic nonlinearity at $\rho_s = 1.5$. In (c) and (d) $\rho_s = 1.0$.

On the other hand, the well-known instability of solitons in uniform cubic media also can be suppressed in the present settings. Our analysis shows that alternation of cubic and saturable nonlinear domains in the transverse plane does

allow stabilization of two-dimensional solitons centered on cubic domains in such purely nonlinear lattice. The typical dependence of energy flow $U$ on $b$ for such solitons is shown in Fig. 2.4(c) for two different widths of cubic domains $\rho_c$. Notice a completely different character of $U(b)$ dependencies for solitons centered on cubic and saturable domains. With increase of $b$ in Fig. 2.4(c) the energy flow decreases, reaches its minimal value at $b = b_{cr}$, and then starts increasing. Thus, there exists a minimal value of energy flow, which decreases with lowering of the width of the cubic domains. The energy flow $U$ asymptotically approaches the value $U_T \approx 5.85$ when $b \to \infty$. By performing a linear stability analysis we found that in the case of solitons centered on cubic domains the Vakhitov-Kolokolov stability criterion does give the correct prediction for domains of soliton stability. Namely, solitons corresponding to the branch with $dU/db > 0$ are linearly stable, while solitons from the branch $dU/db \leq 0$ are unstable. Figure 2.4(d) shows that the real part of the growth rate becomes zero exactly in the inflection point of $U(b)$ dependence, where derivative $dU/db$ changes its sign.

The critical value of propagation constant, $b_{cr}$, at which solitons become stable increases when the width of domains with cubic nonlinearity decreases. Direct propagation of perturbed solitons centered on cubic domains confirms the predictions of the linear stability analysis. Perturbed solitons with $b > b_{cr}$ clean up the noise and propagate undistorted over indefinitely long distances [see an example of stable propagation in Fig. 2.5(b)].

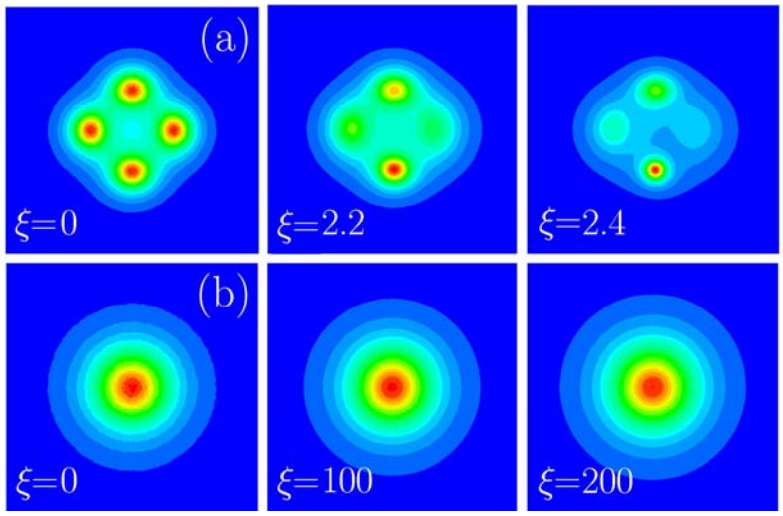


Figure 2.5. (a) Decay of solitons centered on saturable domain at $b = 2.0$, $\rho_c = 1.0$, $\rho_s = 2.0$, and (b) stable propagation of soliton centered on cubic domain at $b = 2.0$, $\rho_c = 1.5$, $\rho_s = 1.0$. Field modulus distributions are shown at different distances.

The difference in the stability properties of solitons centered on cubic and saturable domains is consistent with the applicability conditions of the Vakhitov-Kolokolov criterion. In fact for complete stability of solutions in addition to slope condition $dU / db > 0$ the so-called spectral stability condition should be satisfied. Such spectral instability imposes restrictions, that depend on the domain where soliton center is located, on the number of eigenvalues of linearized operators $\mathcal{L}_u, \mathcal{L}_v$ in the eigenvalue problem (2.2) $\delta u = \mathcal{L}_v v$, $\delta v = \mathcal{L}_u u$. While violation of the slope condition in two-dimensional case results in collapse or decay (as it occurs, for example, in uniform cubic medium), the violation of spectral stability condition results in appearance of eigenvalues with $\delta_{\mathrm{r}} \neq 0$ with associated non-symmetric eigenvectors that indicates that solitons tend to experience transverse drift under the action of such perturbations [107, 108]. Thus, while in our setting solitons residing on saturable domains satisfy the slope condition for certain $b$ values, they do not satisfy the spectral stability condition. As a result they tend to shift to domains with cubic nonlinearity. On intuitive physical grounds, this is understood by taking into account that in cubic domains the nonlinear contribution to refractive index is higher. At the same time, solitons residing on the cubic domains satisfy both conditions as long as $b > b_{\mathrm{cr}}$ and therefore can be stable.

### *2.2. Stabilization of Vector Solitons by Linear or Nonlinear Lattice Acting in One Component*

Stabilization of two-dimensional solitons may be also possible in multi-component states. In particular, it has been shown that linear lattices readily support stable two-dimensional vector solitons composed of two coupled light beams [126, 127]. In nonlinear lattices vector solitons have been considered only in one-dimensional geometries [128]. In all cases, it was assumed that the lattices act equally on *both* components of the vector soliton. A challenging issue is whether such solitons can be made stable when the lattice (linear or nonlinear) selectively acts on a *single* component, with the medium being uniform for the other one. In this Section we address the existence and stability of two-dimensional two-component bright solitons, when a linear or nonlinear lattice affects only one field component. It is shown that the cross-phase-modulation coupling may result in the stabilization of the entire vector complex, despite the fact that the second component is not directly stabilized by any lattice (i.e., such a scalar mode would decay or collapse when propagating alone).

The evolution of a two-dimensional multi-component light field in the presence of linear or nonlinear lattice acting on one component only, is governed by the coupled nonlinear Schrödinger equations for dimensionless field amplitudes $q_{1,2}$:

$$
\begin{aligned}
i\frac{\partial q_1}{\partial \xi} &= -\frac{1}{2}\Delta q_1 - \left[\sigma\left(\eta,\zeta\right)\left|q_1\right|^2 + C\left|q_2\right|^2\right]q_1 - pR\left(\eta,\zeta\right)q_1, \\
i\frac{\partial q_2}{\partial \xi} &= -\frac{1}{2}\Delta q_2 - \left[\left|q_2\right|^2 + C\left|q_1\right|^2\right]q_2,
\end{aligned}
\tag{2.3}
$$

Here the function $\sigma\left(\eta,\zeta\right)$ describes a nonlinearity landscape in the case when the component $q_1$ is subject to the action of a nonlinear lattice, while the function $R\left(\eta,\zeta\right)$ represents a linear lattice with depth $p$. The second term in square brackets in Eq. (2.3) describes the cross-modulation coupling between components, whose strength is described by the coefficient $C$. To analyze the effects of the nonlinear lattice, we set $p=0$ and adopt the nonlinearity-modulation landscape with $\sigma=1$ inside a square array of circles of radius $\rho_r$, with spacing $\rho_{sp}$ between them, while between the circles the medium is supposed to be linear, with $\sigma=0$. The results are reported here for the case of $\rho_r=0.5$ and $\rho_{sp}=2$, which adequately represents the generic situation. We stress that the nonlinearity acting on the second component, $q_2$, is spatially uniform. In contrast, to consider linear lattice effects, we assume that the nonlinearity is uniform in both components, i.e., $\sigma\equiv 1$, but the linear potential is present, with $p\neq 0$ and $R\left(\eta,\zeta\right)=\cos\left(\Omega\eta\right)\cos\left(\Omega\zeta\right)$. Here we set $p=4$ and $\Omega=2$.

Crucially important for the stability of vector solitons in the present model is the value of the cross-phase-modulation coefficient, $C$, which takes on different values in different physical settings. In optical systems, $C=1$ for mutually incoherent light beams, $C=2/3$ for coherent beams with orthogonal linear polarizations in strongly birefringent media, and $C=2$ for circular polarizations, or for two waves with different carrier wavelengths. In addition to that, $C$ may be large in organic materials, and it may be engineered at will in photonic-crystal fibers. Additional possibilities for the manipulation of the cross-phase-modulation coupling are offered by photorefractive crystals, through varying the polarization of the beams and/or elements of the underlying electro-optic tensor. Therefore, we consider $C$ as a control parameter varying in a relatively broad range.

We search for vector-soliton solutions to Eqs. (2.3) as $q_{1,2}\left(\eta,\zeta,\xi\right)=w_{1,2}(\eta,\zeta)\exp(ib_{1,2}\xi)$, where $b_{1,2}$ are the corresponding propagation constants. We look for the simplest solutions with a fundamental (bell-shaped) intensity distributions in both components. Nevertheless, because the lattice acts on one component, the shapes of $w_1$ and $w_2$ are always different, even if $b_1=b_2$ (in contrast to uniform cubic media, where one has $w_1=const\cdot w_2$ for $b_1=b_2$). To cope with the large number of parameters in the model, we fix the propagation constant of the first component, $b_1=3$, and vary $b_2$ and $C$. A detailed numerical

analysis indicates that the results do not change significantly for other values of $b_1$, as long as they belong to a domain where the corresponding scalar soliton, with $q_1 \neq 0$, $q_2 = 0$, supported by nonlinear or linear lattice is stable. Notice also that Eqs. (2.3) conserve the total and partial norms of the two components:

$$U = U_1 + U_2 \equiv \int\int_{-\infty}^{\infty} \left( \left|q_1\right|^2 + \left|q_2\right|^2 \right) d\eta d\zeta, \tag{2.4}$$

which also determine the power sharing between them, namely $S_{1,2} \equiv U_{1,2} / U$.

Typical field profiles of the 2D vector solitons are shown in Fig. 2.6, by means of cross-sections drawn through $\zeta = 0$. As mentioned above, in both cases of the nonlinear [Fig. 2.6(a) and (b)] and linear [Fig. 2.6(c) and (d)] lattices, the propagation constant $b_1 = 3$ was selected so that in the absence of the second component $q_2$ for which the medium is uniform, the corresponding scalar soliton with $q_1 \neq 0$, $q_2 = 0$, $C = 0$ is stable [for a detailed analysis of the stability of scalar solitons in nonlinear lattices see Ref. 113]. Only in this case the stabilization of the second component may be provided by the cross-phase-modulation-induced coupling to its counterpart that is directly stabilized by the nonlinear lattice. At $C > 1$, an increase of $b_2$ results in a decrease of the amplitude of the second component, in both cases of linear and nonlinear lattices, so that for sufficiently large $b_2$ the second component becomes much weaker than the first one [see Figs. 2.6(b) and (d)], and, at a certain value $b_2 = b_2^{upp}$, the second component vanishes altogether, so that the vector soliton degenerates into a scalar one with $w_1 \neq 0$, $w_2 = 0$. The resulting scalar soliton is stable because of the proper choice of $b_1$. In contrast, the decrease of $b_2$ results in a reduction of the first component [see Figs. 2.6(a) and (c)], so that, at another threshold, $b_2 = b_2^{low}$, the vector soliton degenerates into a different scalar mode, with $w_1 = 0$, $w_2 \neq 0$. Since for the second component the medium is uniform, the latter scalar mode is tantamount to the usual Townes soliton in the uniform Kerr medium, which is always unstable [14]. Therefore, in the present model the vector solitons exist in a limited range of values of the propagation constant, $b_2^{low} \leq b_2 \leq b_2^{upp}$. Naturally, this existence domain dramatically depends on the cross-phase-modulation coefficient, $C$.

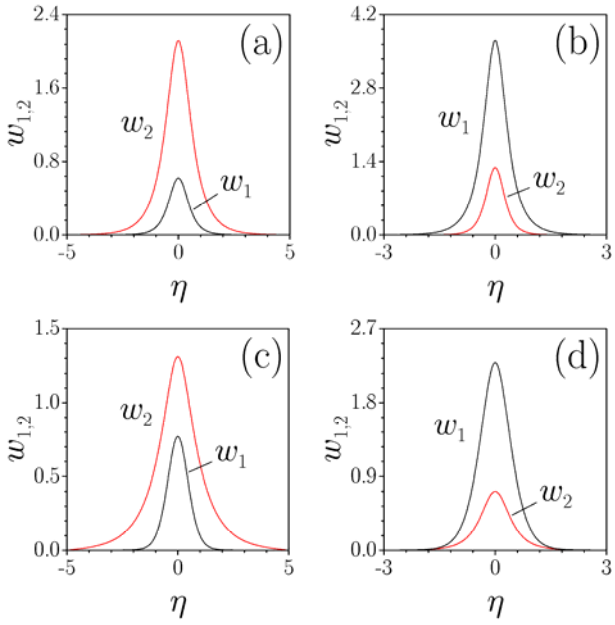


Figure 2.6. Field distributions $w_{1,2}(\eta)$ at $\zeta = 0$ in 2D vector solitons with (a), (b) nonlinear and (c), (d) linear lattices acting on the first component only. In all cases, $C = 2$, $b_1 = 3$ are fixed, while $b_2 = 1$ (a), 9 (b), 0.4 (c), and 2.5 (d). Solitons shown in panels (a), (c) are unstable, while solitons from panels (b), (d) are stable.

Remarkably, the situation described above for $C > 1$ is completely reversed at $C < 1$. In this case, the norm of the second component increases when $b_2 \to b_2^{upp}$ and vanishes when $b_2 \to b_2^{low}$. In all cases, the shapes of both the first and second component are smooth, without pronounced oscillations that might be induced by the lattice. This is because the second component is not affected by the lattice, while the propagation constant of the first component is sufficiently large to ensure its stability in the scalar case, which implies that the corresponding field $w_1$ is well localized within few sites of the linear or nonlinear lattice.

The properties of the vector solitons are summarized in Fig. 2.7 that shows typical dependencies of the norm and energy sharing between the soliton components versus $b_2$ for both the nonlinear lattice [Figs. 2.7(a) and (b)] and for the linear lattice [Figs. 2.7(c) and (d)] models. The norm is a non-monotonous function of $b_2$ - at $C = 2$, it first decreases with increasing $b_2$, but then it starts to grow, as shown in Figs. 2.7(a) and 2.7(c). The behavior of the total norm is different at $C < 1$ - in that case, $U$ first grows and then diminishes with the

increase of $b_2$. Since at $C = 2$ the norm of the second component grows when $b_2 \to b_2^{low}$, while the norm of the first component increases at $b_2 \to b_2^{upp}$, the energy sharing $S_{1,2}$ between the soliton components drastically varies in the interval $[b_2^{low}, b_2^{upp}]$, as shown in Figs. 2.7(b) and (d). Interestingly, in the case of the nonlinear lattice the values of the total norm of the vector solitons at the borders of the existence domain (i.e., at $b_2 \to b_2^{low}$ and $b_2 \to b_2^{upp}$) are very similar, despite the fact that the energy (norm) is concentrated in different components. However, in the presence of the linear lattice, $U\left(b_2 = b_2^{upp}\right)$ is considerably smaller than $U\left(b_2 = b_2^{low}\right)$.

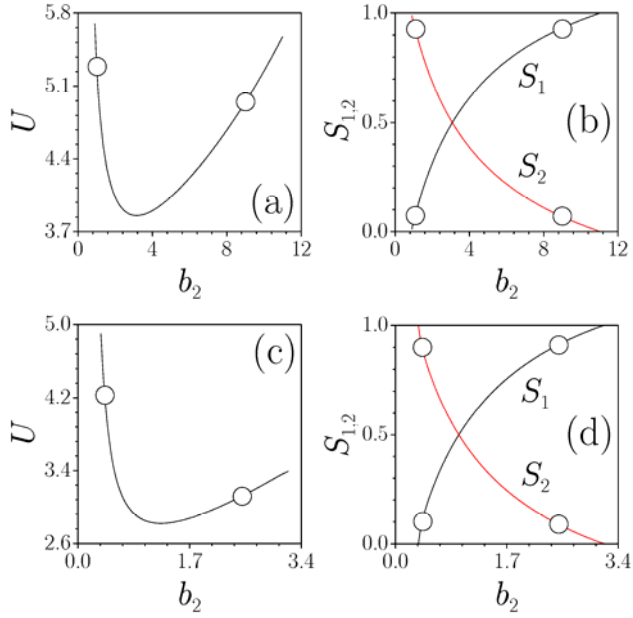


Figure 2.7. The total energy flow (a) and power sharing between the two components (b) versus $b_2$ at $b_1 = 3$ and $C = 2$ for the vector soliton with the nonlinear lattice acting on the first component. Panels (c) and (d) show the same, but when the linear lattice acts in the first component. Points correspond to solitons shown in Fig. 2.6.

The transformation of the vector soliton into a stable scalar mode at $b_2 \to b_2^{upp}$, and its transformation into the unstable Townes soliton at $b_2 \to b_2^{low}$ (recall that this picture holds for $C > 1$, while for $C < 1$ the situation is inverse) suggest that the vector state may be stable in a range of values of $b_2$ close to $b_2^{upp}$, and the stability is lost somewhere inside the existence domain $[b_2^{low}, b_2^{upp}]$.

The main result is that the stabilization of the vector solitons is indeed possible for both cases of linear and nonlinear lattices acting on the single component. Figure 2.8 shows the domains of existence and stability for the vector solitons in the plane $\left(C, b_2\right)$. The stability domain was obtained by collecting simulation results for the propagation of perturbed vector solitons corresponding to different values of $b_2$ and $C$, over a huge distance, $\xi \sim 1000$. The existence domains of the vector solitons shrink around $C = 1$, but then expand with the increase or decrease of the cross-phase-modulation strength.

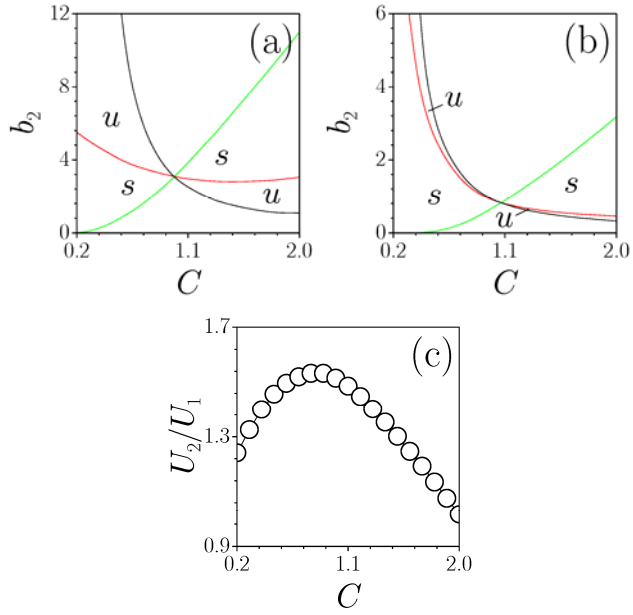


Figure 2.8. Domains of the stability ("s") and instability ("u") for vector solitons with (a) nonlinear and (b) linear lattice acting on the first component in the $\left(C, b_2\right)$-plane for $b_1 = 3$. In both cases the vector solitons exist at $b_2^{low} \le b_2 \le b_2^{upp}$ in the region between the black and green curves. (c) The ratio of norms (energy flows), $U_2/U_1$, of the two components of the vector soliton, taken at the border of the stability domain depicted in panel (a) versus $C$.

The structure of the existence domains for both the nonlinear [Fig. 2.8(a)] and linear [Fig. 2.8(b)] lattices is similar. The vector solitons exist between the black and green curves, with the second component vanishing on the green curve, and first component vanishing along the black one. The stability domains, marked by "s", are located close to the green curves, while the instability domains, marked by "u", are situated close to the black curves. The border of the stability domain is depicted by the red curve. One can see from Fig. 2.8(b) that the linear lattice stabilizes the vector solitons almost in their entire existence domain, while for the

nonlinear lattice the widths of the stability and instability domains in Fig. 2.8(a) are comparable. The main reason behind this fact is that the nonlinear lattice strength, hence its ability to stabilize the solitons, depends on the power of the soliton itself. Therefore, in such lattices the amplitude of the first component, which is subject to the action of the lattice, should be comparable with or larger than the amplitude of the second component. This is in contrast to the case of the linear lattice, where even weak $w_1$ carrying a relatively small norm, can result in the stabilization of the entire vector complex. Figure 2.8(c) shows the ratio of the norms, $U_2/U_1$, of the components of the vector soliton, supported by the nonlinear lattice and taken at a border of the stability domain [the red curve in Fig. 2.8(a)] versus the cross-phase-modulation coefficient $C$. One can clearly see that, in the case of the nonlinear lattice, this ratio is of the order of unity for any value of $C$ in the range of $[0.2, 2.0]$. The ratio $U_2/U_1$ apparently decreases as one moves deeper into the stability domain by varying $b_2$. In contrast to that, in the case of the linear lattice, when the stability domain almost entirely overlaps with the entire existence domain, the ratio $U_2/U_1$ may assume much higher values for stable vector solitons. In particular, for $C = 2$ the ratio at the stability border in the model with linear lattice is $U_2/U_1 = 5.5$, while for $C = 0.5$ this ratio is $U_2/U_1 = 17.6$. These results clearly indicate that even a small-amplitude component affected by the linear lattice can readily stabilize the entire vector soliton.

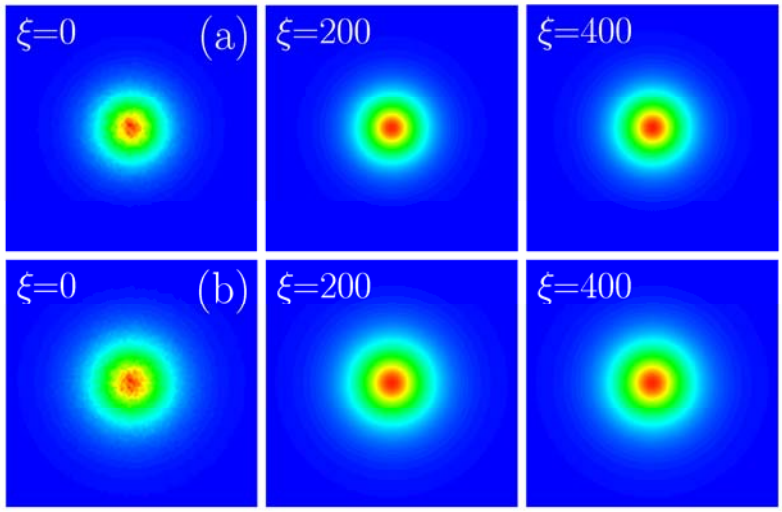


Figure 2.9. The stable propagation of a perturbed vector soliton with the nonlinear (a) and linear (b) lattice acting in the first component, at $C = 2$. Only the distribution of the absolute value of the field in the second component is shown. The solitons displayed in (a) and (b) correspond to $b_1 = 3$, $b_2 = 5.5$, and $b_1 = 3$, $b_2 = 2.5$, respectively.

The results reported do not vary dramatically upon variation of the propagation constant of the first component, $b_1$, although such variation considerably affects the soliton existence and stability domains. In particular, increasing $b_1$ when $C > 1$ results in a considerable expansion of the existence and stability domains. For instance, at $b_1 = 10$ and $C = 2$, the vector solitons in the nonlinear lattice exist between $b_2^{low} = 3$ and $b_2^{upp} = 34.5$, and become completely stable at $b_2 > 10.5$.

Typical examples of the stable propagation of vector solitons perturbed by significant white noise in the models with both linear and nonlinear lattices are shown in Figs. 2.9(a) and (b), respectively. While unstable vector solitons evolve dynamically, the stable ones propagate without any considerable distortion over indefinitely long distances.

### *2.3. Summary*

Two possible methods to stabilize two-dimensional solitons in cubic medium are proposed in this Chapter. The first one employs a nonlinear lattice composed of material domains with cubic and saturable nonlinearity. The second one utilizes a linear or a nonlinear lattice acting on one soliton component only, and stabilization of the entire vector state is achieved due to cross-phase-modulation between components.

Scalar solitons in nonlinear cubic-saturable lattices centered on cubic domains can be stabilized when the soliton propagation constant exceeds a critical value. It was also found that in both one- and two-dimensional geometries solitons centered on saturable domains of the nonlinear lattice are unstable in contrast to the media with pure saturable nonlinearities. They undergo shape transformations with increasing peak intensity when light concentrates in regions with cubic nonlinearity.

Instead of stabilizing two-dimensional scalar soliton in Kerr media directly, it is possible to work with multi-component or vector solitons and stabilize the entire state by acting on only one component. It was found that while even a weak component affected by the linear lattice is sufficient for the stabilization of the entire complex, the stabilization in the nonlinear lattice requires that the norm in the component which is directly supported by the lattice should be comparable to or greater than the norm of the other component, for which the medium is uniform.

The main results summarized in this chapter have been published in the following journals:

1. **O.V. Borovkova,** Y.V. Kartashov, and L. Torner, “Stabilization of two-dimensional solitons in cubic-saturable nonlinear lattices,” Phys. Rev. A **81**, 063806 (2010).

2. **O.V. Borovkova,** B.A. Malomed, and Y.V. Kartashov, “Two-dimensional vector solitons stabilized by a linear or nonlinear lattice acting in one component” Europhys. Lett. **92**, 64001 (2010).

# Chapter 3. 1D and 2D Bright Solitons Supported by Inhomogeneous Defocusing Nonlinearities

A commonly adopted principle underlying the studies of the bright solitons in various physical settings is that they are supported either by the focusing nonlinearity [4] or, in the form of gap solitons, by the defocusing nonlinearity combined with periodic linear potentials [129]. We propose several types of the engineered materials with purely defocusing nonlinearity, whose strength grows fast enough toward the periphery of the material, where a generation of the bright solitons becomes possible without any additional refractive index modulations. One of the most important issues addressed in this Chapter is the value of minimal growth rate of the defocusing nonlinearity in the transverse plane of the sample that is required for the existence of bright solitons.

The existence of the bright solitons in settings presented here is a consequence of the fact that, in contrast to media with homogeneous nonlinearities where the presence of the decaying tails of the soliton places it into the semi-infinite spectral gap of the linearized system in which defocusing nonlinearities cannot support any self-localization, in our case the growth of the nonlinearity coefficient makes the underlying equations nonlinearizable for the decaying tails.

### *3.1. Bright Solitons Supported by Defocusing Nonlinearities, growing exponentially toward the Periphery*

The first type of the complex engineered material that can support bright solitons is the medium with a cubic nonlinearity whose strength grows exponentially toward the periphery. In this very simple system not only numerical, but also a variety of analytical solutions can be obtained. Below we consider both fundamental and higher-order solitons in one- and two-dimensional geometries.

The governing equation describing the propagation of light in the medium with inhomogeneous cubic nonlinearity is the nonlinear Schrödinger equation:

$$i\frac{\partial q}{\partial \xi} = -\frac{1}{2}\Delta q + \sigma\left(\vec{r}\right)\left|q\right|^2 q, \tag{3.1}$$

Here $\vec{r} = \left(\eta, \zeta\right)$ is the radius-vector of the point in the transverse plane with coordinates $\eta$ and $\zeta$, and $\sigma\left(\vec{r}\right) > 0$ is the defocusing nonlinearity strength that varies in the radial direction. Equation (3.1) can be obtained from Eq. (1.8) mentioned in the Introduction when $\beta = 0$ and $\Sigma\left(q\right) = \sigma\left(\vec{r}\right)\left|q\right|^2 q$.

The Eq. (3.1) could be solved analytically if the nonlinearity strength has a special form. We assume that it grows with radius as

$$\sigma\left(\vec{r}\right) = \left(\sigma_0 + \sigma_2 r^2/2\right)\exp\left(\alpha r^2\right), \tag{3.2}$$

here $r$ is the radial coordinate; parameters $\sigma_0, \sigma_2 > 0$, and $\alpha > 0$ may be fixed by scaling (we set $\alpha = 1/2$ below). Spatially inhomogeneous nonlinearities can be realized in various ways [72]. In particular, in the photorefractive materials, such as $LiNbO_3$, nonuniform doping with Cu or Fe may considerably enhance local nonlinearity [130]. The effective modulation of the nonlinearity could be also achieved via the inhomogeneity of the two-photon resonance detuning, controlled by an external field, with the exact resonance occurring at $r = \infty$.

For any dimension $D$, Eq. (3.1) with $\sigma\left(\vec{r}\right)$ taken as per Eq. (3.2) admits the particular analytical solution for the fundamental solitons:

$$q\left(r, \xi\right) = \left(\alpha^2/\sigma_2\right)^{1/2}\exp\left(ib\xi - \alpha r^2/2\right), \tag{3.3}$$

with the propagation constant $b = -\left(D\alpha/2 + \sigma_0 \alpha^2/\sigma_2\right)$.

At the same time, for $\sigma_2 = 0$, the exact solutions for the vortex with topological charge $m = 1$ in 2D, and dipole soliton in 1D are also available:

$$q\left(r,\xi\right)=\left(2\sigma_{0}\right)^{-1/2}\alpha r\exp\left(ib\xi+i\phi-\alpha\, r^{2}/2\right),\tag{3.4}$$

with $b=-\alpha\left(1+D/2\right)$, where an azimuthal coordinate $\phi$ is a part of the solution for $D=2$.

The analytical solutions correspond to the particular values of the propagation constant $b$ (multiplying Eq. (3.1) by $q^{*}$ and integrating, one can prove that the solitons may exist only for $b<0$). For families of the fundamental solitons, a variational approximation can be developed in any dimension by adopting an ansatz suggested by the exact solutions, $q=A\exp\left(ib\xi-\alpha\, r^{2}/2\right)$ (here the amplitude $A$ is a variational parameter). Using the Lagrangian of Eq. (3.1), the variational approach yields the norm of the fundamental solitons as a function of $b$, written here at $\sigma_{2}=0$ and $\sigma_{0}=1$:

$$U\equiv\int\left|q\left(\vec{r}\right)\right|^{2}d\vec{r}=\left(\pi/\alpha\right)^{D/2}\left(b+\alpha\, D/4\right).\tag{3.5}$$

A comparison with the numerical results presented in Figures 3.1(c) and 3.3(c) demonstrates that variational dependencies $U\left(b\right)$ are virtually indistinguishable, on the scale of the figures, from their numerical counterparts for all dimensions. For soliton's width, defined as $W=2U^{-1}\int r\left|q\left(\vec{r}\right)\right|^{2}d\vec{r}$, the variational approach gives $W_{1D}=2/\left(\pi\alpha\right)^{1/2}$, $W_{2D}=\left(\pi\alpha\right)^{1/2}$. Numerically found widths approach these values with the increase of $U$.

It should be stressed that the steep anti-Gaussian profile of the modulation of the defocusing nonlinearity postulated in Eq. (3.2) is not an absolutely necessary condition for the existence of solitons. In fact, a law $\sigma\left(r\right)\sim r^{D+\varepsilon}$ with arbitrary $\varepsilon>0$, where $D$ is the spatial dimension, is sufficient. Furthermore, for the exponential profile $\sigma\left(\eta\right)=a+\sinh^{2}\left(\eta\right)$, with any $a<1$, it is easy to find the exact 1D soliton solution, $w=\left(1-a\right)^{-1/2}\operatorname{sech}\left(\eta\right)$ with $b=-\left(1+a\right)/\left[2\left(1-a\right)\right]$, and for $\sigma\left(\eta\right)=\cosh^{2}\left(\eta\right)$ one can find the exact dipole solution $w=3^{1/2}\sinh\left(\eta\right)\operatorname{sech}^{2}\left(\eta\right)$ with $b=-5/2$.

Further we present the numerical results for the model (3.2) with $\sigma_{2}=0$ and $\sigma_{0}\equiv1$. The fundamental solitons are sought for as $q\left(\vec{r},\xi\right)=w(r)\exp\left(ib\xi\right)$. The solutions were found using the standard relaxation method that quickly converges to exact solitons for a properly selected initial guess. The stability of solutions thus found was investigated by the numerical computation of eigenvalues for small perturbations (with the help of an ordinary eigenvalues solver), using the

linearization of Eq. (3.1), and then verified through direct simulations of the perturbed evolution.

The main result confirming the analytical findings described above is that, in contrast to the common belief that the defocusing nonlinearity cannot give rise to the bright solitons, the inhomogeneous defocusing medium *does* support families of stable localized modes. The tails of solitons of all such types decay at $r \to \infty$ super-exponentially, irrespectively of the dimensionality of the problem $w\big|_{\eta\to\pm\infty} \approx \left(\alpha r \big/ 2^{1/2}\right)\exp\left(-\alpha r^2 \big/ 2\right)$, which compiles with the exact solutions (3.4). Note that this asymptotic form does not contain the propagation constant $b$.

The examples of 1D solitons, with different numbers $k$ of zeros (nodes) in the $w(\eta)$ shape, are displayed in Figs. 3.1(a) and 3.1(b). The soliton amplitude increases with $|b|$, and the numerical results show that their width, at first, rapidly decreases and then saturates at $|b| \simeq 20$ (as it has been predicted by the variational approach). For all types of solitons, their energy flow (norm) increases with $|b|$ [Fig. 3.1(c)]. The solitons of higher orders have smaller norms, which is natural, taking into account the fact that the fundamental solitons, representing the ground state of the system, must minimize the value $-b$ for a given norm.

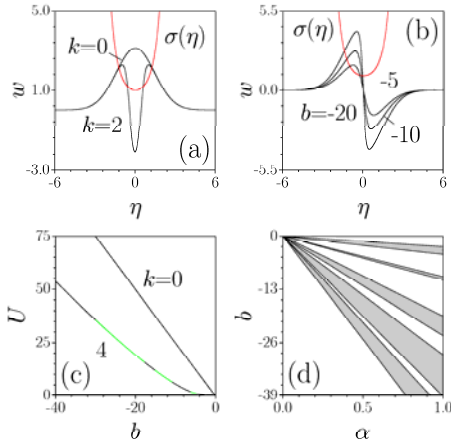


Figure 3.1. Profiles of 1D solitons: (a) with $b = -10$ and different numbers of nodes; (b) dipole solitons with different values of $b$. This and other figures are displayed for $\alpha = 0.5$ in Eq. (3.2), with the red horseshoe-shaped curves showing the nonlinearity modulation profile. (c) $U$ vs $b$ for 1D solitons with different numbers of nodes $k$. For $k = 0$, this dependence is indistinguishable from its variational counterpart (3.5) with $D = 1$. Stable and unstable portions of the soliton families are shown by black and green curves, respectively. (d) Stability (white) and instability (shaded) domains in the $(\alpha, b)$ plane for 1D solitons with $k = 5$. The fan-shaped structure is a manifestation of the scaling invariance of Eq. (3.1).

The 1D solitons are remarkably robust. The computation of stability eigenvalues demonstrates that the modes with $k = 0,1,2$ are stable at least up to $b = -40$ [in particular, this fact implies the stability of the exact solution (3.4); it was checked that the exact solution (3.3) is stable as well]. Only the families of higher-order solitons with $k \geq 3$ feature instability domains alternating with stability areas. The structure of the instability and stability domains becomes more complex with the increase of $k$; see Fig. 3.1(d) for $k = 5$. We did not find any limit on the number of nodes possible in stable 1D solitons, hence even very complex structures with $k \geq 10$ may be stable. Direct simulations of the evolution of the perturbed solitons verify the predictions of stability analysis: While stable solitons keep their shape over distances far exceeding $\xi = 10^3$, their unstable counterparts transform into irregularly breathing modes that remain tightly confined (see the top row in Fig. 3.2).

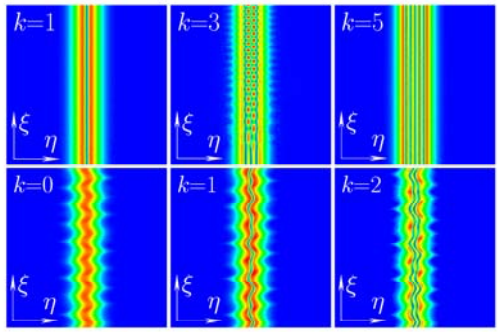


Figure 3.2. Top row: Contour plots of $\left|q\left(\eta,\xi\right)\right|$ demonstrating the stable propagation of the perturbed 1D soliton with $k = 1$, $b = -10$ (left-hand side), instability of the one with $k = 3$, $b = -10$ (center), and stability of the complex mode with $k = 5$, $b = -13$ (right-hand side). Bottom row: Oscillations of 1D solitons with $k = 0,1,2$, $b = -20$, after the application of phase tilt $\theta = 1.5$.

The physically relevant definition of solitons includes their ability to maintain the intrinsic coherence in the state of motion and upon mutual collisions. Solitons may be set in motion by multiplying them by a factor $\exp\left(i\theta\eta\right)$, with the phase tilt $\theta$. As a result, both 1D and 2D solitons start regular oscillations (see examples for 1D solitons with $k = 0,1,2$ in the bottom row of Fig. 3.2) – somewhat similar to the matter-wave solitons in the cigar-shaped traps [131], with a difference that the nonlinearity is defocusing in the present setting, and solitons oscillate in the effective nonlinear potential. An equation of motion for the

vectorial coordinate $\vec{R}(\xi)$ of the soliton center can be readily derived in the quasi-particle approximation

$$\frac{d^2\vec{R}}{d\xi^2} = -2\alpha\left(\alpha/\pi\right)^{D/2} U_D \exp\left(2\alpha R^2\right)\vec{R}, \tag{3.6}$$

where $D = 1,2$ (here $U_D$ is the soliton norm). As follows from Eq. (3.6), the squared frequency of small-amplitude oscillations of the kicked soliton is $\omega_D^2 = 2\alpha\left(\alpha/\pi\right)^{D/2} U_D + \left(3\alpha/2\right)\theta^2$, which was found to be in virtually exact agreement with the results of numerical simulations. Furthermore, we applied opposite kicks to two lobes of a 1D dipole, thus initiating oscillations and the recurrent collisions of two solitons with opposite signs. It was found that solitons keep bouncing from each other elastically. Assuming an instantaneous rebound, Eq. (3.6) also predicts the frequency of the periodic collisions very accurately. Thus, both 1D and 2D solitons are robust quasi-particle objects that maintain their intrinsic coherence and interact elastically in the course of their motion.

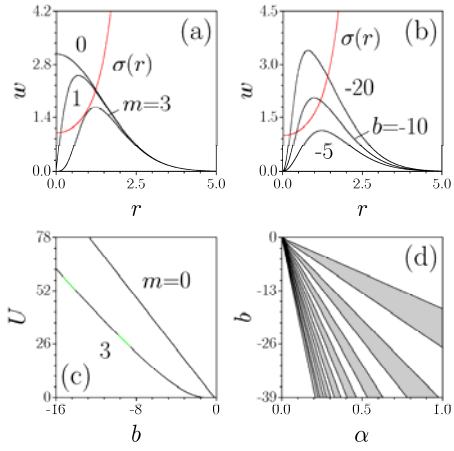


Figure 3.3. Profiles of 2D solitons: (a) for $b = -10$ and the different vorticities $m$; (b) for $m = 2$ and the different values of $b$. (c) $U$ vs $b$ for different $m$ [the curve for $m = 0$ is indistinguishable from the variational result (3.5) with $D = 2$]. Stable and unstable portions of the soliton families are shown by black and green curves, respectively. (d) The lowest stability (white) and instability (shaded) domains in the $(\alpha, b)$ plane for vortex solitons with $m = 2$. The fan-shaped structure is a manifestation of the scaling invariance of Eq. (3.1).

The 2D version of the model (3.1), (3.2) gives rise to vortex solitons $q(r,\xi) = w(r)\exp(im\phi + ib\xi)$ for all integer values of topological charge $m$; see

Figs. 3.3(a) and 3.3(b). For the same reason as in 1D, the vortices with different $m$, while having completely different asymptotic forms at $r \to 0$, become identical at $r \to \infty$ (in contrast to vortex solitons in focusing media, which considerably broaden with the increase of the topological charge [14]). The increase of $|b|$ results in a gradual contraction of the vortex rings toward $r = 0$ [Fig. 3.3(b)]. The energy flow (norm) carried by the 2D solitons at fixed $b$ decreases with the increase of $m$ [Fig. 3.3(c)], similar to the 1D case [cf. Fig. 3.1(c)].

Another essential result is that, due to the defocusing character of the nonlinearity, azimuthal instabilities, which are fatal for vortex solitons in focusing media [14], are suppressed in our system. We have found that solitons with $m = 0$ and $m = 1$ [including the 2D exact solution (3.4)] are completely stable, while vortices with $m > 1$ give rise to a complex structure of stability and instability domains. This structure can be obtained upon substitution of the perturbed solution $q = \left[w(r) + u\left(r\right)\exp\left(in\phi + \delta\xi\right) + \mathrm{v}^*\left(r\right)\exp\left(-in\phi + \delta^*\xi\right)\right]\exp\left(im\phi + ib\xi\right)$, where $n$ is the azimuthal perturbation index and the functions $u, \mathrm{v}$ describe small perturbations, into Eq. (3.1) and its subsequent linearization, that leads to the following linear eigenvalue problem for the perturbation profiles and growth rates $\delta$:

$$\begin{aligned} i\delta u &= -\frac{1}{2}\left(\frac{d^2}{dr^2} + \frac{1}{r}\frac{d}{dr} - \frac{\left(m+n\right)^2}{r^2}\right)u + bu + \sigma w^2\left(\mathrm{v} + 2u\right), \\ i\delta \mathrm{v} &= \frac{1}{2}\left(\frac{d^2}{dr^2} + \frac{1}{r}\frac{d}{dr} - \frac{\left(m-n\right)^2}{r^2}\right)\mathrm{v} - b\mathrm{v} - \sigma w^2\left(u + 2\mathrm{v}\right). \end{aligned} \qquad (3.7)$$

The structure of the stability domains is displayed in Fig. 3.3(d) for vortices with $m = 2$ that can be destroyed by the perturbations with $n = 2$ at certain values of $b$ (similarly, at $m > 2$ the most destructive perturbations pertain to $n = m$, $m \pm 1$). Note that the stability and instability domains are equidistantly spaced in $b$. We stress that conspicuous stability regions have been found for all considered values of topological charge $m$.

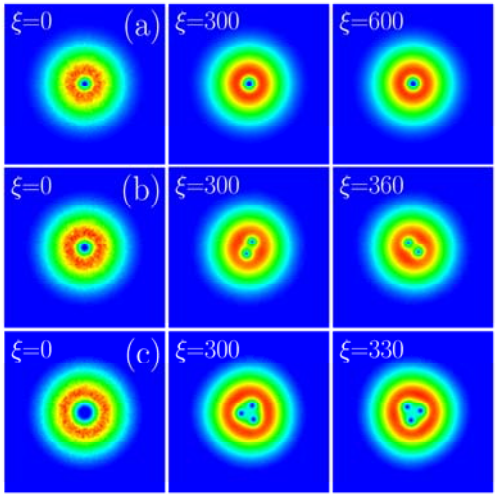


Figure 3.4. (a) Stable propagation of the perturbed vortex soliton with $m=2$, $b=-17$. (b) Splitting of the unstable double vortex $\left(m=2\right)$ with $b=-11$ into a steadily rotating pair of unitary vortices. (c) Splitting of the unstable vortex with $m=3$, $b=-9$ into a rotating set of three vortices.

An example of stable evolution of the perturbed vortex ring, which keeps its structure over indefinitely long distances, is shown in Fig. 3.4(a). Unstable vortex solitons (with $m\geq 2$) tend to split into $m$ separate unitary vortices, staying in the vicinity of point $\eta,\zeta=0$ and performing a persistent rotation around it, which is a consequence of the conservation of the angular momentum. Examples of such evolution dynamics for $m=2$ and 3 are displayed in Figs 3.4(b) and 3.4(c).

### 3.2. Algebraic Bright Solitons Supported by Defocusing Nonlinearities, growing toward the Periphery as $\left(1+\left|r\right|^{\nu}\right)$

In previous section it was shown that a spatially inhomogeneous defocusing nonlinearity whose strength grows toward the periphery does support bright solitons in the conservative media. Here we address the value of minimal growth rate of the defocusing nonlinearity at $r\to\infty$, which is necessary for the existence of bright solitons. For this purpose we consider an algebraic modulation profile of the defocusing nonlinearity in the form $\sigma(r)\sim\left(1+\left|r\right|^{\nu}\right)$. As we will show below in this nonlinearity landscape the algebraic fundamental, multipole, and vortex solitons in one- and two-dimensional geometries could exist.

Let us consider the propagation of light in the nonlinear medium governed by the Eq. (3.1), where the nonlinearity landscape is described by $\sigma\left(\vec{r}\right)=1+\kappa\left|r\right|^{\nu}$ and $\kappa=1$ can be fixed by scaling. We will vary the power $\nu$ in the above mentioned expression. As in the Section 3.1 1D and 2D soliton solutions of Eq. (3.1) are searched in the form $q\left(r,\xi\right)=w(r)\exp\left(im\phi+ib\xi\right)$ (in 1D case, the term $\exp\left(im\phi\right)$ is omitted). The examples of 1D and 2D fundamental and higher-order modes, including vortices and 1D multipole soliton with $k=2$ nodes, that feature bright localized shapes despite the defocusing character of the nonlinearity, are shown in Fig. 3.5.

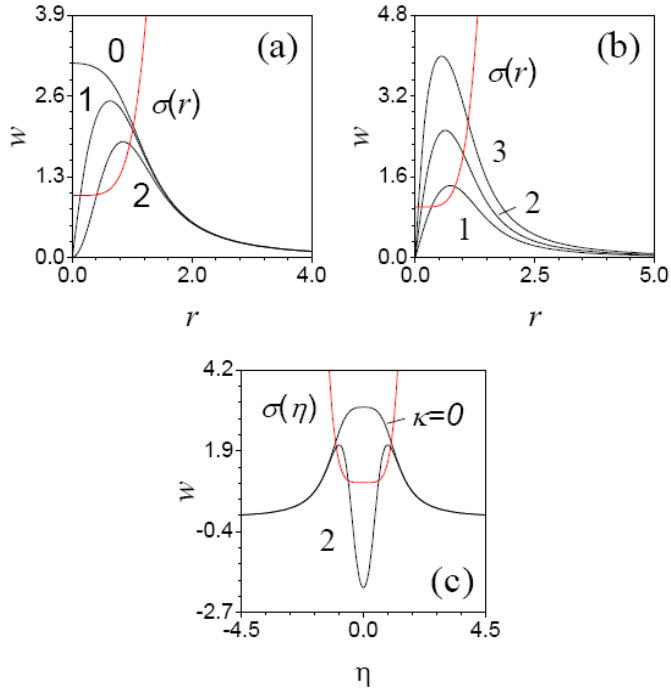


Figure 3.5. (a) Profiles of 2D solitons with different topological charges corresponding to $b=-10$, $\nu=5$. (b) Vortices with $m=1$ corresponding to $b=-5,-10,-20$ (curves 1, 2, 3). (c) 1D solitons with different numbers of nodes corresponding to $b=-10$, $\nu=5$. In each panel, the nonlinearity profile is shown by the red curve.

The shapes of the fundamental solitons in the frames of current model can be accurately predicted by the Thomas-Fermi approximation, which neglects the diffraction term in Eq. (3.1) and allows to obtain the solution $w_{TF}^{2}=-b\Big/\left(1+\left|r\right|^{\nu}\right)$. This approximation yields asymptotically exact algebraic tails of the solitons of all types, irrespective of the topological charge (the Thomas-Fermi profiles of the 2D and 1D fundamental solitons are nearly indistinguishable from their numerical

counterparts displayed in Fig. 3.5). To the best of our knowledge, the vortices with the algebraically decaying tails have not been reported before in the conservative media, although they are known in Bose-Einstein condensates in dissipative settings [132]. In contrast to the conventional bright solitons, in the setting considered here the decay rate of soliton tails does not depend on $b$ and is determined solely by the nonlinearity modulation rate $\nu$. The center of the soliton is always located at the minimum of the defocusing nonlinearity at $r = 0$. The increase of $|b|$ entails the increase of the soliton amplitude (in agreement with the Thomas-Fermi approximation), and a weak contraction of the vortex ring. Further, an expansion of the soliton profile near the maximum point $w = w_{\max}$ at $r = r_{\max}$ (for the fundamental solitons, $r_{\max} = 0$), yields $b \le -\left(1 + r_{\max}^{\nu}\right) w_{\max}^2$, hence solitons exist only for $b \le 0$, as predicted by the Thomas-Fermi approximation too.

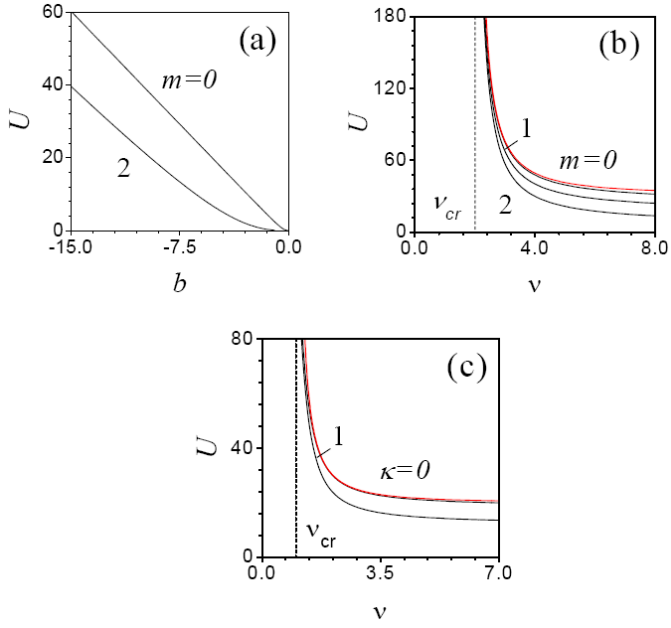


Figure 3.6. The energy flow versus the propagation constant, $b$, for 2D solitons at $\nu = 5$ (a), and versus $\nu$ for 2D (b) and 1D (c) solitons at $b = -10$. Red curves in (b) and (c) show the prediction of the Thomas-Fermi approximation.

The soliton families are characterized by the energy flow (norm), $U = \int |q|^2 \, d\vec{r}$. For the fundamental solitons, the Thomas-Fermi approximation predicts $U_{TF} = 2\pi^D |b| / \left[\nu \sin\left(\pi D / \nu\right)\right]$, which, in particular, explains the linear dependence $U(b)$ in Fig. 3.6(a). As in the case of the medium with anti-Gaussian nonlinearity landscape, the vortex solitons in 2D case and multipoles in 1D case always feature smaller norms than the corresponding fundamental solitons. At

fixed $b$ the soliton energy flow monotonically increases with the decrease of $\nu$ (this is accompanied by the progressive soliton expansion in the transverse plane) and diverges when $\nu$ approaches the critical value $\nu_{cr}$ [see Fig. 3.6(b) for 2D solitons and Fig. 3.6(c) for 1D solitons]. Importantly, this critical value is directly linked with the number of transverse dimensions $D$ in the problem. One finds that $\nu_{cr} = D$. This result is in agreement with the prediction of the Thomas-Fermi approximation where $U_{TF} \to \infty$ at $\nu \to D$. Thus, steeper defocusing-nonlinearity landscapes are required for the existence of bright solitons in higher dimensions.

A key issue is the stability of the obtained soliton solutions. As before, in the 2D case the linear stability analysis was performed by substituting the perturbed field in the form $q(r,\xi) = \left[w(r) + u(r)\exp(in\phi + \delta\xi) + \mathrm{v}^*(r)\exp(-in\phi + \delta^*\xi)\right]\exp(im\phi + ib\xi)$ into nonlinear Schrodinger equation. Then the eigenvalue problem for perturbation growth rates $\delta$ was obtained as in the Section 3.1 [see Eq. (3.7)].

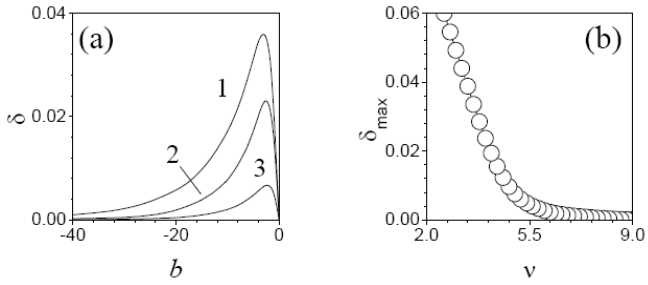


Figure 3.7. (a) The real part of the perturbation growth rate versus $b$ at $\nu = 3.5, 4,$ and 5 (curves 1, 2, and 3) for vortices with $m = 1$ and perturbation index $n = 1$. (b) The largest perturbation growth rate for the vortex with $m = 1$ versus $\nu$.

The results of linear stability analysis for 2D solitons are summarized in Fig. 3.7. The fundamental solitons are always stable. While the vortex solitons with topological charges $m = 1$ are weakly unstable at $\nu \to \nu_{cr}$ with respect to perturbations with $n = 1$, they become stable with the increase of $b$. At moderate $\nu$ values the perturbation growth rate acquires maximum at moderate $b$ value and then it asymptotically vanishes when $b \to -\infty$ [Fig. 3.7(a)]. Already at $\nu = 5$ the vortex with $b = -30$ is a completely stable object. The maximal possible perturbation growth rate (determined over all $b$ values) also rapidly diminishes with the increase of $\nu$ [Fig. 3.7(b)]. Already at $\nu \sim 8$ the entire family of the vortex solitons may be considered stable. A similar picture was found for $m = 2$ vortex solitons, although such states usually require larger rates $\nu$ of nonlinearity growth for their stabilization. 1D fundamental solitons are also stable, while the

stabilization of multipole solitons is achieved for moderate values $\nu \sim 5, 6$ (the larger is the number of the azimuthal nodes, the larger is the $\nu$ value required for the stabilization).

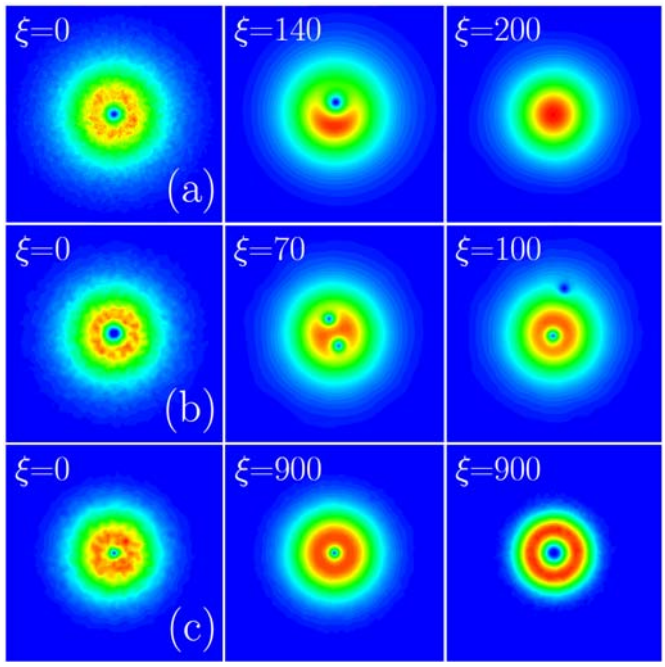


Figure 3.8. (a) A decay of the unstable vortex with $m = 1$, $b = -3$, $\nu = 3.5$. (b) A decay of the unstable vortex with $m = 2$, $b = -20$, $\nu = 4$. (c) The stable propagation of vortex with $m = 1$, $b = -30$, $\nu = 5$ (left, center) and vortex with $m = 2$, $b = -15$, $\nu = 10$ (right). In all cases, the white noise was added to the input field distributions.

The results of stability analysis were verified by the direct simulations of Eq. (3.1). Figure 3.8(a) shows a typical decay scenario for the unstable vortex with $m = 1$ that develops the azimuthal modulations and then transforms into a fundamental soliton, while the phase singularity is expelled to $r \to \infty$. In the unstable vortex with $m = 2$, the central singularity may split into two singularities, which is followed by the expulsion of one of them, while the other singularity stays at the center, developing into a stable vortex with $m = 1$ [Fig. 3.8(b)]. The examples of stable propagation of perturbed vortices with charges $m = 1$ and 2 are displayed in Fig. 3.8(c). One can see that the stable modes preserve their internal structure over indefinitely long distances even in the presence of strong input perturbations.

### *3.3. Stable Bright and Vortex Solitons in the Photonic Crystal Fibers with Inhomogeneous Defocusing Nonlinearity*

In two previous Sections of this Chapter the nonlinearity grew continuously from the center of the material toward its periphery. Here more complex nonlinearity landscape is considered, where the local nonlinearity varies in the transverse plane in a step-like fashion, resulting in the alternation of the narrow defocusing areas with linear domains. Such nonlinearity landscapes may be realized in photonic-crystal fibers whose strands are selectively filled by the refractive-index-matching materials with suitable defocusing nonlinearities. In particular, the liquid-infiltrated photonic-crystal fibers represent an example of material where such complex nonlinearity landscapes can be realized [133, 134].

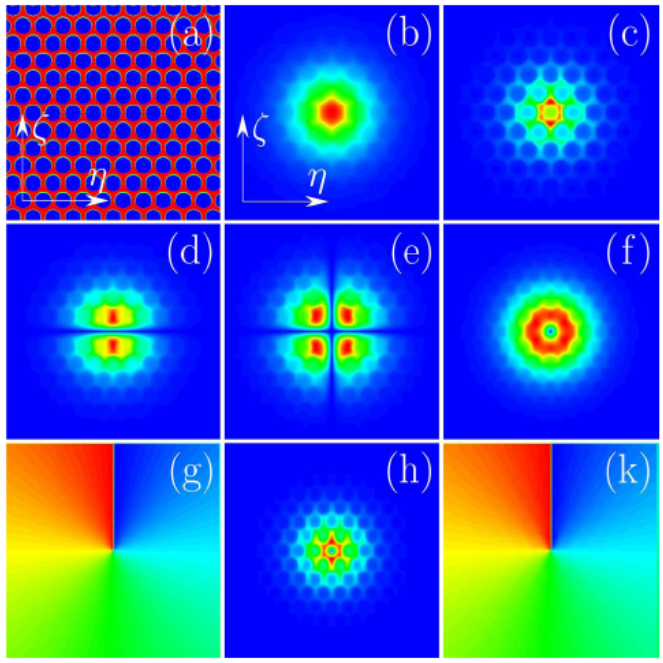


Figure 3.9. (a) The cross section of the photonic crystal fiber, where the core is shown by red and the filled strands are shown by blue. A distribution of the absolute value of the field for fundamental solitons with (b) $b=-1$ and (c) $b=-6$, (d) a dipole soliton with $b=-2$, (e) a quadrupole soliton with $b=-2$, and (f) vortex solitons with topological charge 1 and $b=-1$ or (h) $b=-4$. Panels (g) and (k) show the phase distributions for vortex solitons depicted in (f) and (h), respectively. In all cases $\sigma_c=0$.

To address the propagation of light beams along the $\xi$-axis in a medium with a uniform linear refractive index and transverse modulation of the Kerr nonlinearity we use the following version of the nonlinear Schrödinger equation for the dimensionless field amplitude $q$:

$$i\frac{\partial q}{\partial \xi} = -\frac{1}{2}\Delta q - \sigma\left(\eta, \zeta\right)\left|q\right|^2 q\,. \qquad (3.8)$$

We assume here that the nonlinearity landscape, which depends on both transverse coordinates, is implemented using photonic crystal fiber, whose holes are arranged into the perfectly periodic hexagonal structure [see Fig. 3.9(a)]. The holes are filled with index-matched defocusing materials so that the nonlinearity coefficient in the central hole is $\sigma\left(\eta = \zeta = 0\right) = -1$, and its value grows toward the photonic crystal fiber periphery as $\sigma\left(\eta, \zeta\right) = -\exp\left(\alpha r_{km}\right)$, where $r_{km}$ is the distance between the center of the hole with indices $k, m$ and the photonic crystal fiber axis located at $\eta, \zeta = 0$. The photonic crystal fiber core material may also be nonlinear, with $\sigma = \sigma_c$. We consider only the case of linear or focusing core material, with $\sigma_c \geq 0$. Here we set the hole-to-hole separation in the fiber to $d = 1.5$, the hole radius to $r_0 = 0.6$, and the rate of the nonlinearity growth to $\alpha = 1.5$, but we verified that the results remain qualitatively similar for other values of these parameters.

We search for soliton solutions of Eq. (3.8) in the form $q\left(\eta, \zeta, \xi\right) = w\left(\eta, \zeta\right)\exp\left(ib\xi\right)$, where the function $w\left(\eta, \zeta\right)$ is real for bright solitons and complex for the vortex modes. In the case of uniform defocusing nonlinearity $\left(\alpha = 0\right)$ bright solitons exist only if the nonlinearity of the host photonic crystal fiber is focusing, with $\sigma_c > 0$. Such solitons exhibit a ring-like shape because light is expelled from the central hole containing the defocusing medium into the surrounding focusing area. Such solitons are unstable, as they collapse upon propagation.

For a nonzero growth rate of the defocusing nonlinearity, $\alpha > 0$, different families of bright fundamental, multipole, and vortex solitons exist for $\sigma_c \geq 0$. The illustrative examples are shown in Fig. 3.9. All such solitons feature a strong small-scale shape modulation, reflecting the underlying photonic crystal fiber structure, and cover multiple holes of the fiber. This modulation is most pronounced for high powers, when the light is expelled from the holes into the host material. Note that all solitons shown in Fig. 3.9 were obtained for $\sigma_c = 0$, that is, for a linear host material. Remarkably, even in this case the light field remains localized around the center of the fiber. We also found solitons for an algebraic modulation law of the local defocusing nonlinearity in the holes, $\sigma\left(\eta, \zeta\right) = -1 - r_{km}^{2+\varepsilon}$, with $\varepsilon > 0$, similar to the results presented above in Section 3.2 for a continuous medium. In this case, the slower nonlinearity growth rate results in a weaker soliton localization.

The fundamental solitons exist at negative values of the propagation constant, namely, $b^{low} \le b < 0$ [see Fig. 3.10(a)], with the energy flow being a monotonically decreasing function of $b$ with $U \to 0$ at $b \to 0$. In contrast, at $b = b^{low}$ the tangential line to the $U(b)$ curve becomes vertical, although $U$ remains finite at $b = b^{low}$. Thus, the energy flow of the fundamental solitons is limited by the value $U_m = U\left(b = b^{low}\right)$. The cut-off $b^{low}$ depends on the nonlinearity strength $\sigma_c$ of the host material [Fig. 3.10(b)]. The smaller $\sigma_c$ the broader the existence domain, while $b^{low} \to -\infty$, $U_m \to \infty$ when $\sigma_c \to 0$ [Fig. 3.10(c)]. Thus, while structures with a focusing host material support fundamental solitons with limited energy flows, there is no limitation on the energy flow in the case of photonic crystal fiber made of a linear material.

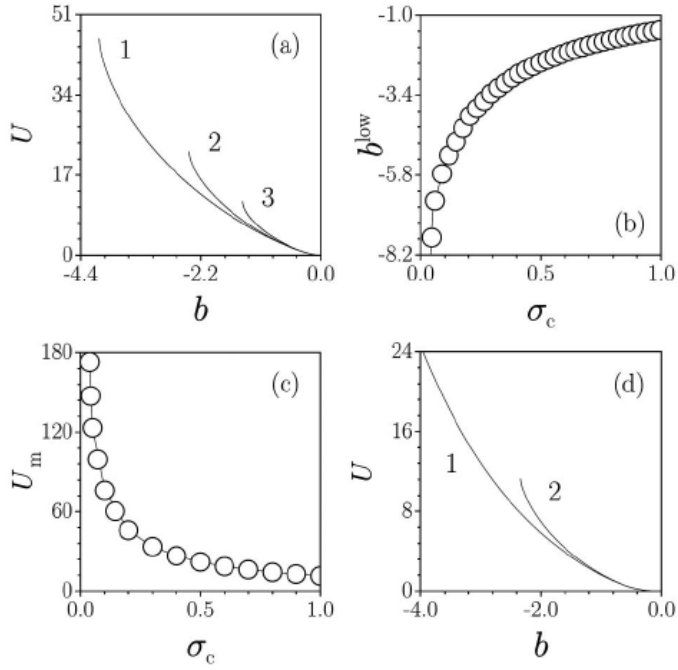


Figure 3.10. (a) The energy flow of the fundamental solitons versus the propagation constant at $\sigma_c = 0.2$ (curve 1), 0.5 (curve 2), and 1.0 (curve 3). (b, c) The lower cutoff and the corresponding energy flow $U_m = U\left(b = b^{low}\right)$ versus the nonlinearity of the host material. (d) The energy flow of the vortex solitons versus the propagation constant at $\sigma_c = 0$ (curve 1) and $\sigma_c = 1$ (curve 2).

Note that at $\sigma_c = 0$ an increase of $U$ leads to a gradual concentration of light in the linear medium, as is visible by comparing Figs. 3.9(b) and 3.9(c). The soliton width monotonically decreases with a decrease of $b$ (i.e., an increase of

$|b|$). The cutoff value is also found to depend on the radius $r_0$ of the photonic crystal fiber holes. When $r_0$ decreases, the cutoff $b^{low}$ monotonically increases, while the respective largest energy flow $U_m$ decreases. For all parameters fixed, the cutoff $b^{low}$ is a monotonically decreasing function of the nonlinearity growth rate $\alpha$. To understand the origin of the existence of limiting energy flow $U_m$ one should note that the largest part of the energy flow of soliton shown in Fig. 3.9(c) is carried by the host material. Therefore, self-focusing $(\sigma_c > 0)$ leads to a collapse at $U = \sigma_c^{-1} U_T$, where the collapse threshold at $\sigma_c = 1$ may be estimated as the norm of the Townes soliton [4], $U_T \approx 5.85$. The resulting estimate $U_m \approx 5.85/\sigma_c$ is consistent with Fig. 3.10(c).

The similar results were obtained for the other types of the localized modes, including multipole and vortex solitons. For example, the typical dependencies $U(b)$ for single-charged vortex solitons are presented in Fig. 3.10(d) for the cases when $\sigma_c = 0$ and $\sigma_c > 0$.

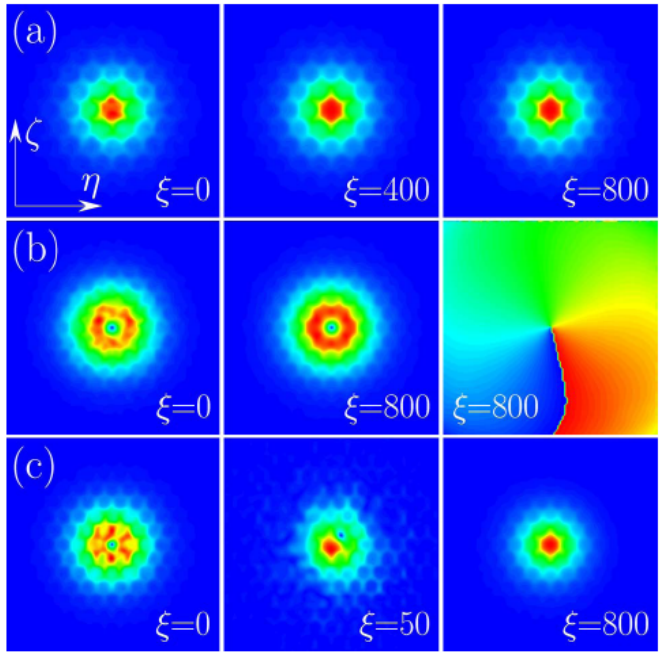


Figure 3.11. (a) The stable propagation of the perturbed fundamental solitons with $b = -2$ and (b) the vortex soliton with $b = -1$, and (c) a decay of an unstable vortex with $b = -2$ into a stable fundamental soliton. The distributions of the absolute value of the field are shown at the different propagation distances. For the stable vortex soliton, the final phase distribution is also shown. In all cases $\sigma_c = 0$.

To check the stability of the stationary soliton families, we studied their propagation up to the large distances $\xi \sim 10^4$ in the presence of significant input perturbations of the exact soliton profiles. The fundamental solitons are found to be stable in their entire existence domain. In this case the perturbed inputs reshape and then propagate in a stable way over indefinitely long distances [Fig. 3.11(a)]. On the other hand, the dipole and quadrupole solutions were found to be always unstable. In the course of the propagation, they exhibit fast reshaping into fundamental solitons. The single-charge vortex solitons were found to be stable inside a finite domain $b^{st} \le b < 0$. An example of the stable propagation of such vortex soliton is shown in Fig. 3.11(b). Outside the stability domain, that is, at $b < b^{st}$, the vortex solitons reshape and decay into the fundamental ones [Fig. 3.11(c)]. Their stability border is $b^{st} \approx -1.48$ at $\sigma_c = 0$, and $b^{st} \approx -1.33$ at $\sigma_c = 1$; that is, the stability domain shrinks with the increase of the strength of the focusing nonlinearity of the host material.

To study the robustness of the solutions against finite-size effects in the infiltrated photonic crystal fibers, we studied the truncated structures where the strength of the defocusing nonlinearity inside the holes grows only for $0 \le r_{km} \le r_{\max}$, while at $r_{km} > r_{\max}$ it saturates at the level of $\sigma = \sigma\left(r_{\max}\right)$. As expected on the physical grounds, the input solutions quickly diffract for small values of $r_{\max}$. However, already for $r_{\max} = 5d$ they retain their shape for more than 200 diffraction lengths without considerable distortions.

### *3.4. Summary*

In this Chapter it was illustrated that, in contrast to common expectations, the defocusing nonlinearity, without any additional linear potential, may support the families of stable bright solitons in one and two dimensions, provided that the nonlinearity strength increases rapidly enough from the center to the periphery of the material.

First of all, the materials with nonlinearity strength growing exponentially toward the periphery were addressed. In such medium one can obtain not only fundamental, but also a variety of stable higher-order bright solitons, including 1D multipoles and 2D vortex rings with all values of the topological charge. When such solitons are set in motion then perform the persistent oscillations around a minimum of the nonlinearity landscape and can interact elastically.

If the defocusing nonlinearity strength varies as $\left(1 + \left|r\right|^{\nu}\right)$, the stable bright solitons with algebraic tails may exist. Not only fundamental solitons, but also stable algebraic vortex and 1D multipole states were encountered. The energy

flow of such solitons converges as long as the nonlinearity growth rate in the medium exceeds the dimensionality of the problem.

Finally, we have shown that the stable 2D fundamental and vortex solitons may exist in the infiltrated photonic crystal fibers with an inhomogeneous defocusing nonlinearity without any modulation of the linear refractive index. Such solitons possess strongly modulated shapes and they exist even if the core material of the photonic crystals fiber is linear.

The main results summarized in this chapter have been published in the following journals:

1. **O.V. Borovkova**, Y.V. Kartashov, L. Torner, and B.A. Malomed, "Bright solitons from defocusing nonlinearities," Phys. Rev. E **84**, 035602 (2011).
2. **O.V. Borovkova**, Y.V. Kartashov, B.A. Malomed, and L. Torner, "Algebraic bright and vortex solitons in defocusing media," Opt. Lett. **36**, 3088-3090 (2011).
3. V.E. Lobanov, **O.V. Borovkova** a, Y.V. Kartashov, B.A. Malomed, and L. Torner "Stable bright and vortex solitons in photonic crystal fibers with inhomogeneous defocusing nonlinearity," Opt. Lett. **37**, 1799-1801 (2012).

# Chapter 4. 1D Dissipative Solitons in Media with Inhomogeneous Gain and Losses

Spatial solitons are usually studied in conservative systems where nonlinearity is to compensate diffraction. However, if a simultaneous balance between diffraction and nonlinearity on the one hand, and between gain and losses on the other hand is achieved, then a dissipative soliton may form. In this chapter we consider dissipative solitons in two types of the engineered materials with transversally inhomogeneous gain and/or absorption. First we show that stable dissipative fundamental and higher-order solitons may form in both self-focusing and self-defocusing media with uniform gain and nonuniform absorption whose strength grows rapidly enough toward the periphery of the system. Two types of absorption landscapes have been investigated: a single-well and a double-well. Second we show that stable spatial solitons can be supported by localized cubic gain competing with uniform linear losses in a cubic-quintic nonlinear medium.

### *4.1. Solitons in Nonlinear Media with Uniform Linear Gain and Nonuniform Cubic Losses*

Stabilization of dissipative solitons may be achieved in systems where higher-order absorption compensates a spatially localized gain. However, an important question arises: Can the spatial shape of the absorption instead of gain be used for the generation and stabilization of new types of dissipative solitons? It is commonly believed that an uniform linear gain destabilizes all localized soliton

states. However, we show that the stable one-dimensional dissipative solitons do exist in nonlinear media with uniform gain in the presence of nonuniform cubic losses whose local strength grows with the transverse coordinate $\eta$ faster than $|\eta|$. In principle, such model may be realizable in Optics by combining a spatially uniform gain and an inhomogeneous doping with two-photon-absorbing elements. Experimental techniques allowing the creation of potentially suitable dopant concentration profiles have been developed in other contexts, such as in lithium niobate channel waveguides [130].

The equation describing light propagation in a nonlinear medium with inhomogeneous amplification and losses was introduced in the Introduction [see Eq. (1.9)]. Here we analyze the one-dimensional variant of such equation describing the propagation of a light beam in a material with uniform gain and nonuniform cubic losses, whose local strength grows with a transverse coordinate:

$$i\frac{\partial q}{\partial \xi} = -\frac{1}{2}\frac{\partial^2 q}{\partial \eta^2} + \sigma |q|^2 q + ip_i q - i\gamma(\eta)|q|^2 q\,. \tag{4.1}$$

The nonlinearity of material is described by the term $\Sigma(q) = \sigma |q|^2 q$, where $\sigma = -1, 0, +1$ corresponds to a focusing, zero, or defocusing Kerr nonlinearity, respectively. The dissipative terms, $P(q) = p_i q$ and $\Gamma(q) = \gamma(\eta)|q|^2 q$, with $p_i > 0$ and $\gamma(\eta) > 0$ account for the uniform linear gain and the inhomogeneous nonlinear absorption. Solitons are sought for as $q(\eta, \xi) = w(\eta)\exp(ib\xi)$, where $w(\eta) = w_r(\eta) + iw_i(\eta)$ is a complex function satisfying the stationary equation,

$$-(b + ip_i)w = -\frac{1}{2}\frac{d^2 w}{d\eta^2} + [\sigma - i\gamma(\eta)]|w|^2 w. \tag{4.2}$$

We start with the consideration of the simplest setting where the strength of the nonlinear absorption in Eqs. (4.1) and (4.2) grows towards the periphery as

$$\gamma(\eta) = \gamma_0 \exp(\kappa\eta^2), \tag{4.3}$$

so that $\gamma(\eta)$ has a single minimum at the center (a single-well absorption profile). By using the scaling transformations one can always set $\kappa = 1$ and keep the strength of the two-photon absorption, $\gamma_0$, as a free parameter. In this case Eq. (4.2) admits an exact dipole-soliton solution at $\sigma = 0$ and $p_i = 3/2$:

$$w(\eta) = \gamma_0^{-1/2}\eta \exp[-(1-i)\eta^2/2], \tag{4.4}$$

with propagation constant $b = -3/2$, which is unstable.

At the same time, Eq. (4.2) has also the exact stable fundamental solution at $p_i = 1/2$ and $b = -1/2$

$$w(\eta) = \gamma_0^{-1/2} \exp\left[-(1-i)\eta^2/2\right], \tag{4.5}$$

if the nonlinear absorption modulation profile is

$$\gamma(\eta) = \gamma_0 \eta^2 \exp(\eta^2), \tag{4.6}$$

instead of (4.3).

These two examples illustrate the crucially important property of this model: namely, the nonlinearizability of Eqs. (4.1) and (4.2) due to the rapid growth of the nonlinear absorption at $|\eta| \to \infty$, which means that the asymptotic form of stationary solutions cannot be found using the formal linearization of Eq. (4.2). The nonlinearizability of governing equation far from a soliton center explains why the uniform linear gain does not imply the exponential growth of field in low-intensity regions (that would lead to the instability).

Numerical solutions of Eqs. (4.2), (4.3) reveal that the single-well absorption landscape gives rise to fundamental solitons with symmetric and asymmetric profiles, i.e., to the effect of the spontaneous symmetry breaking, if the conservative part of cubic nonlinearity is focusing $(\text{i.e., } \sigma = -1)$. Surprisingly, bright solitons in this setting may exist even in the case of zero or defocusing conservative nonlinearities $(\sigma = 0, +1)$, although in these two cases the solitons always feature symmetric shapes.

Figure 4.1 shows the generic examples of stationary solitons in the focusing and defocusing media with the single-well nonlinear-absorption profile, depicted by the red curves. In the case of the focusing nonlinearity, the family of asymmetric solitons bifurcates from the symmetric one with the increase of the linear gain, $p_i$, at the spontaneous symmetry breaking (critical) point, $p_i = p_i^{cr1}$. The bifurcation is presented in Figs. 4.2(a) and 3.2(b), where the energy flow, $U = \int_{-\infty}^{+\infty} |q|^2 \, d\eta$, and propagation constant $b$ are shown versus the gain parameter, $p_i$.

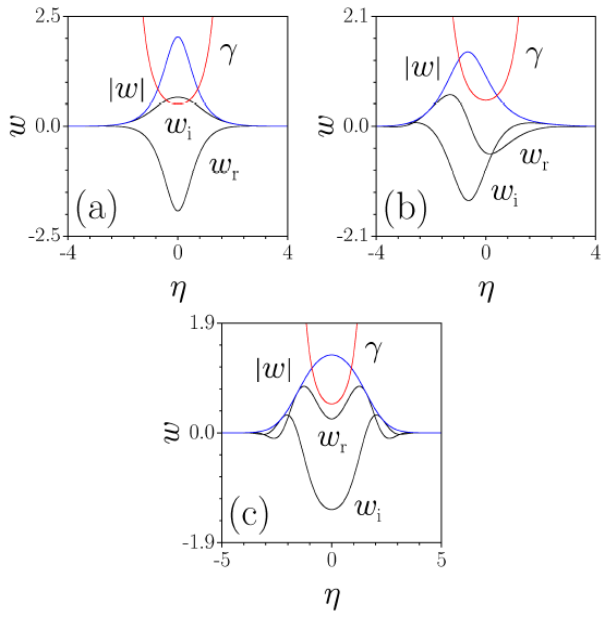


Figure 4.1. Typical profiles of fundamental symmetric (a) and asymmetric (b) soltions in the focusing medium, and of the symmetric one in the defocusing medium (c) with the single-well nonlinear-absorption profile (4.3) [red curves for $\gamma\left(\eta\right)$], at $p_i = 1.5$, $\gamma_0 = 0.5$.

While the spontaneous symmetry breaking is a common feature of double-well systems [135, 136], including dissipative ones [137], it seems more surprising in the present setting, based on the single-well absorption landscape. In this connection, it is worthy to mention that a similar spontaneous symmetry breaking of solitons was reported also in a model combining the self-focusing nonlinearity, uniform cubic loss, and a localized region of linear gain [73]. Another noteworthy feature of the present setting is that, even in the case of the focusing nonlinearity, the propagation constant $b$ can be negative, while focusing nonlinearity in settings with uniform gain and absorption usually gives rise to solitons with $b > 0$ (bright solitons with $b < 0$ are possible in media featuring a localized linear gain against the background of uniform linear loss [72]). Actually, symmetric solitons in Fig. 4.2(b) feature negative $b$ only at small values of the gain, while the asymmetric branch plunges into the region of $b < 0$ with the increase of $p_i$. The above-mentioned nonlinearizability of the underlying equation (4.1) is a fundamental reason for the existence of the solitons with $b < 0$.

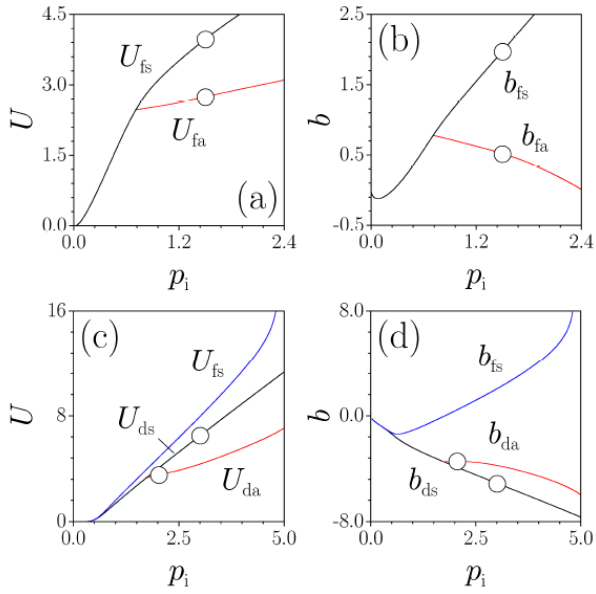


Figure 4.2. The energy flow (a) and propagation constant (b) versus $p_i$ for symmetric ("fs") and asymmetric ("fa") fundamental solitons in the focusing medium with the single-well nonlinear-absorption profile (4.3) at $\gamma_0 = 0.5$. (c), (d): The same for dipole solitons in the double-well nonlinear-absorption landscape (4.6) at $\gamma_0 = 2.0$. Subscripts "fs", "ds", and "da" denote symmetric dipoles in the focusing and defocusing media, and asymmetric dipoles in the defocusing medium, respectively. Circles in (a) and (b) correspond to the solitons in Figs. 4.1(a) and 4.1 (b), while circles in (c), (d) pertain to the solitons in Figs. 4.4 (a) and (b), respectively.

The dependence of the critical value of gain, at which the spontaneous symmetry breaking of the fundamental solitons occurs, on the strength of the nonlinear absorption is shown in Fig. 4.3(a). The asymmetric solitons, which are always stable, exist above this curve, while the symmetric ones are found in the entire $\left(\gamma_0, p_i\right)$ plane, but they are stable only beneath the curve, being unstable where they coexist with the asymmetric solitons (the stability of solitons was inspected by calculating the respective eigenvalues for small perturbations). The latter property complies with the fact that the bifurcation observed in Figs. 4.2(a) and 4.2(b) is of the supercritical type (in other words, it is a phase transition of the second kind).

The family of symmetric solitons that exists in the medium with the defocusing or zero conservative part of nonlinearity is completely stable, featuring no spontaneous symmetry breaking. The energy flow of such modes increases almost literally with the gain, while the corresponding propagation constant decreases, always staying negative.

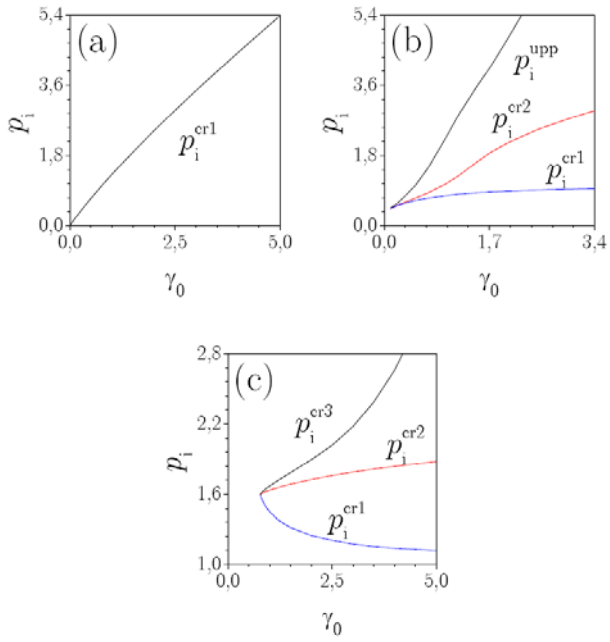


Figure 4.3. Existence and stability domains in the $(\gamma_0, p_i)$ plane. (a) The fundamental solitons in the focusing medium with the single-well nonlinear absorption profile (4.3) (the asymmetric solitons exist and are stable at $p_i > p_i^{cr1}$). (b) and (c): Dipole solitons in the double-well absorption profile (4.7), in the focusing and defocusing media, respectively.

The model with single-well absorption landscape can support higher-order (multipole) solitons too, cf. Eq. (4.4). This is an indication of the important fact that the spatial shaping of nonlinear losses can be used for generation of new types of solitons that do not exist in the uniform dissipative systems. However, such higher-order solitons in single-well landscapes always turn out to be unstable, irrespectively of the sign of the conservative nonlinearity. The instability grows with the increase of the gain, usually transforming the multipole solitons into stable fundamental ones.

Nevertheless, stable multipoles (e.g., dipoles) can be found in the system with a double-well nonlinear-absorption profile, described, e.g., by function

$$\gamma(\eta) = \gamma_0 \left(\eta^2 - \eta_0^2\right)^2 \exp\left(\kappa\eta^2\right), \tag{4.7}$$

in Eqs. (4.1) and (4.2), see examples in Fig. 4.4. Generic results can be adequately showed for $\eta_0 = 1$. We have found that, in the focusing medium with the uniform gain and double-well profile of the nonlinear absorption, all dipole solitons are symmetric (unlike the fundamental solitons in the single-well absorption landscapes, they do not feature the spontaneous symmetry breaking). The energy

flow and propagation constant of the dipoles in the focusing medium as functions of the gain strength are shown in Figs. 4.2(c) and 4.2(d), by curves denoted $U_{fs}$ and $b_{fs}$. The dipoles do not exist above the upper threshold value of the gain, $p_i^{upp}$, at which the tangential lines to the $U\left(p_i\right)$ and $b\left(p_i\right)$ curves become vertical [see Fig. 4.3(b) for the domains of stability and existence of such solitons in the $\left(\gamma_0, p_i\right)$ plane]. The dipole solitons are stable within a limited interval of gain parameters, $p_i^{cr1} < p_i < p_i^{cr2}$ (note the difference from the symmetric fundamental solitons, which have no existence boundaries, and are completely stable in the absence of the spontaneous symmetry breaking).

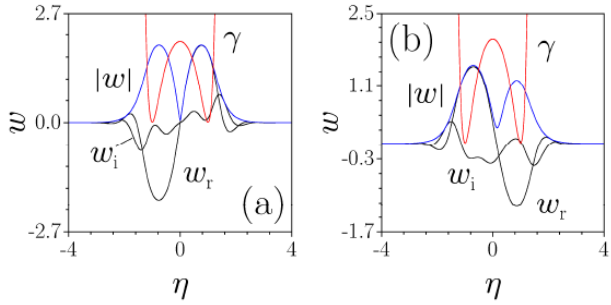


Figure 4.4. Examples of symmetric and asymmetric dipole solitons at $p_i = 3.0$ (a) and $p_i = 1.9$ (b), respectively, in the defocusing medium with the double-well nonlinear-absorption landscape (4.5) [red curves for $\gamma\left(\eta\right)$], at $\gamma_0 = 2.0$.

Various scenarios of the evolution of perturbed dipoles in the focusing medium with the double-well absorption landscape are displayed in Figs. 4.5(a)-4.5(c). At small values of the gain, $p_i < p_i^{cr1}$, the unstable dipoles usually evolve into symmetric fundamental solitons [Fig. 3.5(a)]. Stable propagation of the dipole soliton is presented in Fig. 4.5(b) for $p_i^{cr1} < p_i < p_i^{cr2}$. At larger gain levels, $p_i > p_i^{cr2}$, the dipole solitons develop an oscillatory instability and may transform into persistent breathers, without symmetry breaking. The initial stage of this process is shown in Fig. 4.5(c), in which case the emerging breather propagates stably over an indefinitely long distance.

On the contrary to the case of fundamental solitons, dipoles exhibit the spontaneous symmetry breaking in the defocusing medium with the double-well absorption landscape. This finding resembles a well-known fact that, in dual-core conservative systems, the spontaneous symmetry breaking of spatially odd modes occurs under the action of defocusing nonlinearities (in contrast to the spatially even ground state, which undergoes the symmetry breaking under the action of focusing nonlinearities [135, 136]). Examples of such symmetric and asymmetric

dipoles are displayed in Fig. 4.4, while the symmetry-breaking bifurcation is shown by the respective $U\left(p_i\right)$ and $b\left(p_i\right)$ curves in Figs. 4.2(c) and 4.2(d). The emerging asymmetric dipoles are stable, while the symmetric ones are unstable past the bifurcation point [in compliance with the supercritical character of the bifurcation in Figs. 4.2(c) and 4.2(d)]. As shown in Fig. 4.3(c), the symmetric dipoles in the two-well absorption landscapes, with the defocusing nonlinearity, are stable in the domain of $p_i^{cr1} < p_i < p_i^{cr2}$, which also implies that they can be stable only if the nonlinear-absorption strength, $\sigma_i$, exceeds a certain minimal value. The upper stability border, $p_i = p_i^{cr2}$, is actually determined by the symmetry-breaking bifurcation. The asymmetric dipoles that emerge above the $p_i^{cr2}$ curve are also stable only within a limited range of the gain parameter, $p_i^{cr2} < p_i < p_i^{cr3}$.

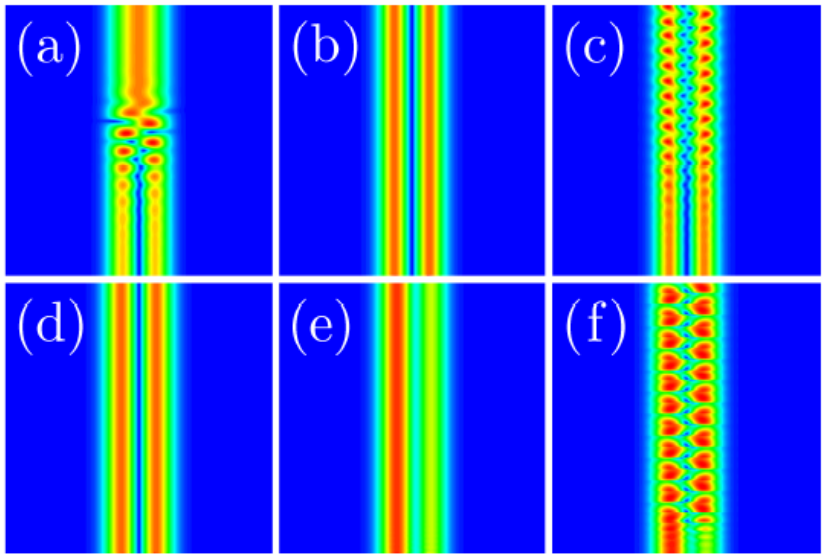


Figure 4.5. The dynamics of dipole solitons in the focusing (a)-(c) and defocusing (d)-(f) media with the double-well nonlinear-loss profile (4.7). (a) Spontaneous transformation of an unstable symmetric dipole into a fundamental soliton at $p_i = 0.8$. (b) Stable propagation of the symmetric dipole at $p_i = 1.8$. (c) The transformation of an unstable symmetric dipole into breather at $p_i = 3.2$. (d, e) The stable propagation of the symmetric and asymmetric dipoles at $p_i = 1.5$ and $p_i = 2.1$, respectively. (f) Spontaneous transformation of an unstable asymmetric dipole into a breather, with the dynamically restored symmetry, at $p_i = 2.23$. All the cases are shown for $\gamma_0 = 3$, with small noise added to the input.

Figures 4.5(d)-4.5(f) illustrate the stable and unstable evolution of the dipoles in these areas. In particular, at $p_i > p_i^{cr3}$, the asymmetric dipoles are subject to an oscillatory instability, which transforms them into breathers, leading to an effective dynamical restoration of the symmetry [Fig. 4.5(f)].

The numerical findings reported here are consistent with analytical estimates based on the Thomas-Fermi approximation, which, at the lowest order, neglects the diffraction term and conservative nonlinearity, i.e., all real terms, in Eq. (4.2). This approximation yields a real stationary wave function,

$$w_{TF} = \left(p_i/\gamma_0\right)^{1/2} \exp\left(-\eta^2/2\right). \tag{4.8}$$

Strictly speaking, the Thomas-Fermi approximation is applicable under the condition that $\gamma_0/\sigma$ and $p_i$ are large parameters, but, in reality, the accuracy of the approximation is reasonable even when these quantities take values $\sim 1$. In particular, the expression for the energy flow, $U_{TF} = \pi^{1/2} p_i/\gamma_0$, following from Eq. (4.8), approximates the $U\left(p_i\right)$ dependence in Fig. 4.2(a) quite accurately, up to the bifurcation point: for $\gamma_0 = 0.5$, the slope of the linear dependence, given by this expression, is $U_{TF}/p_i \approx 3.54$, while its numerically found counterpart is $3.52$.

At the next order of the Thomas-Fermi approximation, we substitute the wave function (4.8) into the real part of Eq. (4.2), multiply it by $w_{TF}\left(\eta\right)$, and integrate the result from $\eta = -\infty$ to $\eta = +\infty$. This procedure yields the prediction for the propagation constant, $b_{TF} = -1/4 - \sigma p_i/\left(\sqrt{2}\gamma_0\right)$. For $\sigma = -1$ and $\gamma_0 = 0.5$, this yields linear slope $0.71$ for the $b\left(p_i\right)$ dependence, while its numerical counterpart, corresponding to Fig. 4.2(b), is $0.69$.

Note that the steep anti-Gaussian modulation of the nonlinear absorption in Eq. (4.3) is not an absolutely necessary ingredient for the existence of stable solitons in the presence of the uniform linear gain. Thus, Eq. (4.2) with exponential (rather than anti-Gaussian) absorption landscape, $\gamma\left(\eta\right) = a + \cosh^2\left(\eta\right)$, gives rise to an exact chirped fundamental soliton,

$$\begin{aligned} q\left(\eta, \xi\right) &= \left(3\mu/2a\right)^{1/2} \exp\left(ib\xi\right) \mathrm{sech}^{1+i\mu}\left(\eta\right), \\ \mu &= \left(3\sigma/2a\right) + \mathrm{sgn}\left(a\right)\left[\left(3\sigma/2a\right)^2 + 2\right]^{1/2}, \end{aligned} \tag{4.9}$$

with propagation constant $b = \left(1-\mu^2\right)/2$ and $p_i = \mu\left[1 + \left(3/2a\right)\right]$. In this absorption landscape, an exact dipole soliton solution can be constructed too

$$q\left(\eta,\xi\right)=\exp\left(-5i\xi/2\right)\operatorname{sech}^{1-i\sqrt{6}}\left(\eta\right)\sinh\left(\eta\right), \tag{4.10}$$

for parameters $a=\sigma=0$ and $p_i=\left(27/2\right)^{1/2}$.

Finally, using the Thomas-Fermi approximation, it is easy to find that the mildest nonlinear-absorption profile supporting solutions with a convergent energy flow (norm) is $\gamma\left(\eta\right)\sim\left|\eta\right|^{1+\varepsilon}$ with any $\varepsilon>0$. Furthermore, in the $D$-dimensional version of Eq. (4.2) the same is true for $\gamma\left(r\right)\sim\left|r\right|^{D+\varepsilon}$.

### *4.2. Solitons in Cubic-Quintic Nonlinear Media with Localized Cubic Gain and Uniform Linear Losses*

Now we study a possibility of the existence of stable solitons in media with spatially inhomogeneous cubic gain and uniform linear losses. A challenging aspect of such a setting is that only strongly localized cubic gain is employed without the presence of the overall stabilizing quintic dissipation that is routinely employed for the investigation of solitons of Ginzburg-Landau equation. Here we show that stable solitons can be supported by the localized cubic gain with uniform linear loss in the nonlinear medium with the focusing cubic and defocusing quintic conservative parts of the nonlinearity. Realization of this model may be possible in the same settings which were considered previously [138-141].

We address the propagation of a light beam in a medium featuring cubic and quintic nonlinearities, linear loss, and localized cubic gain:

$$i\frac{\partial q}{\partial\xi}=-\frac{1}{2}\Delta q+\sigma\left|q\right|^{2}q+\sigma_{5}\left|q\right|^{4}q+ip_{i}\left|q\right|^{2}q-i\gamma q\,. \tag{4.11}$$

Here $\sigma=-1$ corresponds to the focusing cubic nonlinearity component, and $\sigma_{5}>0$ accounts for the spatially uniform defocusing quintic nonlinearity; $\gamma$ is the coefficient describing linear losses, while the localized cubic gain is described by $p_{i}=p\exp\left(-\dfrac{\eta^{2}}{\rho_{g}^{2}}\right)$, where $p$ and $\rho_{g}$ stand for the strength and width of the cubic-gain 'hot-spots', locally pumped regions created in a lossy waveguide.

Soliton solutions are searched for as $q\left(\eta,\xi\right)=w\left(\eta\right)\exp\left(ib\xi\right)$, where $w\left(\eta\right)$ is a complex function describing the shape of the dissipative soliton pinned to the localized gain spot, and $b$ is the propagation constant. The shapes of soliton solutions can be found from the following equation:

$$\frac{1}{2}\frac{d^{2}w}{d\eta^{2}}-bw+\left|w\right|^{2}w-\sigma_{5}\left|w\right|^{4}w-ip\exp\left(-\frac{\eta^{2}}{\rho_{g}^{2}}\right)\left|w\right|^{2}w+i\gamma w=0\,. \tag{4.12}$$

Stationary modes should satisfy the condition of the balance between the gain and losses: $p\int_{-\infty}^{+\infty}\exp\left(-\eta^2/\rho_g^2\right)\left|w\left(\eta\right)\right|^4 d\eta = p\int_{-\infty}^{+\infty}\left|w\left(\eta\right)\right|^2 d\eta \equiv \gamma U$, where $U$ is the total power.

First, we present analytical results based on the perturbation theory. To this end, assuming that width $\rho_g$ of the 'hot spot' is much smaller than the size of the soliton pinned to it, we approximate the gain profile by $\tilde{p}\delta\left(\eta\right)$, with $\tilde{p} = \sqrt{\pi}\rho_g p$ (so as to keep the same integral gain), and Dirac delta $\delta\left(\eta\right)$, and treat $p$ and $\gamma$ as small parameters. In the zero-order approximation, we take the exact soliton solution to Eq. (4.12) with $\gamma = p = 0$ [145]:

$$w^2\left(\eta\right) = \frac{4\sqrt{b_{co}}b}{\sqrt{b_{co}-b}\cosh\left(2\sqrt{2b}\eta\right)+\sqrt{b_{co}}}, \tag{4.13}$$

where the propagation constant and peak power are limited by the cutoff values, $0 < b < b_{co} \equiv 3/\left(16\sigma_5\right)$, $w^2\left(\eta=0\right) < I_{co} \equiv w^2\left(\eta=0, b=b_{co}\right) = 4b_{co}$, where $I_{co}$ is the cutoff intensity, and the total power is

$$U = \sqrt{8b_{co}}\ln\left(\frac{\sqrt{b_{co}}+\sqrt{b}}{\sqrt{b_{co}-b}}\right). \tag{4.14}$$

Numerical results presented below suggest that stable solitons correspond to $b_{co} - b \ll b_{co}$. In this case, the substitution of Eq. (4.13) into the power balance condition, $\tilde{p}w^4\left(\eta=0\right) = \gamma U$, yields, in the first approximation of the perturbation theory,

$$U = \frac{9\sqrt{\pi}p\rho_g}{16\gamma\sigma_5^2}. \tag{4.15}$$

This result shows the necessity of the defocusing quintic term, as the total power diverges at $\sigma_5 \to 0$. Further, the width of broad solitons with the nearly constant peak power is given by $W \equiv U/I_{co} \approx \left(3\sqrt{\pi}/4\right)p\rho_g/\left(\gamma\sigma_5\right)$.

Without assuming $b_{co} - b \ll b_{co}$ the analysis of the energy balance condition shows that the solutions exist for the gain strength exceeding the threshold value:

$$p \geq p_{thr} = G\gamma\sigma_5^{3/2}/\rho_g, \tag{4.16}$$

with numerical constant $G \approx 4.383$. At the threshold point, the (upper) soliton branch (4.15) is connected to a lower one, which can be found explicitly at $b \ll b_{co}$, i.e., for $\rho_g p \gg 5\sigma_5^{2/3}\gamma$ :

$$U \approx \left(\frac{16\gamma}{\sqrt{\pi}\rho_g p}\right)^{1/3}, b \approx \left(\frac{\gamma}{\sqrt{2\pi}\rho_g p}\right)^{2/3}. \qquad (4.17)$$

The lower branch is obviously unstable, being a separatrix between the stable zero solution and the upper branch. Note that $\sigma_5$ does not appear in solution (4.17), hence it remains valid, as the unstable one, in the absence of the quintic nonlinearity.

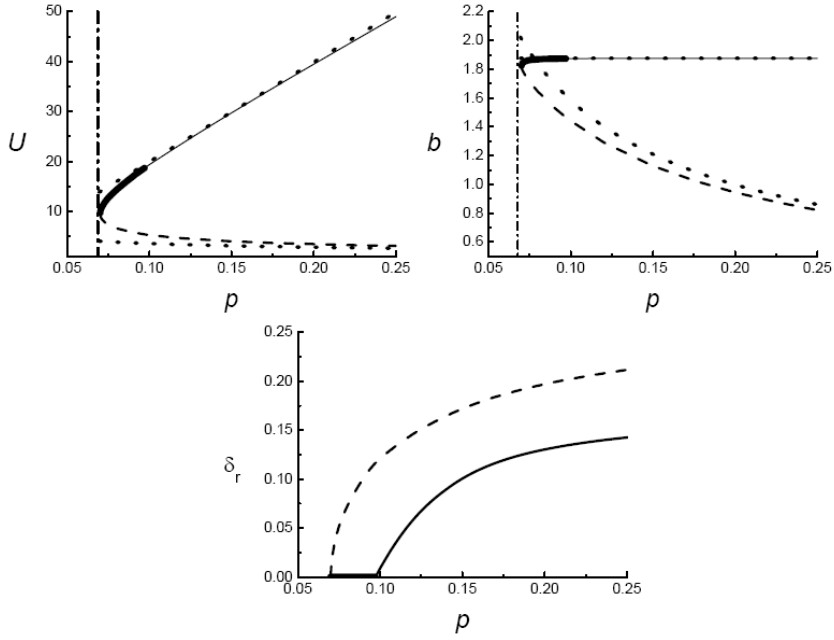


Figure 4.6. The soliton total power $U$ (top left), propagation constant $b$ (top right), and instability growth rates $\delta_r$ (bottom) vs gain coefficient $p$ at $\sigma_5 = 0.1$, $\gamma = 0.05$, $\rho_g = 0.1$. Here and in Fig. 4.7 below, the dashed line corresponds to the completely unstable lower branch, the bold segment represents the stable part of the upper branch, and its unstable continuation is depicted by the thin solid line. Analytical predictions (4.15) and (4.17) are shown by dotted curves (for the upper branch in the top right panel, the approximation amounts to $b = b_{co}$), and vertical dash-dotted lines mark the threshold point as predicted by Eq. (4.16).

Our numerical analysis confirmed all the analytical predictions made above. Figures 4.6 and 4.7 demonstrate the comparison of the theoretical and

numerical results. Soliton solutions exist if the gain exceeds the threshold value, as predicted by Eq. (4.16). Two branches of the soliton solutions originate from the threshold point, the upper one being almost exactly predicted by Eq. (4.15), while the lower branch is close to asymptotic approximation (4.17).

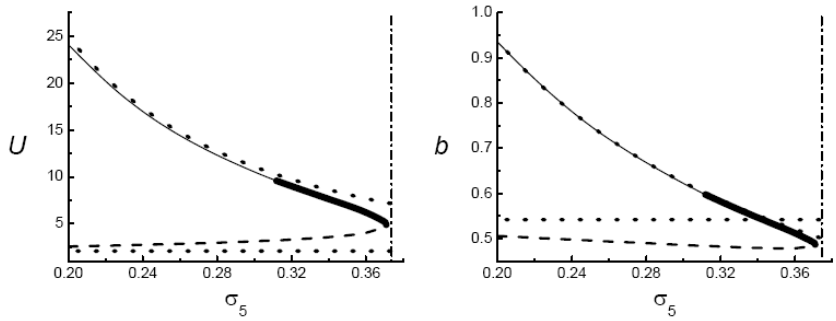


Figure 4.7. The total power and propagation constant of the soliton vs the quintic coefficient, $\sigma_5$, at $p = 0.5$, $\gamma = 0.05$, $\rho_g = 0.1$. The horizontal dotted lines represent asymptotic values (4.17), which do not depend on $\sigma_5$.

While the solitons belonging to the lower branch are completely unstable (as said above), suffering a rapid decay in the course of the propagation, a part of the upper branch is stable, as verified by the linear stability analysis and direct simulations alike. The fully unstable lower branch is characterized by a real instability growth rate, while the destabilization of the higher branch at the border between the bold and thin curves in Figs. 4.6 and 4.7 is accounted for by a pair of complex eigenvalues (the Hopf bifurcation).

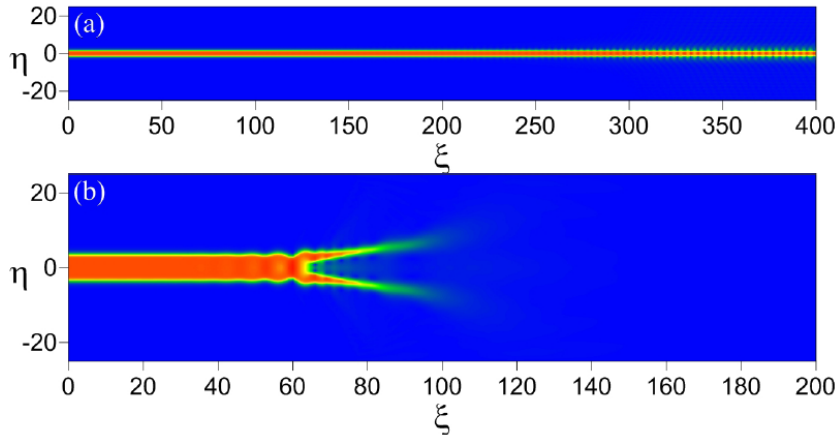


Figure 4.8. (a) The evolution of a weakly unstable soliton, belonging to the upper branch, into a stable breather, at $\sigma_5 = 0.1$, $\gamma = 0.05$, $\rho_g = 0.1$ and $p = 0.105$. (b) The decay of the localized mode at a larger value of the cubic gain, $p = 0.25$.

Accordingly, in direct simulations the unstable soliton belonging to the upper branch is transformed into a stable localized breather [see Fig. 4.8(a)]. At still larger values of $p$, the breathers become unstable too, decaying in the course of the propagation. It is worthy to stress the unexpected result that the increase of the cubic gain $p$ leads to the decay of the breathers, rather than their blowup. This may be explained by the fact that the onset of the instability causes the expansion of the wave field into the lossy medium, where it suffers the attenuation, see Fig. 4.8(b).

If the gain is fixed, while the quintic coefficient, $\sigma_5$, is varied, Fig. 4.7 demonstrates that the solitons exist below a maximum value of $\sigma_5$, which is also accurately predicted by Eq. (4.16): $\sigma_5 \leq \left[p\rho_g / (G\gamma)\right]^{2/3}$. In agreement with Eq. (4.15), $U$ is a monotonously decreasing function of $\sigma_5$ on the upper branch, and the respective dependence $b(\sigma_5)$ is close to $b_{co}(\sigma_5)$ (recall that $b \approx b_{co}$ along the upper branch).

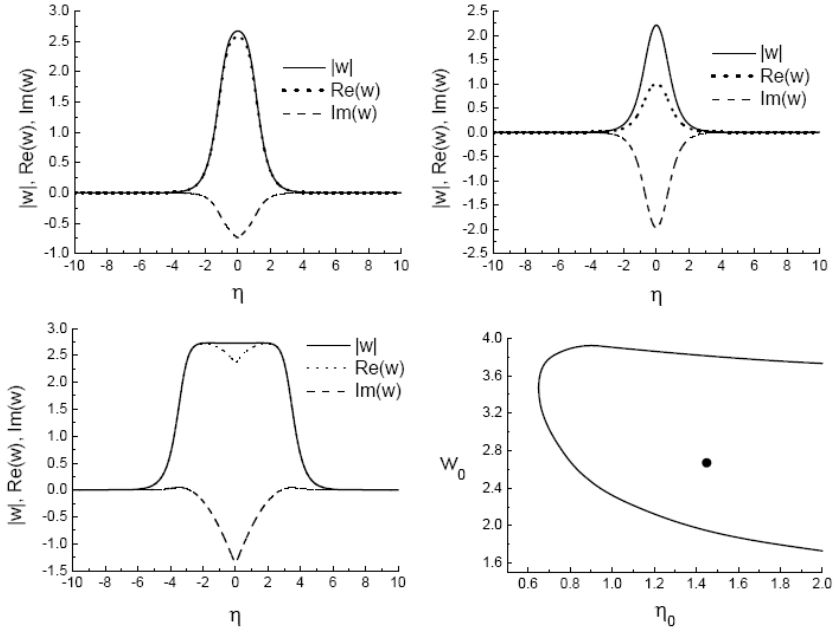


Figure 4.9. Typical examples of the solitons, for $\sigma_5 = 0.1$, $\gamma = 0.05$, $\rho_g = 0.1$: (top left panel) a stable soliton belonging to the upper branch, at $p = 0.08$; (bottom left panel) a destabilized soliton from the same branch, at $p = 0.25$; (top right panel) an unstable soliton which belongs to the lower branch, at $p = 0.08$. The bottom right panel displays the attraction basin of the stable soliton excited by the Gaussian input (see text), the bold point showing parameters of the soliton fitted to the Gaussian shape.

Generic examples of numerically found soliton profiles are displayed in Fig. 4.9. The solitons belonging to the upper branch broaden with the increase of $p$, as predicted by the above analysis.

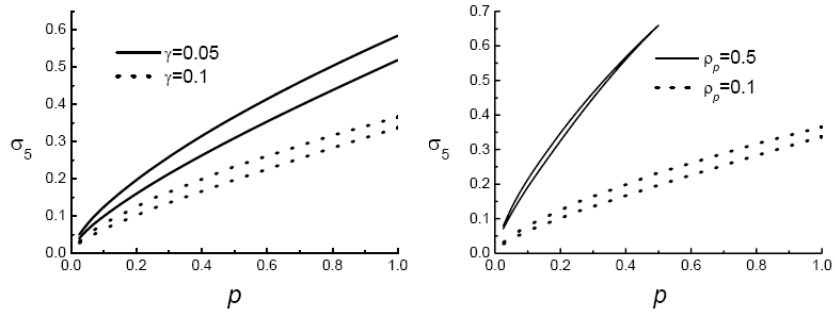


Figure 4.10. Stability domains (between the borders) for the solitons at different values of the loss coefficient, $\gamma$, and fixed width of the gain distribution, $\rho_g = 0.1$ (left panel), and at different values of $\rho_g$ and fixed $\gamma = 0.1$ (right panel).

The results obtained for the solitons are summarized in the form of stability domains in the $\left(p, \sigma_5\right)$ plane, plotted in Fig. 4.10. Solitons do not exist above the top stability border, and they are unstable below the bottom border. With the increase of the loss parameter $\gamma$, the stability domains shift to smaller values $\sigma_5$. On the other hand, they shift to larger values of $\sigma_5$ and become narrower with the increase of width $\rho_g$ of the gain profile. These trends may be explained by a straightforward consideration of Eq. (4.16), which shows that the increase of $\sigma_5$ can be compensated by the decrease of $\gamma$ or increase of $\rho_g$. The fact that the stability regions are narrow in terms of $p$ is not a problem for the experimental realization, as the gain may be easily varied by adjusting the pump intensity.

### *4.3. Summary*

Summarizing, our research presented in this Chapter has revealed that fundamental and multipole one-dimensional solitons, propagating in both focusing and defocusing nonlinear dissipative media with the uniform linear gain, can be stabilized with the help of an inhomogeneous nonlinear absorption whose strength grows with the transverse coordinate faster than $|\eta|$. Some isolated soliton solutions were found in exact analytical form. In the single-well absorption landscape only fundamental solitons are stable, featuring a spontaneous symmetry breaking in focusing media. A double-well absorption landscape is

required for the stabilization of dipoles, in that case symmetry breaking occurs in the defocusing case. The main result is that spatial shaping of the nonlinear losses can be used for the generation of new types of solitons that do not exist in uniform dissipative systems. Basic results for the symmetric fundamental solitons can be obtained in accurate analytical form by means of the Thomas-Fermi approximation.

We also studied solitons supported by a localized cubic gain embedded into a medium with a cubic-quintic nonlinearity and linear loss. Using perturbation theory and numerical analysis, a family of fundamental spatial solitons pinned to the localized nonlinear gain spot was found. On the contrary to the complex Ginzburg-Landau equation modeling uniform media, a part of the soliton family can be stable even without stabilizing quintic dissipation as long as a conservative defocusing quintic nonlinearity is also present. The family of the stable solitons is bounded by the Hopf bifurcation, which replaces them by breathers. Eventually, the breathers lose their stability, too, and decay at the increase of the localization strength.

The main results summarized in this chapter have been published in the following journals:

1. **O.V. Borovkova**, Y.V. Kartashov, V.A. Vysloukh, V.E. Lobanov, B.A. Malomed, and L. Torner, “Solitons supported by spatially inhomogeneous nonlinear losses,” Opt. Express **20**, 2657-2667 (2012).
2. **O.V. Borovkova**, V.E. Lobanov, and B.A. Malomed, “Stable nonlinear amplification of solitons without gain saturation,” Europhys. Lett. **97**, 44003 (2012).

# Chapter 5. 2D Dissipative Vortex Solitons in Media with Inhomogeneous Gain and Losses

In Chapter 4 we discussed the properties of soliton solutions in one-dimensional dissipative media. Now we focus on two-dimensional solitons, in particular, on vortices that do not exist in one-dimensional settings. While vortex solitons are well-studied in the systems governed by Ginzburg-Landau equations, no such states have been found so far in materials with a spatially inhomogeneous gain or absorption. Here we show that ring-like localized gain landscapes imprinted in focusing cubic media with two-photon absorption do support rich families of rotating vortex states, which exhibit multiple phase singularities embedded into a single vortex core and have strongly azimuthally modulated shapes. The phase singularities in such objects are found to rotate around the center of the gain landscape, with the rotation period being determined by the strength of the gain and the nonlinear absorption. Then we show that elliptical gain landscapes imprinted in focusing media with two-photon absorption support nonconventional stable vortex solitons that carry several spatially separated phase singularities with a single topological charge instead of one high-charge phase singularity in the center. The separation of phase singularities is dictated by the ellipticity of gain landscape and it only slightly changes upon variation of the gain or absorption strength. Finally, the properties of multivortex soliton complexes, composed of vortices featuring identical or opposite topological charges, supported by multi-ring gain landscapes are addressed. In the simplest geometries with two amplifying rings vortex twins with equal topological charges exhibit asymmetric intensity distributions, while vortex anti-twins may be symmetric or asymmetric, depending on the gain level and on the separation between the amplifying rings.

### *5.1. Rotating Dissipative Vortex Solitons*

In conservative systems formation of vortex solitons with multiple singularities may be stimulated by external factors, such as large sample asymmetry in nonlocal media [143] or the presence of strong optical lattices [144]. Here we show that in dissipative settings asymmetric rotating vortices may appear even in systems whose parameters are either spatially uniform (diffraction and nonlinearity) or radially symmetric (gain). This indicates that the formation of such states is mediated by complex internal energy flows that may be highly asymmetric in a system with localized gain.

The equation describing the propagation of a light beam in a two-dimensional cubic nonlinear medium with strong two-photon absorption and nonuniform gain can be written as

$$i\frac{\partial q}{\partial \xi} = -\frac{1}{2}\frac{\partial^2 q}{\partial \eta^2} - \frac{1}{2}\frac{\partial^2 q}{\partial \zeta^2} - \left|q\right|^2 q + ip\left(\eta, \zeta\right)q - i\gamma\left|q\right|^2 q\,. \qquad (5.1)$$

Here the function $p\left(\eta, \zeta\right)$ describes the gain profile; and $\gamma$ is the parameter of two-photon absorption. The nonlinear terms in Eq. (5.1) adequately model a nonlinear response of the semiconductor materials where solitons form below half the bandgap and two-photon absorption is the dominating mechanism of optical losses [145]. Suitable shaping of the concentration of amplifying centers may be used to create various gain landscapes in such materials [146].

The radially symmetric gain landscape that we consider in this section is described by the function $p\left(\eta, \zeta\right) = p_i \exp\left[-\left(r-\rho_r\right)^2 \Big/ \rho_w^2\right]$, where $p_i$ is the gain parameter, $r = \left(\eta^2 + \zeta^2\right)^{1/2}$ is the radial variable, $\rho_w$ and $\rho_r$ are the width and the radius of the amplifying ring, respectively. Here we set $\rho_r = 5.25$ and $\rho_w = 1.75$. Soliton solutions of Eq. (5.1) may exist due to the balance between localized gain and nonlinear losses, and between diffraction and focusing nonlinearity. Spatial localization of the gain ensures stability of the background at $r \to \infty$, a crucial ingredient for the stability of localized solutions. The formation of solitons should be expected around the maxima of $p\left(\eta, \zeta\right)$ where nonlinear absorption compensates gain, thus preventing the uncontrolled growth of the soliton amplitude and suppressing collapse. This point must be stressed, since the nonlinearity is cubic and the system is two-dimensional. Since an exact balance between gain and losses is required for soliton formation, the soliton shape and transverse extent should depend considerably on the shape of the amplifying domain.

In order to find rotating vortex solitons we integrated Eq. (5.1) for a variety of inputs $q\left(\eta, \zeta, \xi = 0\right)$, with single or with multiple phase singularities nested in different locations of a single core. Under proper conditions, input beams emit radiation, experience reshaping upon propagation, and approach rotating vortex soliton states. In our simulations we propagated the beams for large distances (up to $\xi \sim 20000$) to confirm stability of the obtained rotating states. We verified that identical rotating solitons can be generated with different inputs, a result that is an indication that the states are attractors with a sufficiently large basin.

The central finding is that the ring-like gain landscapes can support a rich variety of rotating vortex solitons. In all such states, phase singularities are embedded in a single vortex core and perform persistent rotation around the center of the gain ring. Examples of rotating structures with up to three singularities are shown in Fig. 4.1. Notice that all such states can be generated with the ring input beams $q \sim r \exp\left(-r^2\right) \exp\left(im\varphi\right)$ carrying singularities with winding numbers $m = 1, 2, 3$, when their centers are strongly displaced from the center of the amplifying ring at $\eta, \zeta = 0$. The number of singularities in the rotating vortex solitons is not determined exclusively by the charge or number of singularities in the input beam. Actually, rotating vortex with $m > 1$ singularities can be excited by a shifted vortex with $m = 1$. In contrast to conservative settings where rotating states emerge from azimuthally perturbed vortex solitons [147], in our dissipative system, azimuthal perturbations of radially symmetric states usually tend to decay.

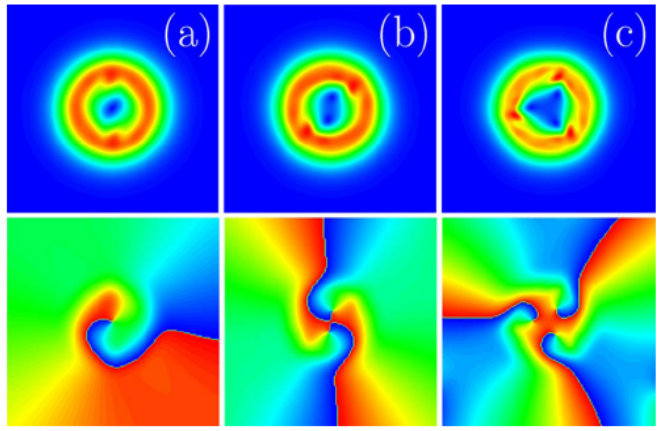


Figure 5.1. Field modulus (top) and phase distributions (bottom) for rotating vortex solitons having (a) one phase singularity at $p_i = 1.7$, (b) two singularities at $p_i = 2.0$, and (c) three singularities at $p_i = 2.8$. In all cases, $\gamma = 2.0$.

All rotating vortex solitons exhibit azimuthal modulations of the intensity distributions, in spite of the fact that the gain landscape is radially symmetric. The

depth of the azimuthal intensity modulation depends on the value of the gain parameter $p_i$. We observed that, as a rule, the azimuthal modulation is most pronounced in the center of the existence domain (in terms of $p_i$) and decreases when approaching the upper boundary of the domain. The decrease of the azimuthal modulation is usually accompanied by a decrease of separation between the phase singularities nested in the vortex core. The phase singularities in the simplest rotating vortex solitons are located symmetrically with respect to the origin at $\eta, \zeta = 0$, but we found that vortex states with an asymmetric arrangement of the singularities may be generated, too.

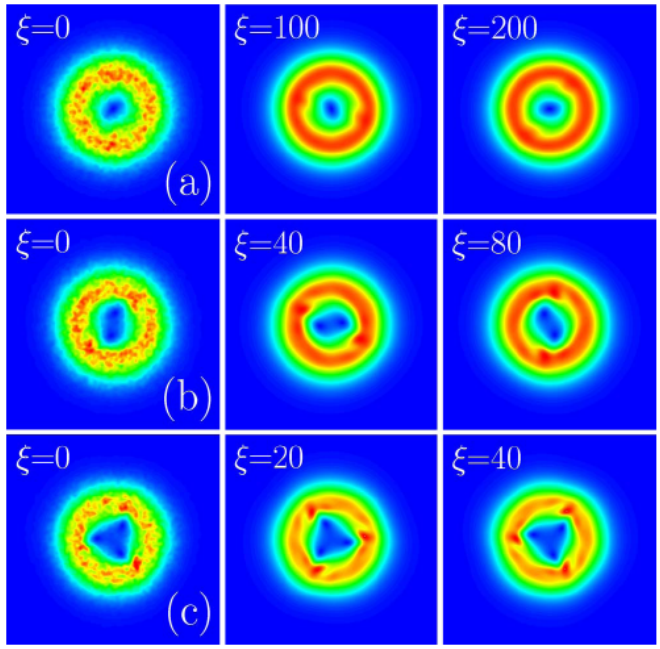


Figure 5.2. Dynamics of propagation for rotating vortex solitons having (a) one phase singularity at $p_i = 1.7$, (b) two singularities at $p_i = 2.0$, and (c) three singularities at $p_i = 2.8$. In all cases, $\gamma = 2.0$, and white noise was added into the input fields.

The propagation dynamics of the perturbed rotating vortex solitons is illustrated in Fig. 5.2. Such structures were numerically generated by the direct propagation of input beams over huge distances, so that a stable solution was excited, and subsequently used as inputs with added noise. Note that, in practice, approximate versions of such solitons may be generated by using phase masks. The perturbed solutions were then propagated for one rotation period to ensure that they perform persistent rotation even in the presence of noise. Rotating vortex solitons are characterized by highly nonconventional energy flow distributions $S_\perp = \mathrm{Im}\left(q^* \nabla_\perp q\right)$ [Fig. 5.4(d)]. They are not circular due to nonzero

radial components. There are several maxima of $|S_\perp|$ in the points where the intensity reaches the maximal values [the hydrodynamic form of Eq. (5.1) shows that asymmetric internal energy flows affect soliton intensity distributions, rendering them asymmetric]. The soliton intensity peaks rotate in the direction of the phase gradient [a counterclockwise rotation can be observed by comparing Fig. 5.4(d) and dynamics in Fig. 5.2(c)].

The existence domains of the rotating vortex solitons with two and three phase singularities are presented in Fig. 5.3. The domains were constructed by using slow modifications of the gain parameter until either transformation into radially symmetric vortex states (this scenario is typical for high $p_i$ values) or the development of instabilities is achieved. Therefore, the domains shown in Fig. 5.3 correspond to the parameter range where the rotating vortex solitons are stable. For a given strength of two-photon absorption, the stable rotating vortex solitons exist inside a limited range of values of the gain coefficient $p_i^{low} \le p_i \le p_i^{upp}$. The growth of the nonlinear losses shifts this limited existence domain to higher values of gain. Usually, vortex states with three singularities exist at highest gain values, although the existence domains for solitons with two and three singularities may overlap slightly. Similarly, vortices with one singularity exist at the lowest gain levels. Therefore, a general conclusion can be made that higher gain values allow generation of more complex rotating vortex solitons with a larger number of singularities. Similar existence domains were obtained for other $\rho_r$ and $\rho_w$ values. If $\rho_w \ll \rho_r$ an increase of $\rho_w$ results in a shift of the entire existence domains to lower gain values. However, there exists an upper limit $\left(\rho_w \sim 0.8\rho_r\right)$ for the width of the amplifying ring (that depends on $p_i$) at which rotating vortex solitons can be generated. The domains of existence of rotating vortices may overlap with domains of existence of radially symmetric states [75], i.e., several stable attractors coexist for the same set of parameters.

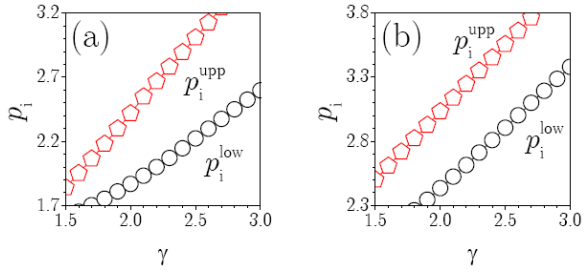


Figure 5.3. Domains of existence of stable rotating vortex solitons with (a) two and (b) three singularities on the plane $\left(\gamma, p_i\right)$.

In contrast to the conventional non-rotating vortex solitons characterized by a single propagation constant value, the local propagation constant of the rotating vortex soliton, defined as $b(\xi) = \mathrm{Arg}\left[q(\xi + d\xi)/q(\xi)\right]/d\xi$, is not identical in all points in the transverse plane. This propagation constant evolves periodically with distance $\xi$ that may be attributed to the rotation of the entire azimuthally modulated complex. Thus, Fig. 5.4(a) shows the propagation constant values $b_{\eta=0}$ and $b_{\zeta=0}$ defined along the corresponding lines as functions of $\xi$. The shift between these two periodic dependencies is readily apparent. The energy flow $U = \int\int_{-\infty}^{+\infty} |q|^2 \, d\eta d\zeta$ is a monotonically increasing function of $p_i$ irrespective of the number of singularities in the rotating vortex [Fig. 5.4(b)]. Vortices with more singularities have higher powers.

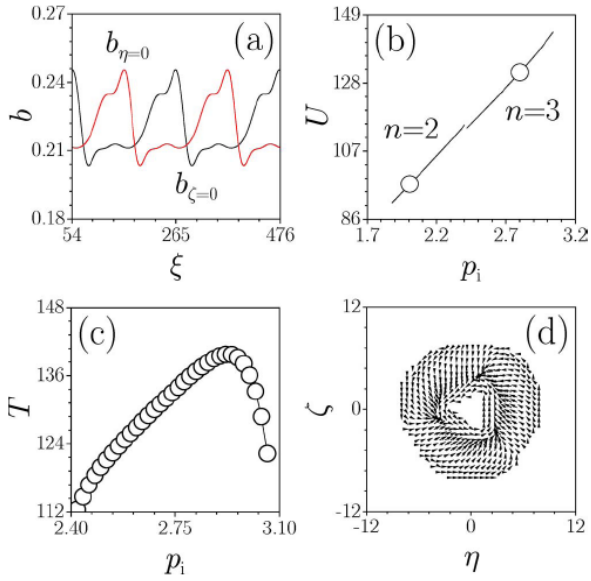


Figure 5.4. (a) Instantaneous propagation constant value defined in different points versus propagation distance for rotating vortex with one singularity at $p_i = 1.7$, $\gamma = 2.0$. (b) Energy flow versus $p_i$ for vortex solitons with two or three singularities at $\gamma = 2.0$. Points correspond to solitons shown in Figs. 5.1(b) and 5.1(c). (c) Period of rotation for vortex with three singularities versus $p_i$ at $\gamma = 2.0$. (d) Map of internal energy flows in vortex soliton from Fig. 5.1(c).

The dependence of the rotation period $T$ of the vortex states on the gain parameter [Fig. 5.4(c)] was also studied. In the vicinity of the lower border of the existence domain $p_i \to p_i^{low}$, the rotation period grows with $p_i$ monotonically, but when $p_i \to p_i^{upp}$ the rotation period rapidly decreases. A decrease in the period of

rotation favors the tendency for singularities to fuse into one central singularity with a higher winding number at sufficiently high gain levels (in this case the rotating vortex transforms into radially symmetric one). The dependencies $T\left(p_i\right)$ shown in Fig. 5.4(c) are typical for all vortex solitons discussed in this section.

### *5.2. Stable Vortex Solitons with Separated Phase Singularities*

While in conservative uniform media vortex solitons with any topological charge have radially symmetric shapes and carry a single phase dislocation in the center [17], in media where the refractive index or the nonlinearity are transversally inhomogeneous or depend on the sample geometry, it becomes possible to form nonconventional vortex soliton states featuring several, spatially separated phase dislocations nested in a common vortex core. In this section it is shown that elliptical gain landscape imprinted in the medium with strong nonlinear absorption may support stable elliptical vortex solitons that carry several spatially separated single-charge dislocations.

The propagation of light in the medium with elliptically shaped gain landscape can be modeled by Eq. (5.1) with $p\left(\eta,\zeta\right)=p_i\exp\left[-\left(r-\rho_r\right)^2\Big/\rho_w^2\right]$, where $r=\left(\left(\varepsilon\eta\right)^2+\zeta^2\right)^{1/2}$, $\varepsilon$ is the parameter that defines the ellipticity of the gain profile, and $\rho_r$ sets the smaller semiaxis of the elliptical gain landscape (notice that the length of the longer semi-axis that is parallel to the $\eta$ axis depends on $\rho_r$ as well as on $\varepsilon$). We set $\rho_r=5.25$ and $\rho_w=1.75$ as in Section 5.1. For smaller values of $\rho_r$ or $\rho_w$ higher gain levels are usually required for the generation of vortex solitons, but their properties remain qualitatively similar to the ones described below. In fact, one can always use scaling transformations in Eq. (5.1) to set a desired value for $\rho_r$. Also, we varied the parameter $\varepsilon$ in the range $0.5<\varepsilon<1.0$.

Elliptical gain landscapes may be implemented experimentally by using properly shaped pump beams or materials with a specially shaped concentration of active centers. Such fabrication techniques are well established and readily used in the area of fiber optics. Also, an original method to manufacture laser gain media with a spatially variable gain profile, that may be used to implement the gain profiles we consider, has been invented [148].

Vortex solitons of Eq. (5.1) have the form $q\left(\eta,\zeta,\xi\right)=\left[w_r\left(\eta,\zeta\right)+iw_i\left(\eta,\zeta\right)\right]\exp\left(ib\xi\right)$, with $b$ being the propagation constant, and $w_r, w_i$ being the real and imaginary parts of the field. The topological charge of such a vortex can be obtained as $m=\left(2\pi\right)^{-1}\oint\arctan\left(w_i/w_r\right)d\phi$, where one can

use any closed contour surrounding the phase dislocation to calculate the accumulated phase $\phi$. In the case of $l$ dislocations, the topological charges can be calculated for each of them. In Eq. (5.1) vortex solitons form due to the competition between gain and two-photon absorption that results in suppression of collapse and azimuthal instabilities even for cubic nonlinearities. In ring-like gain landscapes with $\varepsilon = 1$ that were discussed in the previous section, radially symmetric vortex solitons are attractors and form dynamically from various vortex-carrying inputs, such as $q\big|_{\xi=0} = Ar^{|m|}\exp\left(-r^2/\rho^2\right)\exp\left(im\phi\right)$, where $m$ is the input topological charge [75].

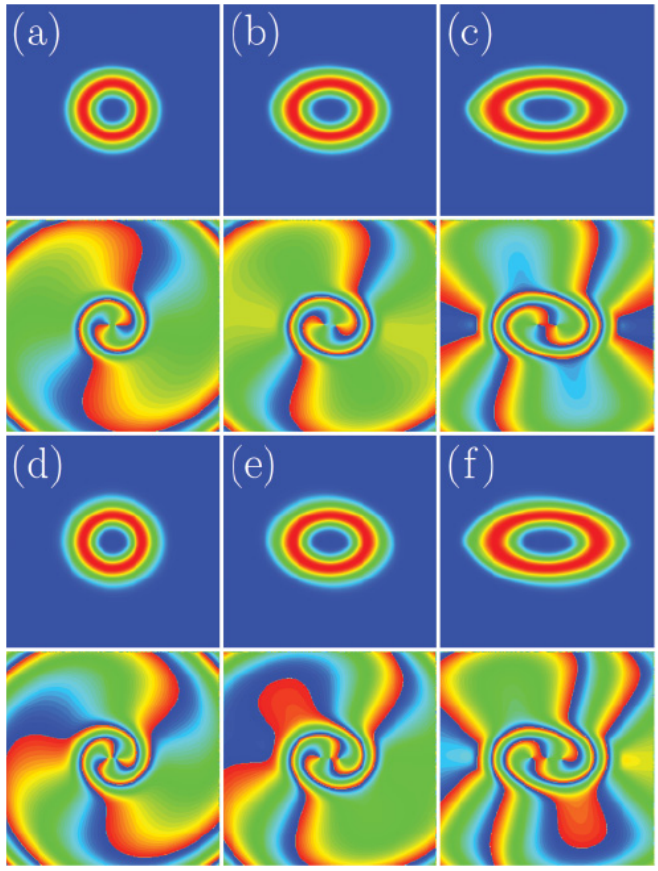


Figure 5.5. (top) Field modulus and (bottom) phase distributions for dissipative vortex solitons with two phase dislocations at (a) $\varepsilon = 0.9$, (b) $\varepsilon = 0.7$, and (c) $\varepsilon = 0.5$ and for solitons with three phase dislocations at (d) $\varepsilon = 0.9$, (e) $\varepsilon = 0.7$, and (f) $\varepsilon = 0.5$. In all cases $p_i = 7$ and $\gamma = 2.0$.

Here we study what happens with output vortex soliton upon stretching of the gain landscape (a decrease of $\varepsilon$). Thus, we solved Eq. (5.1) with the above mentioned inputs up to large distances $\xi \sim 10^4$. The stability and robustness of

the excitation of the resulting beams (attractors of the system) were tested by adding noise to the reached states and propagating them for another $\xi \sim 10^3$ units. It was found that while for $m = 1$ inputs the phase dislocation always remains in the center of the vortex that becomes elliptical for $\varepsilon < 1$, the input beams with $m > 1$ always excite vortex solitons with $m$ spatially separated single-charge dislocations nested in the common vortex core. Figure 5.5 illustrates this effect for input beam with topological charges $m = 2$ and $3$. The stretching of the gain landscapes results in a considerable expansion of the vortex states. The high-charge dislocation located initially in the center of the pattern splits into $m$ dislocations, and this splitting usually occurs in the direction of the stretching of the gain landscape. Notice that while each dislocation has a unit charge, the total topological charge of the pattern calculated over the closed contour surrounding all dislocations remains equal to $m$. For vortices with odd charges, one dislocation always remains in the center of the pattern, while in vortices with even charges, all dislocations are shifted from the center.

The distance $d$ between the outermost dislocations grows considerably with a decrease of $\varepsilon$ (an increase of ellipticity), and this spacing is always larger for vortices with higher $m$ values [Fig. 5.6(a)]. At the same time, the distance $d$ only slightly varies with modifications of the gain and absorption – increasing the gain strength results in the decrease of the separation between dislocations. Still, the main factor determining the splitting of dislocations is the geometrical ellipticity of the gain landscape. It should be stressed that the distances between neighboring dislocations are different for vortex solitons with topological charges $m > 3$.

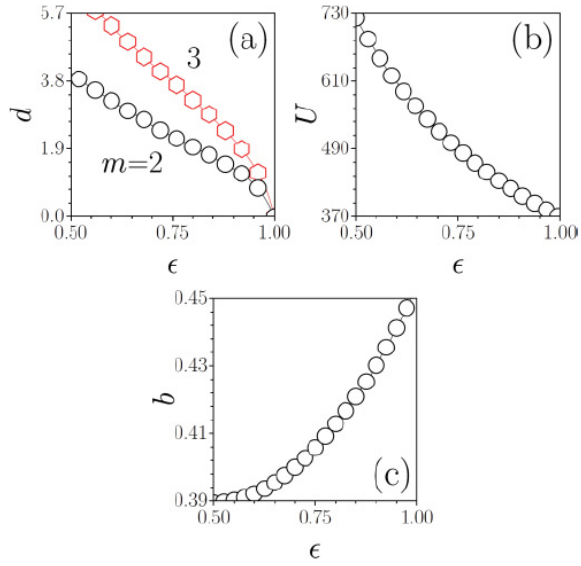


Figure 5.6. (a) The separation between outermost phase dislocations for vortex solitons with $m = 2$ and $3$ versus $\varepsilon$. The (b) energy flow and (c) propagation constant of a vortex soltion with $m = 2$ versus $\varepsilon$.

The dependence of the energy flow $U$ of vortex solitons on the ellipticity parameter is shown in Fig. 5.6(b). The energy flow increases upon the stretching of the gain landscape. The curves $U(\varepsilon)$ are almost indistinguishable for $m = 2, 3$ and only one of them is shown. The propagation constant for a vortex soliton with two dislocations decreases with decreasing $\varepsilon$ [Fig. 5.6(c)].

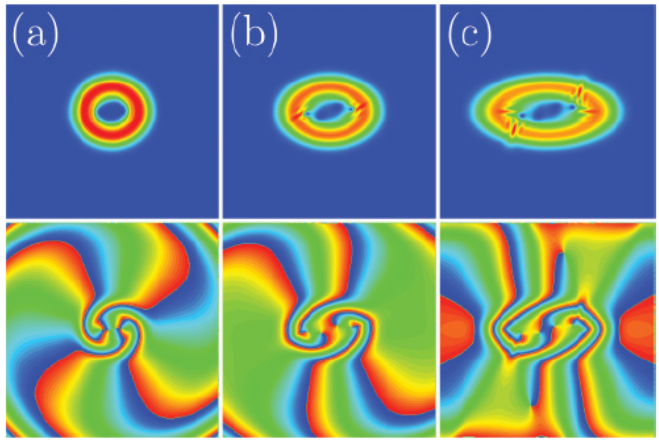


Figure 5.7. (top) Field modulus and (bottom) phase distributions in unconventional azimuthally modulated dissipative vortex solitons with four phase dislocations at (a) $\varepsilon = 0.9$, (b) $\varepsilon = 0.7$, and (c) $\varepsilon = 0.5$ In all cases $p_i = 7$ and $\gamma = 2.0$.

While for solitons with $m = 2, 3$ presented above, the phase dislocations were separated only along the $\eta$ axis (in the direction of the stretching of the gain landscape), the situation is also possible when dislocations shift along both $\eta$ and $\zeta$ axes. This is the case for higher-charge vortex solitons with $m > 3$. An example for $m = 4$ is shown in Fig. 5.7. In this case the shift of dislocations may be so considerable that they fall into high-gain domains, around which the field intensity is not small anymore that results in a considerable deformation of vortex intensity distributions.

### *5.3. Vortex Twins and Anti-Twins supported by Multi-Ring Gain Landscapes*

It has been shown above that the dissipative vortex solitons exist and can be stable in ring-shaped gain landscapes. Now we address vortex soliton complexes supported by the system of amplifying rings. In particular, we show that suitable gain landscapes made of well-separated or strongly overlapping amplifying rings imprinted in a Kerr nonlinear medium with strong two-photon absorption support stationary vortex twins and anti-twins. Vortex twins form as

pairs of vortices with identical topological charges and they always exhibit asymmetric shapes. Vortex anti-twins carry two opposite charges and can be symmetric or asymmetric, depending on the gain level.

As in the previous section we utilize Eq. (5.1) for the description of a laser beam propagation in a material with inhomogeneous gain, whose profile is described by the function $p\left(\eta,\zeta\right)=p_i\sum_j \exp\left[-\left(r_j-\rho_r\right)^2/\rho_w^2\right]$, where $p_i$ is the gain parameter, $r_j^2=\left(\eta-\eta_j\right)^2+\left(\zeta-\zeta_j\right)^2$, and $\eta_j$, $\zeta_j$ stand for the coordinates of the center of the *j*th amplifying ring. The distance between the centers of the neighboring rings is equal to $2s\rho_r$, i.e. at $s=1$ the maxima of two rings overlap (this results in an increase of the effective amplification in the overlap region), while at $s\to\infty$ the distance between rings becomes infinitely large and one recovers the case of a single amplifying ring. Here, we set $\rho_r=5.25$, $\rho_w=3.1$, and $\gamma=2.5$ and use the gain level $p_i$ and separation between rings $s$ as control parameters. However, it was verified that the results reported here remain qualitatively similar for other values of $\rho_r$, $\rho_w$, and $\gamma$. The field of the stationary solutions can be written in the form $q\left(\eta,\zeta,\xi\right)=w\left(\eta,\zeta\right)\exp\left(ib\xi\right)$, where $w\left(\eta,\zeta\right)$ is a function describing the multi-vortex shape and $b$ is the propagation constant. Each individual vortex, that forms in the amplifying ring, is characterized by its topological charge $m$. Here the simplest case with $m=\pm1$ is considered, although higher-charge vortices may also form complexes. The multi-vortex states are stable attractors in certain parameter region and they were obtained by solving Eq. (5.1) with a standard split-step fast Fourier method up to large distances with input conditions consisting of several rings with suitable wave front distributions. The families of solutions were obtained by changing $p_i$, $s$ and using the output field from a previous step as the input condition for the new set of $p_i$, $s$ values.

First, the simplest gain landscape with two amplifying rings is considered. Such gain landscapes support vortex twins and anti-twins (Fig. 5.8). The multivortex complexes exist within a wide range of gain parameters and for different separations between the amplifying rings. Within the vortex-antivortex family, two types of solitons were found: solutions whose field modulus distributions are symmetric with respect to both $\eta,\zeta=0$ axes [Fig. 5.8(a)] and solutions that are asymmetric with respect to vertical axis $\eta=0$ [Fig. 5.8(b)]. In all cases vortex twins are asymmetric with respect to both $\eta,\zeta=0$ axes [Fig. 5.8(c)]. A close inspection of the phase distribution of the multivortex states reveals that in addition to the main phase dislocations residing in the centers of the amplifying rings, secondary dislocations may appear in low-intensity regions. Such secondary vortices ensure a smooth joining of the complex internal currents (that are not

circular, unlike in usual radially symmetric vortices) inside multivortex states, but at the same time they result in symmetry breaking, especially when dislocations appear not in pairs [Fig. 5.8(c)]. In the domain between amplifying rings, the field modulus features an interference pattern that becomes smoother with increasing separation $s$ between the amplifying rings.

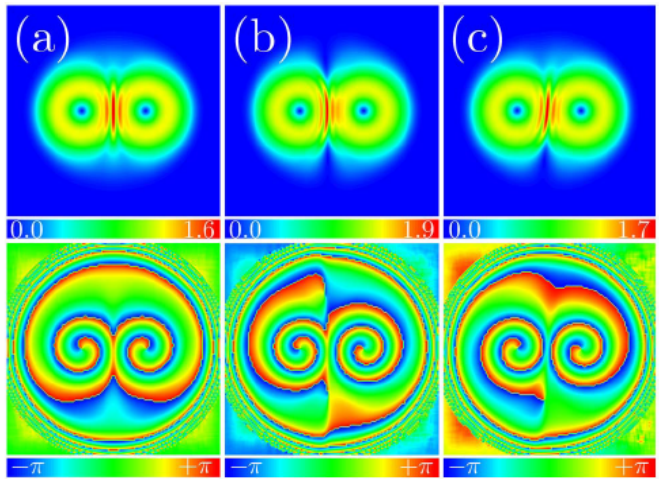


Figure 5.8. (a) Symmetric vortex-antivortex mode at $p_i = 3.7$. (b) Asymmetric vortex-antivortex soliton at $p_i = 5$. (c) Asymmetric vortex-vortex mode at $p_i = 4$. Top row: field modulus distribution, bottom row: phase distributions. In all cases $s = 1.5$.

By the very nature of dissipative solitons, their energy flow $U$ and propagation constant $b$ are determined by the gain and losses. Figure 5.9(a) shows the energy flow $U$ of the vortex anti-twins versus the gain parameter $p_i$. Despite the smooth growth of the energy flow with $p_i$, the symmetry of the solution may change along the curve. Thus, for $s = 1.5$, the soliton mode is symmetric for $1.45 \le p_i \le 2.2$ and $2.7 \le p_i \le 3.75$ (black branches) and is asymmetric for other $p_i$ values (red branches). The asymmetry becomes more pronounced with increasing gain. The dependence $U\left(p_i\right)$ for asymmetric vortex twins (not shown) is similar to that of vortex anti-twin states. We found that, as in the case of single vortex solitons supported by a single gain ring [75], stable multivortex solitons do not exist below a threshold gain level [the curve in Fig. 5.9(a) stops at the corresponding $p_i = p_i^{\min}$ value]. For smaller values, the existing absorption cannot be compensated by the available gain. Only symmetric vortex-antivortex soliton modes exist when $p_i \to p_i^{\min}$. At the same time, no upper threshold in gain was found, although only strongly asymmetric states can be generated at high $p_i$ values.

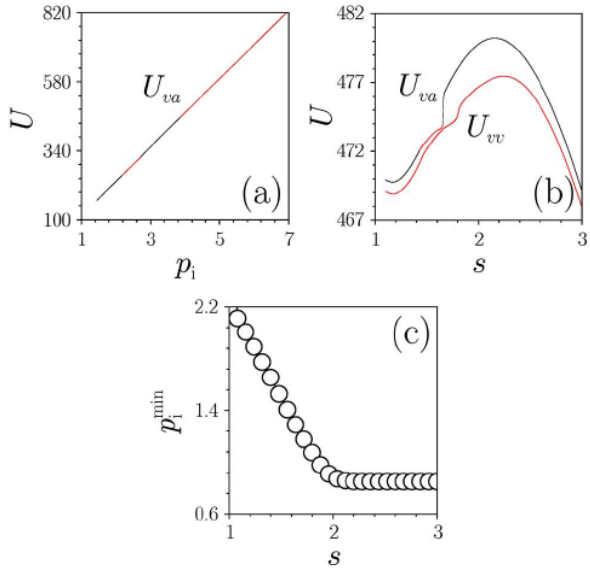


Figure 5.9. (a) Energy flow of vortex-antivortex soliton versus $p_i$ at $s = 1.5$. (b) Energy flow of vortex-vortex and vortex-antivortex solitons versus $s$ at $p_i = 4$. The branches corresponding to symmetric solitons are shown black, while branches of asymmetric solitons are shown red. (c) Minimal gain required for existence of stable vortex-antivortex solitons versus $s$.

Of particular interest is the influence of the distance between the centers of the amplifying rings on the energy flow [Fig. 5.9(b)]. Despite the fact that decreasing the separation results in overlapping amplifying rings and in an effective growth of the gain, it was found that both vortex-vortex and vortex-antivortex solitons can exist only above a minimal ring separation. For both types of solitons, the energy flow is a nonmonotonic function of the separation. At moderate gain levels, e.g., $p_i = 4$, only a small portion of the vortex-antivortex branch for $1.43 \le s \le 1.66$ is asymmetric. Notice that the asymmetric vortex-vortex family terminates exactly for the same $s$ value as the symmetric vortex-antivortex family. Both dependencies $U_{va}$ and $U_{vv}$ approach the same limiting value at $s \to \infty$, which corresponds to the energy of two vortex solitons supported by a single ring.

As it was mentioned above, both vortex-vortex and vortex-antivortex families may be stable only above a minimum gain level $p_i^{min}$. In Fig. 5.9(c), this threshold gain is plotted as a function of the separation between the amplifying rings. Somehow surprisingly, for weakly separated rings a larger gain is necessary for the stabilization of the multivortex complexes. The minimal threshold gain is found to rapidly diminish with increasing separation between rings; it saturates already at $s \sim 2$, when the vortex soliton modes residing in different rings weakly

affect each other. Also, we found that all vortex complexes studied here are rather robust objects.

Besides vortex-pairs, more complex stable multivortex states were also found. In particular, we were able to generate a variety of complexes composed of three and four vortex rings. However, it becomes more and more difficult to generate states with symmetric field modulus distributions in structures with large number of amplifying channels. In contrast, the domains of existence of stable multivortex complexes in $\left(s, p_i\right)$ plane do not change qualitatively with the increase of number of amplifying rings or with modifications in their mutual arrangement.

Examples of states including three vortices with identical topological charges supported by a triangular system of amplifying rings are shown in Fig. 5.10(a). One can observe additional secondary multiple dislocations in the region between amplifying rings. For comparison, only one such dislocation is visible in the vortex-vortex complex show in Fig. 5.8(c). As mentioned above, such additional dislocations are needed to allow closed-contour energy circulation in the wave front; thus they appear in the stationary vortex for a variety of inputs. The pattern becomes somewhat smoother when one of the vortices carries an opposite topological charge [Fig. 5.10(b)]. Figure 5.10(c) shows a stable structure comprising two pairs of vortices and antivortices. Different arrangements of the dislocations in such complexes generate various stable soliton families with slightly different energy flows. All these families may be completely stable for the same set of system parameters, although that they are obtained using different initial conditions.

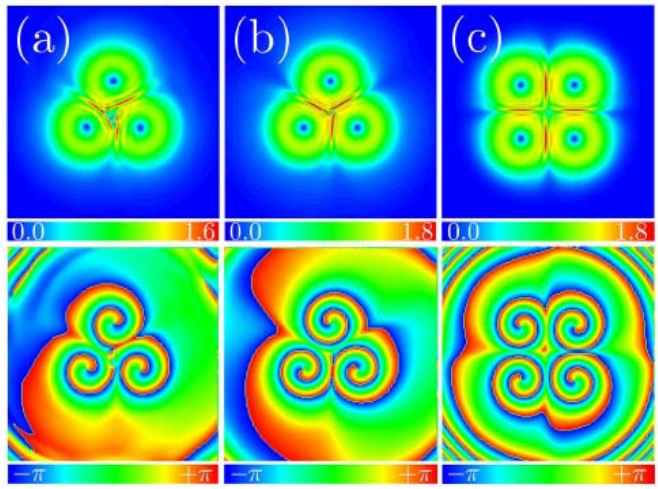


Figure 5.10. Multivortex solitons in gain landscapes with three (a), (b), and four (c) rings. In (a) $p_i = 3$, while in (b), (c) $p_i = 4$. Top row shows field modulus distributions, while bottom row shows phase distributions. In all cases $s = 1.5$.

### *5.4. Summary*

In this Chapter we showed that suitable ring-like gain landscapes imprinted in a cubic nonlinear media with two-photon absorption support rotating vortex solitons carrying multiple phase singularities and possessing azimuthally modulated shapes. The rotating states feature a strong modulation in the azimuthal direction, even when all parameters of the system are either spatially uniform or radially symmetric.

Upon the transformation of the ring-shaped gain landscape into an elliptical one, the phase dislocation of the initial multivortex state transforms into several single-charge dislocations, which are still nested in a common vortex core. Such elliptically shaped vortex solitons with multiple dislocations are attractors of the system, thus in principle they can be excited with various vortex-carrying input beams. The separation between dislocations may be comparable with the width of the amplifying ring, and it is dictated mainly by the geometry of the gain landscape.

Moreover, it was also shown that more complex gain landscapes, composed of several amplifying rings, can support rich families of dissipative multi-vortex solitons, which turn out to be completely stable. Vortex twins and anti-twins can be symmetric or strongly asymmetric, depending on the arrangement of the individual vortices in the neighboring amplifying rings and on the gain strength.

The main results summarized in this chapter have been published in the following journals:

1. **O.V. Borovkova**, V.E. Lobanov, Y.V. Kartashov, and L. Torner, “Rotating vortex solitons supported by localized gain,” Opt. Lett. **36**, 1936-1938 (2011).
2. **O.V. Borovkova**, V.E. Lobanov, Y.V. Kartashov, and L. Torner, “Stable vortex-soliton tori with multiple nested phase singularities in dissipative media,” Phys. Rev. A **85**, 023814 (2012).
3. **O.V. Borovkova**, Y.V. Kartashov, V.E. Lobanov, V.A. Vysloukh, and L. Torner, “Vortex twins and anti-twins supported by multiring gain landscapes,” Opt. Lett. **36**, 3783-3785 (2011).

# Chapter 6. 3D Dissipative Fundamental and Vortex Light Bullets

In the Introduction it was discussed that fully three-dimensional spatiotemporal optical solitons or light bullets have never been observed in uniform nonlinear media to date and that for their experimental demonstration novel engineered materials (whose properties, such as refractive index or nonlinearity, may vary in the transverse plane or in the longitudinal direction) are required. Among the examples of such media are conservative materials with transverse refractive index modulations where stable light bullets were theoretically predicted [149, 150] and whose experimental existence has been explored recently [49]. Such refractive index modulations may support various stable spatiotemporal states not only in conservative, but also in the dissipative media, where light evolution is described by the complex cubic-quintic Ginzburg-Landau equation [61, 63-65, 151, 152].

In this Chapter we discuss a simpler setting with an homogeneous refractive index, nonlinearity, two-photon absorption, and spatially profiled gain, where stable spatiotemporal solitons may form even in the absence of stabilizing three-photon absorption that is typically required in Ginzburg-Landau models. We show that focusing cubic medium with gain localized in both space and time and uniform nonlinear losses does support various stable three-dimensional solitons. While spherically symmetric gain landscapes support stable fundamental solitons, gain profiles featuring ring-like spatial and bell-like temporal shapes are shown to support stable vortex bullets. It is also shown that elliptical gain landscapes give rise to stable light bullets with multiple spatially separated single-charge dislocations.

### *6.1. Topological Light Bullets*

We consider the propagation of a spatiotemporal wave packet along $\xi$-axis in a cubic nonlinear medium with two-photon absorption and nonuniform gain that can be described by the following equation that is a particular case of Eq. (1.9) discussed in the introduction:

$$i\frac{\partial q}{\partial \xi} = -\frac{1}{2}\left(\frac{\partial^2 q}{\partial \eta^2} + \frac{\partial^2 q}{\partial \zeta^2}\right) - \frac{\beta}{2}\frac{\partial^2 q}{\partial \tau^2} - \left|q\right|^2 q + ip\left(\eta, \zeta, \tau\right)q - i\gamma\left|q\right|^2 q\,. \qquad (6.1)$$

In our numerical calculations we consider a medium with focusing nonlinearity and assume anomalous dispersion (i.e., we set $\beta = 1$).

The key novelty of the setting considered here is the presence of gain localized in both space and time and moving with the group velocity of the light bullet. Suitable shaping of the concentration of amplifying centers or spatially localized optical pumping in the material with focusing nonlinearity and anomalous group velocity dispersion can be used for the creation of localized spatial gain landscapes. Implementation of the running gain propagating with the group velocity of the spatiotemporal wave packet may be accomplished by using an adapted variant of the so-called tilted-pulse-front amplification techniques [153]. Such a method was introduced in the beginning of the 1980s as the group-velocity matching technique between the optical pump pulse and the generated or amplified radiation. By using such traveling-wave excitation of laser materials, especially dye solitons, semiconductors, and nonlinear crystals of the optical parametric amplifiers, extremely high gain and reduced amplified spontaneous emission could be obtained. Currently the tilted-phase-front pumping is widely applied for the excitation of short-wavelength lasers, broadband frequency conversion, and high-field terahertz pulse generation by the optical rectification of femtosecond laser pulses.

Solitons in the system governed by Eq. (6.1) form due to a double balance between localized gain and nonlinear losses, on the one hand, and between diffraction, dispersion, and focusing nonlinearity, on the other hand. Spatiotemporal localization of gain ensures stability of the background at $\left|\zeta\right|, \left|\eta\right|, \left|\tau\right| \to \infty$, which is a crutial ingredient for the stability of localized solutions. The formation of light bullets occurs around the maxima of gain landscape $p\left(\zeta, \eta, \tau\right)$ where two-photon absorption compensates gain, thus preventing the uncontrolled growth of the optical field amplitude and suppressing collapse, even though the conservative nonlinearity is cubic. Since an exact balance between gain and losses is required in both space and time for three-dimensional soliton formation, the shape of soliton and its extent along $\zeta, \eta, \tau$ axes strongly depend on the shape of the amplifying domain, and on the strength of gain and nonlinear

absorption. This follows from the integral condition of balance between gain and losses that can be derived from Eq. (6.1):

$$\gamma \iiint |q|^4 \, d\eta d\zeta d\tau = \iiint p(\eta, \zeta, \tau) |q|^2 \, d\eta d\zeta d\tau \, . \qquad (6.2)$$

First we address spherically symmetric spatiotemporal gain landscapes described by the function $p = p_i \exp\left(-r^2/\rho_w^2\right)$, where $r = \left(\eta^2 + \zeta^2 + \tau^2\right)^{1/2}$, $p_i$ is the gain parameter, and $\rho_w$ is the gain profile width (further we set $\rho_w = 1.5$). The profiles of simplest fundamental light bullets supported by such gain landscapes were searched in the form $q = w(r)\exp(ib\xi)$, where the complex function $w = w_r + iw_i$ describes soliton shape. We found the soliton profiles numerically using a relaxation method taking into account the balance condition (6.2) and the fact that in dissipative systems the propagation constant and all other soliton parameters are determined by the gain and loss coefficients $p_i$ and $\gamma$.

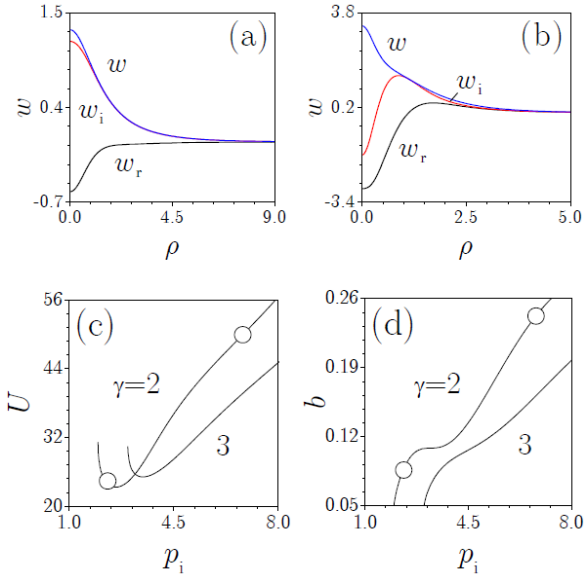


Figure 6.1. Profiles of spherically symmetric solitons at (a) $p_i = 2.3$ and (b) $p_i = 6.8$ for $\gamma = 2.0$. Here $w$ is a modulus of the solution. Energy (c) and propagation constant (d) versus gain parameter $p_i$. Circles correspond to solitons in panels (a) and (b).

The typical shapes of simplest spherically symmetric dissipative light bullets are shown in Figs. 6.1(a) and 6.1(b). Such solitons are always characterized by the nontrivial internal phase distributions (see also Fig. 6.3). There is a flow of energy from the domain with gain toward the periphery of material where only nonlinear losses are acting. Due to this energy flow, light can strongly penetrate

into domains with losses, especially in the low-energy limit. For fixed nonlinear losses $\gamma$, an increase of gain $p_i$ (that we further use as a control parameter in our system) is accompanied by the progressive soliton localization in the domain with gain. The internal phase chirp in the soliton becomes more pronounced with increase of $p_i$ [compare Figs. 6.1(a) and 6.1(b)]. Notice that for sufficiently high $p_i$ values a narrow spike develops on top of the broad pedestal in soliton shape [Fig. 6.1(b)].

The energy of a fundamental light bullet $U = \int\int\int_{-\infty}^{+\infty} |q|^2 \, d\eta d\zeta d\tau$ nontrivially depends on the gain parameter $p_i$ [Fig. 6.1(c)]. The initial decrease of $U$ is followed by growth, which is monotonic for $\gamma > 1$ and nonmonotonic for $\gamma < 1$. Light bullets can be obtained only when the gain parameter exceeds a minimal value $p_i^{low}$. The derivative $dU/dp_i$ tends to infinity, although the energy value $U$ remains finite when $p_i \to p_i^{low}$. We found that $p_i^{low}$ grows almost linearly with the increase of nonlinear losses [Fig. 6.2(a)] and monotonically decreases with the increase of the width of domain with gain. Similarly to energy, the propagation constant $b$ of the light bullet is the nonmonotonic function of $p_i$ for small nonlinear losses, but already for $\gamma \sim 3$ the propagation constant monotonically increases with $p_i$ [Fig. 6.1(d)]. When $p_i \to p_i^{low}$ the propagation constant approaches zero.

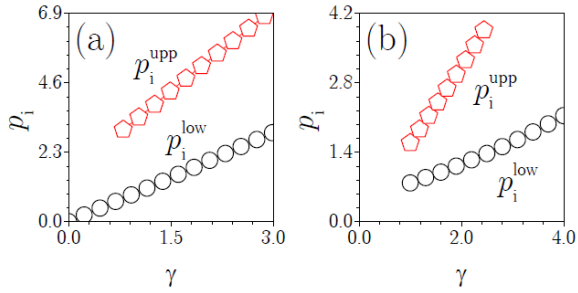


Figure 6.2. Lower $p_i^{low}$ and upper $p_i^{upp}$ borders of stability domain for (a) fundamental light bullets and (b) vortex light bullets with $m = 1$.

To elucidate the stability of the light bullets, we propagated them for large distances, up to $\xi \sim 10^4$, in the presence of added input noise by solving the governing equations with a standard split-step fast Fourier algorithm. We found that for a fixed strength of two-photon absorption the fundamental light bullets are usually stable within a finite interval of gain coefficients $p_i^{low} < p_i < p_i^{upp}$ adjacent to minimal gain level $p_i^{low}$ required for soliton existence. With increase of

nonlinear losses the domain of stability slightly broadens and shifts to higher values of gain [Fig. 6.2(a)]. The solitons belonging to the stability domain rapidly clean up the noise and propagate in a stable fashion over indefinitely long distances (Fig. 6.3, left). Outside the stability domain at $p_i > p_i^{upp}$, spherically symmetric solitons decay or experience considerable shape transformations. Propagating perturbed spherically symmetric solutions, we surprisingly found that instability may result in their transformation into stable asymmetric light bullets featuring ellipsoid-like states (Fig. 6.3, center). Such asymmetric solitons have equal widths in two orthogonal axes (e.g., $\eta, \zeta$) and larger width along the third axis (e.g., $\tau$), which is highly unexpected considering that all parameters in the system are either uniform or spherically symmetric. The orientation of longer axis of such ellipsoid-like bullets is arbitrary. Such asymmetric solitons are characterized by unusual asymmetric internal energy flows, in contrast to spherically symmetric states.

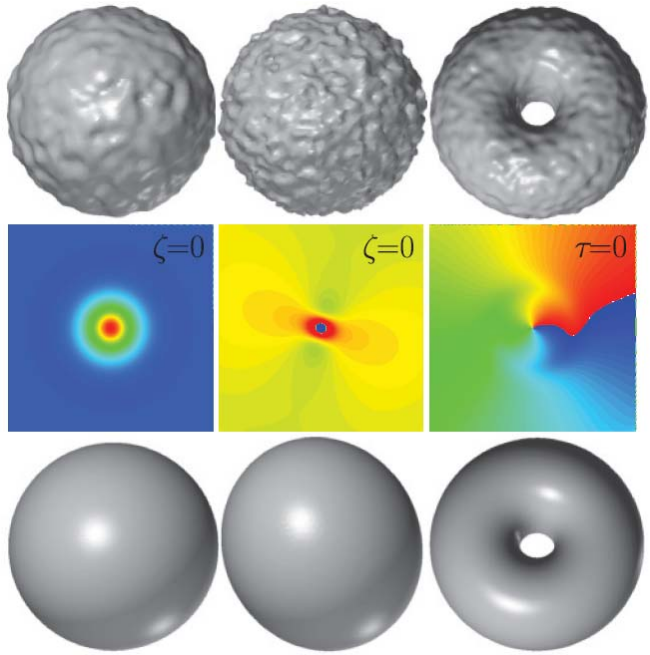


Figure 6.3. Isosurface plots showing intensity distributions at $\xi = 0$ (top) and $\xi = 1000$ (bottom) and illustrating stable propagation of a fundamental light bullet at $p_i = 5.2$, $\gamma = 2.0$ (left), transformation of an initial spherically symmetric fundamental bullet into an asymmetric bullet at $p_i = 4.35$, $\gamma = 1.5$ (center), and stable propagation of a vortex light bullet with $m = 1$ at $p_i = 2.8$, $\gamma = 3.5$ (right). Output phase distributions are shown in the middle row. In all cases the noise was added to input field distributions.

Although the entire family of asymmetric solitons may be constructed by varying gain $p_i$, the stability domain for such states is usually very narrow and it is located near the upper border of the stability domain for symmetric solitons. It should be stressed that stable fundamental light bullets can be also constructed when the dispersion parameter $\beta \neq 1$. Such bullets always feature ellipsoid-like intensity distributions.

Next we address gain landscapes having ring-like spatial shapes and Gaussian temporal profiles, i.e., $p = p_i \exp\left[-\left(\sqrt{\eta^2+\zeta^2}-\rho_r\right)^2 \Big/ \rho_w^2\right]\exp\left(-\tau^2/t^2\right)$, where $\rho_w$ and $\rho_r$ are the width and radius of the amplifying ring, respectively, and $t$ characterizes gain duration. Here we use the values $\rho_r = 3.75$, $\rho_w = 1.5$, $t = 2.0$, but the reported results remain similar for other parameters of gain profile. We search the profiles of three-dimensional vortex light bullets in the form $q = w\left(\eta, \zeta, \tau\right)\exp\left(im\varphi\right)\exp\left(ib\xi\right)$, where $\varphi$ is the azimuthal angle in the plane $\left(\eta, \zeta\right)$, and $m$ is the topological charge. Since stable vortex light bullets are attractors of Eq. (6.1), their shapes can be obtained by direct propagation for large distances, $\xi \sim 10^4$, using as an input, say, $q\big|_{\xi=0} = \left(\eta^2+\zeta^2\right)^{|m|/2}\exp\left(-\eta^2-\zeta^2+im\varphi\right)\exp\left(-\tau^2\right)$. Under proper conditions, such pulses experience fast reshaping, emit radiation, and asymptotically approach stationary vortex states. This means that spatially localized gain acting in combination with two-photon absorption suppresses not only supercritical collapse in three-dimensional case in cubic medium, but also azimuthal modulation instabilities that are destructive for vortices in the majority of focusing materials. Notice that the method of obtaining of stationary field distributions described above guarantees the robustness of the output states and shows that they can be excited from different input conditions, as they are attractors of the system. The stability of all obtained solutions is tested by adding input noise. The intensity distribution of the vortex light bullets looks like a torus [see Fig. 6.3(left) that illustrates stable propagation of such bullets in the presence of perturbations]. We generated stable light bullets with topological charges $m = 1$ and $m = 2$. Typical spatial field modulus and phase distributions in such states are shown in Fig. 6.4. The spatial radius of the resulting vortex bullets is always close to the radius of the amplifying ring, although the field of the light bullet may penetrate considerably into domains with losses at low $p_i$ values.

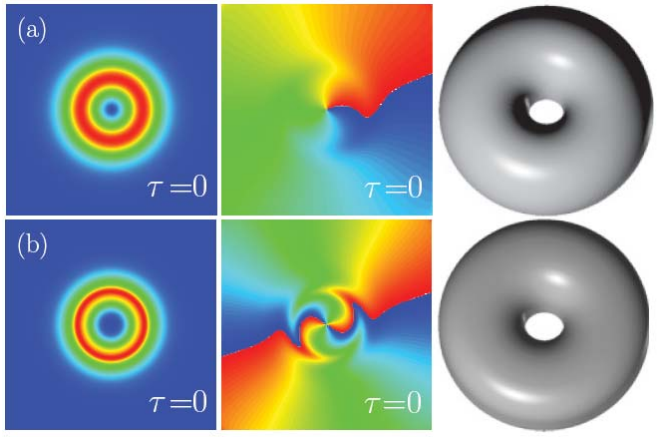


Figure 6.4. Field modulus (left) and phase (center) distributions at $\tau = 0$ as well as isosurface intensity plots (right) for stable vortex light bullets at (a) $m = 1$, $p_i = 2.8$, $\gamma = 3.5$ and (b) $m = 2$, $p_i = 8.0$, $\gamma = 3.0$.

The existence domains of vortex light bullets were obtained by slowly varying the gain parameter for each particular level of nonlinear losses. Therefore the obtained domains correspond to the parameter range in which vortex bullets are stable (thus they may be narrower than the total existence domains for such solitons). It was found that for moderate two-photon absorption, stable vortex bullets exist for a limited interval of gain parameters $p_i^{low} < p_i < p_i^{upp}$ [Fig. 6.2(b)]. The domain of stability monotonically expands with $\gamma$ and both $p_i^{low}$ and $p_i^{upp}$ grow with $\gamma$. Above the upper border of the stability domain, vortex light bullets transform into steadily pulsating breather-like structures. At the same time, for sufficiently large values of nonlinear losses, the upper border of the stability domain was not detected and light bullets remain stable even at very high gain levels. When nonlinear losses are too small ($\gamma < 1$) we did not find stable states at all.

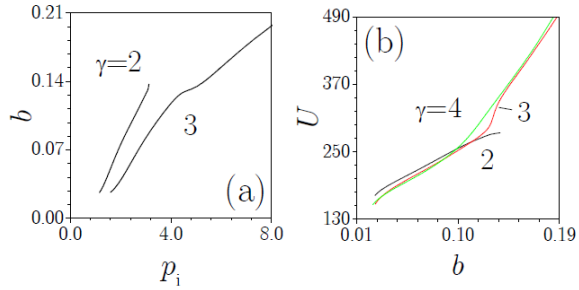


Figure 6.5. Propagation constant of a vortex light bullet versus gain parameter $p_i$ (a) and energy of a light bullet versus propagation constant (b).

The dependencies of the propagation constant of the vortex light bullet on the gain parameter and its energy on the propagation constant are shown in Figs. 6.5(a) and 6.5(b), respectively. Both $U\left(b\right)$ and $b\left(p_i\right)$ are monotonically growing functions. Notice the difference in $U\left(b\right)$ and $b\left(p_i\right)$ dependencies for solitons that feature an upper stability border (e.g., at $\gamma = 2$) and solitons that are stable even for high $p_i$ values (e.g., at $\gamma = 3$). It should be mentioned that vortex solitons with higher topological charge require considerably higher gain levels for their stabilization. Thus at $\gamma = 3$ the stable vortex bullet with $m = 1$ can be obtained already at $p_i^{low} \approx 1.6$, while the vortex bullet with $m = 2$ requires for its stabilization the gain level $p_i^{low} \approx 7.3$.

### *6.2. Spatial Splitting of Dislocations in Topological Light Bullets*

Until now we have considered vortex light bullets featuring only one phase dislocation with topological charge $m$. However, as in the two-dimensional case, the spatial deformation of gain landscape may cause a splitting of phase dislocations in light bullets. In order to illustrate this we again employ Eq. (6.1), but assume that the gain landscape has elliptical spatial and Gaussian temporal shapes, $p = p_i \exp\left(-\left(\sqrt{\left(\varepsilon\eta\right)^2 + \zeta^2} - \rho_r\right)^2 \Big/ \rho_w^2\right)\exp\left(-\tau^2/t^2\right)$, where $\rho_r = 3.75$, $\rho_w = 1.5$, $t = 2.0$, and the parameter $\varepsilon$ describes the ellipticity of gain ring in space. Vortex light bullets in such medium were excited with input wave packets $q\big|_{\xi=0} = q_0\left(\left(\varepsilon\eta\right)^2 + \zeta^2\right)^{|m|/2}\exp\left(-\left(\varepsilon\eta\right)^2 - \zeta^2 + im\varphi\right)\exp\left(-\tau^2\right)$ for various values of the ellipticity parameter $\varepsilon$. Here we consider only light bullets with topological charges $m = 2$ since solitons with higher topological charges require considerably higher gain levels for their stabilization.

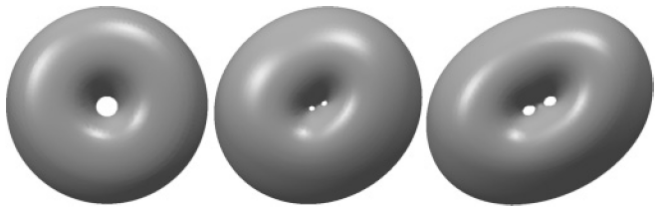

Figure 6.6. Isosurface plots showing the field modulus distribution in vortex light bullets with two phase dislocations for (left) $\varepsilon = 1$, (center) $\varepsilon = 0.85$, (right) $\varepsilon = 0.7$. In all cases $p_i = 9$, $\gamma = 3.5$.

Figure 6.6 illustrates the gradual deformation of the output shape of initially ring-like vortex light bullet upon increase of the ellipticity of the gain landscape. The progressive expansion of the vortex shape and separation of dislocations occurring in the direction of the stretching of the gain landscape are clearly visible. However, we found that too strong stretching of the gain profile results in the destabilization of a vortex bullet. Thus, for the parameters considered here, stable vortex bullets with separated dislocations were obtained only for $0.6 < \varepsilon < 1.0$.

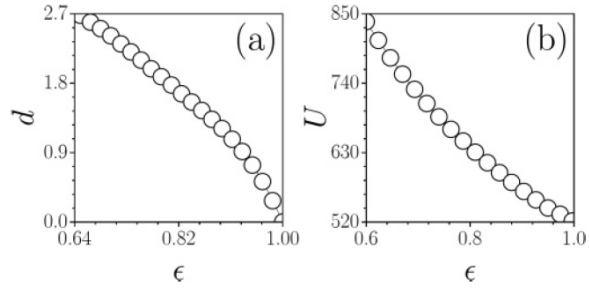


Figure 6.7. (a) The separation between outermost phase dislocations for a vortex light bullet with $m = 2$ versus $\varepsilon$ and (b) the energy of such bullets versus $\varepsilon$ at $\gamma = 3.5$ and $p_i = 9$.

A typical dependence of the separation between dislocations $d$ on the ellipticity parameter is shown in Fig. 6.7(a). The separation $d$ monotonically decreases with increase of $\varepsilon$ and approaches zero when $\varepsilon \to 1$ for a radially symmetric gain landscape. The total energy of a vortex light bullet $U$ as well as its propagation constant $b$ are the monotonically decreasing functions of the ellipticity parameter $\varepsilon$ [Fig. 6.7(b)].

### *6.3. Summary*

In this Chapter we illustrated that the competition between spatially and temporarily localized gain and uniform two-photon absorption in cubic nonlinear media may result in suppression of spherical collapse and azimuthal modulation instabilities, and therefore in the formation of stable fully three-dimensional light bullets. Depending on the gain profile, one may excite fundamental light bullets or vortex tori carrying nonzero topological charge. Moreover, modification of the spatial gain shape from ring-like to the elliptical one leads to the transformation of vortex light bullets with single dislocation into states with multiple spatially separated single-charged dislocations.

The main results summarized in this chapter have been published in the following journals:

1. V.E. Lobanov, **O.V. Borovkova**, Y.V. Kartashov, V.A. Vysloukh, and L. Torner, “Topological light bullets supported by spatiotemporal gain,” Phys. Rev. A **85**, 023804 (2012).
2. **O.V. Borovkova**, V.E. Lobanov, Y.V. Kartashov, and L. Torner, “Stable vortex-soliton tori with multiple nested phase singularities in dissipative media,” Phys. Rev. A **85**, 023814 (2012).

# Chapter 7. Quasi-Nondiffracting Linear Light Bullets

While nonlinearity is required for the rigorous existence of self-sustained solitary-wave structures localized in both space and time and carrying finite energy, it is well-known that stationary wave packet propagation may occur even in linear media if the wave packet belongs to the class of so-called nondiffracting fields, which always carry unlimited energy. Nevertheless, such wave packets may possess localized features in their intensity distributions (as it happens with very well known nondiffracting Bessel beam having localized central lobe) and, what is even more important, such field distributions diffract very slowly if they are truncated. In this sense, in practice, such nondiffracting wavepackets with localized features may be considered as the linear light bullets. The types of possible nondiffracting beams depend crucially on their dimensionality. For example, in two-dimensional geometries, nondiffracting patterns can be constructed in the coordinate systems where the Helmholtz equation is separable, yielding solutions invariant upon propagation, such as plane waves in Cartesian coordinates, Bessel beams in circular cylindrical coordinates [154], Mathieu beams in elliptic cylindrical coordinates [155], and parabolic beams in parabolic cylindrical coordinates [156]. Direct engineering of the spatial spectrum allows construction of more sophisticated spatial patterns [157].

Especially interesting for practical applications is the generation of fully three-dimensional nonspreading linear wave packets [158-163]. Such wave packets for normal and anomalous dispersion regimes have been studied in Refs. [164-166]. Recently, the formation of 3D Airy-Bessel wave packets was demonstrated experimentally [167] and beams featuring Airy shapes in three dimensions were generated [168]. The term linear light bullet was used for wave packets of this type, by analogy with their more elusive self-sustained counterparts

that exist in suitable nonlinear media [42, 49]. Nonspreading 3D wave packets may be important in diverse applications where the propagation of a focused beam of short pulsed light over a significant depth of focus is critical (e.g., in nanolithography and nanosurgery). Some of these applications may require sculptured complex spatial patterns beyond the known polychromatic combinations of Bessel beams.

In this Chapter we present an approach for generation of complex fully three-dimensional wave packets with various shapes. The method is based on the engineering of the spatiotemporal spectrum of the beam, and it allows generation of quasi-nondiffracting (i.e., very slowly diffracting) field distributions that have no analogs among the solutions known to date. They propagate undistorted over considerable distances, far more than those required in most practical applications.

### *7.1. Method of Construction of Quasi-Nondiffracting Linear Light Bullets*

We describe the propagation of a 3D linear wave packet in a uniform medium with anomalous group velocity dispersion by the linear Schrödinger equation (Eq. (1.8) with omitted nonlinear term) for the dimensionless light field amplitude $q$:

$$i\frac{\partial q}{\partial \xi} = -\frac{1}{2}\left(\frac{\partial^2 q}{\partial \eta^2} + \frac{\partial^2 q}{\partial \zeta^2} + \frac{\partial^2 q}{\partial \tau^2}\right). \tag{7.1}$$

The profile of any nonspreading wave packet that satisfies Eq. (7.1) and that propagates parallel to the $\xi$-axis can be presented in terms of the Whittaker integral [154-157], generalized to the case of three dimensions:

$$\begin{aligned} &q_s = \exp\left(-ik_t^2\xi/2\right)\cdot \\ &\cdot\int_0^{\pi} d\theta \int_0^{2\pi} G\left(\theta,\varphi\right)\exp\left[ik_t\left(\eta\cos\varphi\sin\theta + \zeta\sin\varphi\sin\theta + \tau\cos\theta\right)\right]d\varphi, \end{aligned} \tag{7.2}$$

where $k_t = \left(k_\eta^2 + k_\zeta^2 + k_\tau^2\right)^{1/2}$ is the transverse wavenumber, $\varphi$, $\theta$ are the azimuthal and polar angles in the frequency space, respectively, and $G\left(\theta,\varphi\right)$ is the angular spectrum. The Fourier transform $q_k$ of the field $q_s$ shows that the angular spectrum $G\left(\theta,\varphi\right)$ of a rigorously nonspreading wave packet is localized on the surface of a sphere of radius $k_t$. Physically, this means that only plane waves having equal transverse wavenumbers $k_t$ (hence, equal phase shifts accumulated upon propagation) may be involved into the formation of a nonspreading wave packet. The wavenumber $k_t$ determines the characteristic transverse scale of the wave packet.

Integral Eq. (7.2) is the key ingredient for the construction of quasi-nonspreading wave packets. Broadening the angular spectrum, i.e., using spectral components with different transverse wavenumbers $k_t$ belonging to the finite spherical layer of width $\delta k_t$, dramatically enriches the shapes of the beams that can be generated. Naturally, such broadening causes wave packets to spread slowly. However, the spreading remains slow as long as $\delta k_t \ll k_t$. In order to construct quasi-nonspreading wave packets, we used an iterative procedure that starts by selecting the desired field distribution $q_s\left(\eta, \zeta, \tau\right)$ at $\xi = 0$ and calculating its Fourier spectrum $q_k\left(k_\eta, k_\zeta, k_\tau\right)$. Then, the spectrum is modified by setting to zero the amplitudes of spectral components $q_k$ with $\left(k_\eta^2 + k_\zeta^2 + k_\tau^2\right)^{1/2}$ values outside a finite spherical layer $\left[k_t - \delta k_t/2,\, k_t + \delta k_t/2\right]$. After the calculation of the inverse Fourier transform, one keeps new phase distribution $\arg\left[q_s\left(\eta, \zeta, \tau\right)\right]$, but replaces the field modulus with the initial desired field modulus distribution. The iterative procedure is repeated until the convergence in phase is achieved [157].

### *7.2. Examples of Quasi-Nondiffracting Linear Light Bullets*

The essence of this method is illustrated in Fig. 7.1, where we show wave packets constructed with different widths of the angular spectrum using as a trial function a localized Gaussian distribution (further we use $k_t = 1$). For large relative widths of the spectrum $\delta = \delta k_t / k_t$, the resulting shape reproduces almost any trial function because multiple spectral components are involved in its formation (see right column in Fig. 7.1 where $\delta \sim 0.5$ and the convergence toward a Gaussian distribution is apparent). However, such a wave packet quickly spreads upon propagation due to the accumulated dephasing of spectral components. Decreasing the spectral width results in the appearance of multiple rings around the bright central core (Fig. 7.1, left column). These rings ensure nonspreading propagation by providing the transverse energy flow from the wave packet periphery to its center. In the limit $\delta \to 0$, the method produces exact nonspreading wave packets $q_s = \left[\sin\left(k_t\rho\right)/\rho\right]\exp\left(-ik_t^2\xi/2\right)$, where $\rho = \left(\eta^2 + \zeta^2 + \tau^2\right)^{1/2}$.

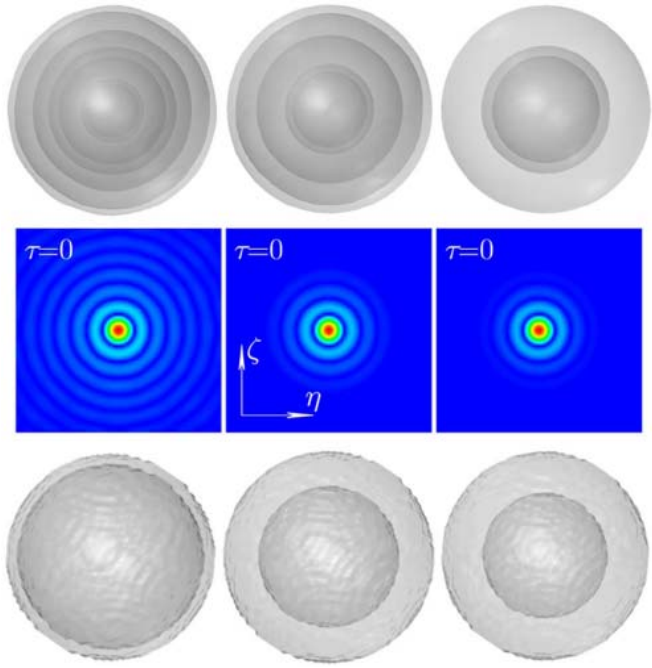


Figure 7.1. Isosurface plots at the level $0.08 \cdot \max\left|q_s\right|$ showing 3D field modulus distribution (top row), field modulus distribution in the plane $\tau = 0$ (middle row), and corresponding spectra at the level $0.4 \max\left|q_k\right|$ (bottom row) of 3D wave packets generated at $\delta = 0.1$ (left column), 0.4 (middle column), and 0.5 (right column). All isosurface plots are made partially transparent to show internal structure of the wave packet and its spectrum.

The impact of the width of the angular spectrum on the rate of beam spreading in the course of propagation is illustrated in Fig. 7.2(a). Here we defined $L$ as a propagation distance at which the peak amplitude of the beam decreases by $10\%$. When $\delta \to 0$, $L$ diverges, and when $\delta \sim 1$ (i.e., at $\delta k_t \sim k_t$), the distance $L$ approaches the spreading length for the trial beam. Note that even for $\delta \sim 0.2$ the spreading length for the iterated wave packets is sufficiently large what allows to consider them as nonspreading for most practical purposes. The broader the spectrum, the richer the possible quasi-nonspreading patterns. Since exact nonspreading wave packets carry an infinite energy, the fraction of power carried by the central bright spot decreases as $\delta \to 0$ [Fig. 7.2(b)].

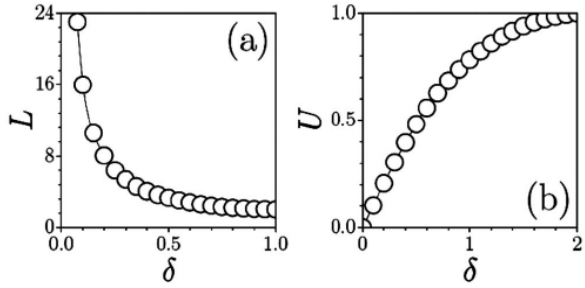


Figure 7.2. (a) Propagation distance at which peak amplitude of the wave packet from Fig. 7.1 decreases by 10% versus angular spectrum width. (b) Fraction of energy concentrated in the central bright spot versus angular spectrum width.

The method described above allows formation of quasi-nonspreading wave packets featuring radially symmetric or azimuthally modulated spatial distributions at any $\tau$ value and pronounced localization in time. For example, Fig. 7.3 (left column) shows a sequence of two wave packets separated by a certain time interval and having Bessel-like spatial distributions. The finite width of the angular spectrum allows us to achieve a situation when temporal localization of each wave packet is more pronounced than its spatial localization, as one can see from the cross section at $\eta = 0$. The spectrum of such a wave packet resembles a finite-width ring wrapped around a sphere. One can generate 3D wave packets with spatial shapes corresponding to any known 2D nondiffracting beam, such as a Bessel, Mathieu, or parabolic beam. The temporal distributions of such wave packets consist of the central bright lobe surrounded by multiple decaying oscillations. Arbitrary sequences of separated or overlapping in $\tau$ Bessel, Mathieu, or parabolic wave packets can be generated, too.

A specific necklacelike wave packet that at each point of time resembles a higher-order azimuthally modulated Bessel beam is shown in Fig. 7.3 (central column). Such a wave packet is characterized by more localized field modulus distribution in the $\tau = 0$ plane than the azimuthally modulated Bessel beam. The spectrum of this beam is azimuthally modulated. The number of nodes in the spectrum corresponds to the number of azimuthal nodes in the spatial distributions. One can generate wave packets localized in time with sophisticated spatial profiles, such as necklacelike wave packets shown in Fig. 7.3 (right column) that exhibit different numbers of azimuthal nodes at $\eta < 0$ and $\eta > 0$ at any time moment $\tau$.

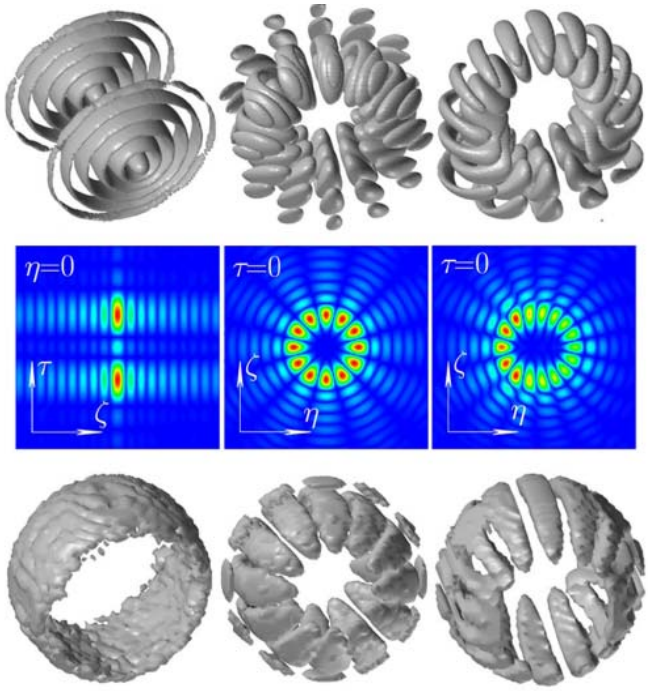


Figure 7.3. Left, field modulus distribution at the level $0.19\max\left|q_s\right|$ (top row), field modulus distribution at $\eta = 0$ (middle row), and beam spectrum at the level $0.02\max\left|q_k\right|$ (bottom row) for a wave packet composed of two Bessel-like pulsed beams. Center, field modulus distribution at the level $0.19\max\left|q_s\right|$ (top row), field modulus distribution at $\tau = 0$ (middle row), and spectrum at the level $0.14\max\left|q_k\right|$ (bottom row) for a necklacelike wave packet. Right, field modulus distribution at the level $0.17\max\left|q_s\right|$ (top row), field modulus distribution at $\tau = 0$ (middle row), and spectrum at $0.36\max\left|q_k\right|$ (bottom row) for a necklace wave packet with complex spatial distribution.

Distributions that have no analogs among 3D patterns known to date are illustrated in Fig. 7.4. Such wave packets feature complex shapes and may change topology between different temporal and spatial cross sections. Examples include hollow 3D shapes (Fig. 7.4, left column) whose field modulus distribution in any cross section $\eta = 0$, $\zeta = 0$, or $\tau = 0$ resembles a ring surrounding the region with very small field intensity. The spectrum of such a beam is composed of several rings with gradually decreasing widths that wrap around the sphere. One can generate a sequence of wave packets that are well localized in space and whose centers may follow complex shapes in time. An example that exhibits spiraling in time is illustrated in Fig. 7.4 (central column).

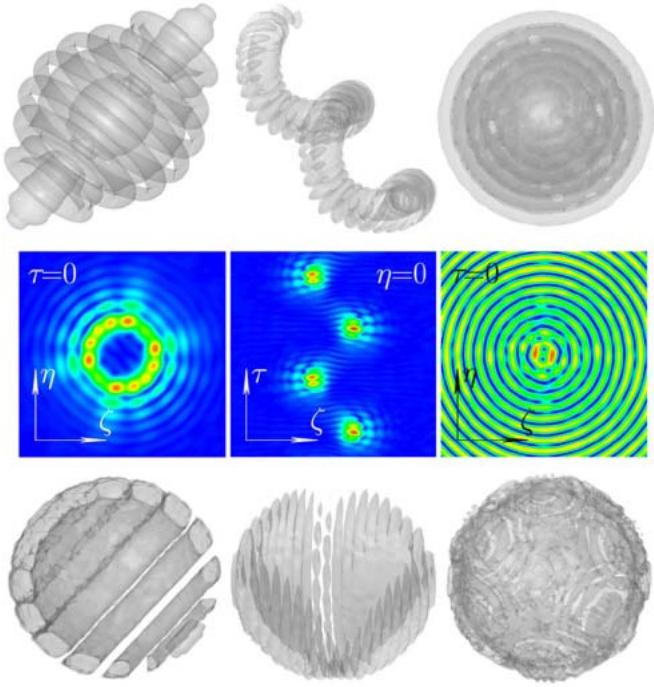


Figure 7.4. Left, field modulus distribution at the level $0.13\max\left|q_s\right|$ (top row), field modulus distribution at $\tau = 0$ (middle row), and beam spectrum at the level $0.02\max\left|q_k\right|$ (bottom row) for a 'hollow' wave packet. Center, field modulus distribution at the level $0.02\max\left|q_s\right|$ (top row), field modulus distribution at $\eta = 0$ (middle row), and spectrum at the level $0.05\max\left|q_k\right|$ (bottom row) for a spiraling wave packet. Right, field modulus distribution at the level $0.2\max\left|q_s\right|$ (top row), field modulus distribution at $\tau = 0$ (middle row), and spectrum at $0.16\max\left|q_k\right|$ (bottom row) for a spherically periodic wave packet (only several central rings are shown).

Finally, a specific spherically periodic wave packet is shown in Fig. 7.4 (right column). Such a wave packet shows remarkable field periodicity at the periphery, while the field amplitude does not decrease at $\rho \to \infty$, as it happens in truly nondiffracting spherically symmetric beam with $q_s \sim \sin\left(k_t\rho\right)\big/\rho$.

### *7.3. Summary*

In this Chapter we touched upon an approach for generation of a variety of quasi-nonspreading wave patterns, beyond the known nondiffracting solutions of Helmholtz equation describing light propagation in a medium with anomalous group velocity dispersion. Such quasi-nonspreading patterns may be tailored to

meet the requirements of each particular application. Potential applications where such sculptured pulsed beams may be crucial are anticipated in areas where tight focus, large depth of focus, and high peak power are required.

The main results summarized in this chapter have been published in the following journals:

1. **O.V. Borovkova**, Y.V. Kartashov, V.E. Lobanov, V.A. Vysloukh, and L. Torner, “General quasi-nonspreading linear three-dimensional wave packets,” Opt. Lett. **36**, 2176-2178 (2011).

# Conclusion

The subjects of this PhD Thesis are the properties, dynamics, and stability of various kinds of conservative and dissipative solitons in complex engineered materials. Such materials are constructed in order to obtain desired properties, unattainable in natural optical media. They can support stable solitons in settings in which these solitons do not even exist in the natural materials. We consider the media with shallow modulations of the linear refractive index, nonlinearity coefficient, losses, and amplification.

It was found that in conservative systems, nonlinear lattice composed of alternating domains with cubic and saturable nonlinearities can support stable scalar two-dimensional solitons that would be unstable in uniform cubic media. While solitons centered on the cubic domains are stable, their counterparts centered on saturable regions are unstable and exhibit reshaping upon propagation. We found that linear or nonlinear lattices affecting only one of two components of the vector soliton may stabilize the entire complex state. The impact of the linear lattice is reasonably strong, and the vector soliton may even be stable if it includes a weak lattice component. However, the nonlinear lattice affecting one component only ensures soliton stabilization when the norm of the component feeling the lattice is comparable to or greater than the norm of the other component, for which the medium is uniform.

Complex engineered materials may support new types of soliton that are impossible in natural media. Thus, bright solitons may form in the medium with purely defocusing nonlinearity if its strength grows rapidly enough from the center to the periphery of the material. Fundamental solitons, higher-order modes, and vortex rings have been demonstrated in the materials with the exponential law of increase in the defocusing nonlinearity. In power-law defocusing nonlinearity landscapes, stable bright two-dimensional fundamental and vortex solitons and one-dimensional multipoles could be generated. Moreover, stable two-

dimensional bright and vortex solitons exist in hexagonal photonic crystal fibers in which the core material is linear or focusing, while voids are filled with a defocusing material whose nonlinearity grows towards the photonic crystal periphery.

In dissipative settings the inhomogeneous gain and absorption landscapes support new types of dissipative soliton. First of all, one-dimensional fundamental and multipole solitons in nonlinear dissipative materials were considered. We showed that even in medium with uniform linear gain, stable solitons may be supported by spatially inhomogeneous nonlinear absorption growth towards the periphery of the sample. Single-well absorption landscapes support the family of completely stable fundamental solitons in defocusing medium, while in focusing medium solitons may experience spontaneous symmetry breaking, manifested in the formation of asymmetric stable soliton branches. Stable dipoles could be generated in the setting with a double-well absorption landscape and focusing nonlinearity. In this case, symmetry breaking was encountered in defocusing medium. Linear losses combined with a localized cubic gain in the cubic-quintic nonlinear medium supports the family of fundamental spatial solitons pinned to the localized nonlinear gain spot.

Ring-shaped gain landscapes support stable two-dimensional vortex solitons in the medium with focusing cubic nonlinearity and two-photon absorption. Such gain landscapes not only support stationary, but also rotating vortex solitons with azimuthally modulated shapes, despite the fact that all the parameters of the system are either spatially uniform or radially symmetric. The transformation of the initial ring-like gain profile into an elliptical one leads to the transformation of the single multi-charge vortex into a state with several charge-1 dislocations nested inside a common vortex core. The separation between dislocations is mainly dictated by the geometry of the gain landscape. Finally, complex amplifying landscapes constructed of several gain rings support a variety of stable multi-vortex solitons, with the simplest of them being vortex twins and anti-twins, which may have symmetric or asymmetric shapes.

Stable fully three-dimensional light bullets have been demonstrated in dissipative media with uniform two-photon absorption and gain localized in both space and time. In such materials fundamental light bullets or vortex tori carrying nonzero topological charge can exist. The modification of the spatial gain shape from ring-like to elliptical leads to the transformation of vortex light bullets with single dislocation into states with multiple spatially separated single-charged dislocations.

We proposed a new method of generation of quasi-nonspreading three-dimensional wave patterns that remain virtually unchanged upon propagation of several tens of diffraction lengths. Such quasi-nonspreading patterns may be tailored to meet the requirements of each particular application, where tight focus, large depth of focus, and high peak power of the light beam are required.

Thus, this PhD Thesis presents a variety of new types of soliton, ranging from the simplest one-dimensional fundamental states to fully three-dimensional light bullets and vortex tori, in both conservative and dissipative complex engineered materials possessing unique properties that are inaccessible in natural media. The novel types of soliton explored in this PhD Thesis in the field of optics may appear in other areas of nonlinear science.

# Bibliography


1. J.S. Russell, "Report on waves", Report of the 14th Meeting of the British Association for the Advancement of Science, York, 311 (September, 1844).
2. D.J. Korteweg, and G. de Vries, "On the change of form of long waves advancing in a rectangular canal, and on a new type of long stationary waves," Philosophical Magazine **39**, 422 (1895).
3. N.J. Zabusky, and M.D. Kruskal, "Interaction of 'solitons' in a collisionless plasma and the recurrence of initial states," Phys. Rev. Lett. **15**, 240 (1965).
4. Y.S. Kivshar, and G.P. Agrawal, "Optical solitons: from fibers to photonic crystals," Academic Press, London (2003).
5. J.R. Taylor, ed., "Optical solitons: theory and experiment," New York: Cambridge University Press (1992).
6. N.N. Akhmediev, A. Ankiewicz, eds., "Solitons: nonlinear pulses and beams," London: Chapman and Hall (1997).
7. N.N. Akhmediev, A. Ankiewicz, eds., "Dissipative solitons: from optics to biology and medicine," Vol. **751** of Lecture Notes in Physics, Springer (2008).
8. R.W. Boyd, "Nonlinear optics," San Diego: Academic Press (2008).
9. J.E. Bjorkholm, and A.A. Ashkin, "cw Self-focusing and self-trapping of light in sodium vapor," Phys. Rev. Lett. **32**, 129 (1974).
10. T.K. Gustafson, P.L. Kelley, R.Y. Chiao, R.G. Brewer, "Self-trapping in media with saturation of the nonlinear index," Appl. Phys. Lett. **12**, 165 (1968).
11. J.H. Marburger, and E. Dawes, "Dynamical formation of a small-scale filament," Phys. Rev. Lett. **21**, 556 (1968).
12. G.I.A. Stegeman, D.N. Christodoulides, and M. Segev, "Optical spatial solitons: historical perspectives," IEEE J. Quantum Electron. **6**, 1419 (2000).
13. G.P. Agrawal, "Nonlinear fiber optics," San Diego: Academic Press (2006).
14. B.A. Malomed, D. Mihalache, F. Wise, and L. Torner, "Spatiotemporal optical solitons," J. Opt. B **7**, R53 (2005).

15. F. Wise, and P. Di Trapani, “Spatiotemporal solitons,” Opt. Photonics News **13**, 28 (2002).
16. A.S. Desyatnikov, D. Neshev, E.A. Ostrovskaya, Y.S. Kivshar, G. McCarthy, W. Krolikowski, and B. Luther-Davies, “Multipole composite spatial solitons: theory and experiment,” J. Opt. Soc. Am. B **19**, 586 (2002).
17. A.S. Desyatnikov, Y.S. Kivshar, and L. Torner, “Optical vortices and vortex solitons,” Progress in Optics **47**, 291 (2005).
18. S.V. Manakov, “On the theory of two-dimensional stationary self-focusing of electromagnetic waves,” Sov. Phys. JETP **38**, 248 (1974).
19. A. Hasegawa, and F. Tappert, “Transmission of stationary nonlinear optical pulses in dispersive dielectric fibers. I. Anomalous dispersion,” Appl. Phys. Lett. **23**, 142 (1973).
20. L.F. Mollenauer, R.H. Stolen, and J.P. Gordon, “Experimental observation of picosecond pulse narrowing and solitons in optical fibers,” Phys. Rev. Lett. **45**, 1095 (1980).
21. A. Hasegawa, “Amplification and reshaping of optical solitons in a glass fiber-IV: Use of the stimulated Raman process,” Opt. Lett. **8**, 650 (1983).
22. L.F. Mollenauer, R.H. Stolen, and M.N. Islam, “Experimental demonstration of soliton propagation in long fibers: loss compensated by Raman gain,” Opt. Lett. **10**, 229 (1985).
23. L.F. Mollenauer, and K. Smith, “Demonstration of soliton transmission over more than 4000 km in fiber with loss periodically compensated by Raman gain,” Opt. Lett. **13**, 675 (1988).
24. G.A. Askar’yan, “Effects of the gradient of a strong electromagnetic beam on electrons and atoms,” Sov. Phys. JETP **15**, 1088 (1962).
25. R.Y. Chiao, E. Garmire, and C.H. Townes, “Self-trapping of optical beams,” Phys. Rev. Lett. **13**, 479 (1964).
26. V.I. Talanov, “Propagation of a short electromagnetic pulse in an active medium,” Radio Phys. **7**, 254 (1964).
27. P.L. Kelley, “Self-focusing of optical beams,” Phys. Rev. Lett. **15**, 1005 (1965).
28. L. Berge, “Wave collapse in physics: principles and applications to light and plasma waves,” Phys. Rep. **303**, 259 (1998).
29. V.E. Zakharov, and A.M. Rubenchik, “Instability of waveguides and solitons in nonlinear media,” Sov. Phys. JETP **38**, 494 (1974).
30. M. Karlsson, “Optical beams in saturable self-focusing media,” Phys. Rev. A **46**, 2726 (1992).
31. M. Mitchell, Z. Chen, M. Shih, and M. Segev, “Self-trapping of partially spatially incoherent light,” Phys. Rev. Lett. **77**, 490 (1996).
32. M. Shih, P. Leach, M. Segev, M.H. Garret, G. Salamo, and G.C. Valley, “Two-dimensional steady-state photorefractive screening solitons,” Opt. Lett. **21**, 324 (1996).
33. J.M. Soto-Crespo, D.R. Heatley, E.M. Wright, and N.N. Akhmediev, “Stability of the higher-bound states in a saturable self-focusing medium,” Phys. Rev. A **44**, 636-644 (1991).

34. J. Yang, “Internal oscillations and instability characteristics of (2+1)-dimensional solitons in a saturable nonlinear medium,” Phys. Rev. E **66**, 026601 (2002).
35. M. Quiroga-Teixeiro, and H. Michinel, “Stable azimuthal stationary state in quintic nonlinear optical media,” J. Opt. Soc. Am. B **14**, 2004 (1997).
36. A.I. Yakimenko, Y.A. Zaliznyak, and Y. Kivshar, “Stable vortex solitons in nonlocal self-focusing nonlinear media,” Phys. Rev. E **71**, 065603(R) (2005).
37. J.U. Kang, G.I. Stegeman, J.S. Aitchison, and N. Akhmediev, “Observation of Manakov spatial solitons in AlGaAs planar waveguides,” Phys. Rev. Lett. **76**, 3699 (1996).
38. Z.H. Musslimani, M. Segev, D.N. Christodoulides, and M. Soljacic, “Composite multihump vector solitons carrying topological charge,” Phys. Rev. Lett. **84**, 1164 (2000).
39. O. Cohen, T. Schwartz, J.W. Fleischer, M. Segev, and D.N. Christodoulides, “Multiband vector lattice solitons,” Phys. Rev. Lett. **91**, 113901 (2003).
40. A.A. Sukhorukov, and Y.S. Kivshar, “Multigap discrete vector solitons,” Phys. Rev. Lett. **91**, 113902 (2003).
41. Y.V. Kartashov, A.S. Zelenina, V.A. Vysloukh, and L. Torner, “Stabilization of vector solitons in optical lattices,” Phys. Rev. E **70**, 066623 (2004).
42. Y. Silberberg, “Collapse of optical pulses,” Opt. Lett. **15**, 1282 (1990).
43. H.S. Eisenberg, R. Morandotti, Y. Silberberg, S. Bar-Ad, D. Ross, and J.S. Aitchison, “Kerr spatiotemporal self-focusing in a planar glass waveguide,” Phys. Rev. Lett. **87**, 043902 (2001).
44. A.B. Blagoeva, S.G. Dinev, A.A. Dreischuh, and A. Naidenov, “Light bullets formation in a bulk media,” IEEE J. Quantum Electron. **27**, 2060 (1991).
45. S.K. Turitsyn, “Spatial dispersion of nonlinearity and stability of multidimensional solitons,” Theoretical and Mathematical Physics **64**, 797 (1985).
46. G. Fibich, B. Ilan, and G. Papanicolaou, “Self-focusing with fourth-order dispersion,” SIAM J. Appl. Math. **62**, 1437 (2002).
47. N.N. Akhmediev, A. Ankiewicz, and J.M. Soto-Crespo, “Does the nonlinear Schrödinger equation correctly describe beam propagation?” Opt. Lett. **18**, 411 (1993).
48. L.-C. Crasovan, J.P. Torres, D. Mihalache, and L. Torner “Arresting wave collapse by wave self-rectification,” Phys. Rev. Lett. **91**, 063904 (2003).
49. S. Minardi, F. Eilenberger, Y.V. Kartashov, A. Szameit, U. Röpke, J. Kobelke, K. Schuster, H. Bartelt, S. Nolte, L. Torner, F. Lederer, A. Tünnermann, and T. Pertsch, “Three-dimensional light bullets in arrays of waveguides,” Phys. Rev. Lett. **105**, 263901 (2010).
50. N.N. Rosanov, “Spatial Hysteresis and Optical Patterns,” Berlin, Springer (2002).
51. N.R. Pereira, and L. Stenflo, “Nonlinear Schrodinger equation including growth and damping,” Phys. Fluids **20**, 1733 (1977).

52. W. van Saarloos, and P.C. Hohenberg, “Pulses and fronts in the complex Ginzburg-Landau equation near a subcritical bifurcation,” Phys. Rev. Lett. **64**, 749 (1990).
53. N.N. Akhmediev, V.V. Afanasjev, “Novel arbitrary-amplitude soliton solutions of the cubic-quintic complex Ginzburg-Landau equation,” Phys. Rev. Lett. **75**, 2320 (1995).
54. H. Sakaguchi, and B.A. Malomed, “Two-dimensional solitary pulses in driven diffractive-diffusive complex Ginzburg-Landau equation,” Physica D **167**, 123 (2002).
55. L.-C. Crasovan, B.A. Malomed, and D. Mihalache, “Stable vortex solitons in the two-dimensional Ginzburg-Landau equation,” Phys. Rev. E **63**, 016605 (2000).
56. J.M. Soto-Crespo, N. Akhmediev, C. Mejia-Cortes, and N. Devine, “Dissipative ring solitons with vorticity,” Opt. Express **17**, 4236 (2009).
57. N.A. Kaliteevskii, N.N. Rosanov, and S.V. Fedorov, “Formation of laser bullets,” Opt. Spectrosc. **85**, 485 (1998).
58. N.A. Veretenov, A.G. Vladimirov, N.A. Kaliteevskii, N.N. Rozanov, S.V. Fedorov, and A.N. Shatsev, “Conditions for the existence of laser bullets,” Opt. Spectrosc. **89**, 380 (2000).
59. J.M. Soto-Crespo, Ph. Grelu, and N. Akhmediev, “Optical bullets and ‘rockets’ in nonlinear dissipative systems and their transformations and interactions,” Opt. Express **14**, 4013 (2006).
60. V. Sharka, and N.B. Aleksic, “Stability criterion for dissipative soliton solutions of the one-, two-, and three-dimensional complex cubic-quintic Ginzburg-Landau equations,” Phys. Rev. Lett. **96**, 013903 (2006).
61. D. Mihalache, D. Mazilu, F. Lederer, H. Leblond, and B.A. Malomed, “Stability of dissipative optical solitons in the three-dimensional cubic-quintic Ginzburg-Landau equation,” Phys. Rev. A **75**, 033811 (2007).
62. D. Mihalache, D. Mazilu, F. Lederer, H. Leblond, and B.A. Malomed, “Collisions between coaxial vortex solitons in the three-dimensional cubic-quintic complex Ginzburg-Landau equation,” Phys. Rev. A **77**, 033817 (2008).
63. D. Mihalache, D. Mazilu, F. Lederer, Y.V. Kartashov, L.-C. Crasovan, L. Torner, and B.A. Malomed, “Stable vortex tori in the three-dimensional cubic-quintic Ginzburg-Landau equation,” Phys. Rev. Lett. **97**, 073904 (2006).
64. D. Mihalache, D. Mazilu, F. Lederer, H. Leblond, and B.A. Malomed, “Stability limits for three-dimensional vortex solitons in the Ginzburg-Landau equation with the cubic-quintic nonlinearity,” Phys. Rev. A **76**, 045803 (2007).
65. D. Mihalache, D. Mazilu, F. Lederer, H. Leblond, and B.A. Malomed, “Spatiotemporal solitons in the Ginzburg-Landau model with a two-dimensional transverse grating,” Phys. Rev. A **81**, 025801 (2010).
66. S. Barland, J.R. Tredicce, M. Brambilla, L.A. Lugiato, S. Balle, M. Giudici, T. Maggipinto, L. Spinelli, G. Tissoni, T. Knödl, M. Miller, and R. Jäger, “Cavity solitons as pixels in semiconductor microcavities,” Nature **419**, 699 (2002).

67. E.A. Ultanir, G.I. Stegeman, D. Michaelis, Ch.H. Lange, and F. Lederer, “Stable dissipative solitons in semiconductor optical amplifiers,” Phys. Rev. Lett. **90**, 253903 (2003).
68. J. Atai, and B.A. Malomed, “Stability and interactions of solitons in two-component active systems,” Phys. Rev. E **54**, 4371 (1996).
69. P.V. Paulau, D. Gomila, P. Colet, N.A. Loiko, N.N. Rosanov, T. Ackemann, and W.J. Firth, “Vortex solitons in lasers with feedback,” Opt. Express **18**, 8859 (2010).
70. F.Kh. Abdullaev, V.V. Konotop, M. Salerno, and A.V. Yulin, “Dissipative periodic waves, solitons, and breathers of the nonlinear Schrödinger equation with complex potentials,” Phys. Rev. E **82**, 056606 (2010).
71. Y.V. Kartashov, V.V. Konotop, and V.A. Vysloukh, “Dissipative surface solitons in periodic structures,” EPL **91**, 34003 (2010).
72. D.A. Zezyulin, Y.V. Kartashov, and V.V. Konotop, “Solitons in a medium with linear dissipation and localized gain,” Opt. Lett. **36**, 1200 (2011).
73. Y.V. Kartashov, V.V. Konotop, and V.A. Vysloukh, “Symmetry breaking and multipeaked solitons in inhomogeneous gain landscapes,” Phys. Rev. A **83**, 041806(R) (2011).
74. C.H. Tsang, B.A. Malomed, and K.W. Chow, “Multistable dissipative structures pinned to dual hot spots,” Phys. Rev. E **84**, 066609 (2011).
75. V.E. Lobanov, Y.V. Kartashov, V.A. Vysloukh, and L. Torner, “Stable radially symmetric and azimuthally modulated vortex solitons supported by localized gain,” Opt. Lett. **36**, 85 (2011).
76. N.N. Rosanov, S.V. Fedorov, and A.N. Shatsev, “Curvilinear motion of multivortex laser-soliton complexes with strong and weak coupling,” Phys. Rev. Lett. **95**, 053903 (2005).
77. E. Caboche, F. Pedaci, P. Genevet, S. Barland, M. Giudici, J. Tredicce, G. Tissoni, and L.A. Lugiato, “Microresonator defects as sources of drifting cavity solitons,” Phys. Rev. Lett. **102**, 163901 (2009).
78. Y. V. Kartashov, V.V. Konotop, V. A. Vysloukh, and L. Torner, “Dissipative defect modes in periodic structures,” Opt. Lett. **35**, 1638 (2010).
79. Y. V. Kartashov, V.V. Konotop, V. A. Vysloukh, and L. Torner, “Vortex lattice solitons supported by localized gain,” Opt. Lett. **35**, 3177 (2010).
80. E. Yablonovitch, “Inhibited spontaneous emission in solid-state physics and electronics,” Phys. Rev. Lett. **58**, 2059 (1987).
81. S. John, “Strong localization of photons in certain disordered dielectric superlattices,” Phys. Rev. Lett. **58**, 2486 (1987).
82. K. Sakoda, “Optical properties of photonic crystals,” Berlin: Springer (2004).
83. J.D. Joannoupoulos, S.G. Johnson, J.N. Winn, and R.D. Meade, “Photonic crystals: molding the flow of light,” Princeton University Press, Princeton (2008).
84. A. Mekis, J.C. Chen, I. Kurland, Sh. Fan, P.R. Villeneuve, and J.D. Joannopoulos, “High transmission through sharp bends in photonic crystal waveguides,” Phys. Rev. Lett. **77**, 3787 (1996).

85. C. Jin, B. Cheng, B. Man, Z. Li, D. Zhang, S. Ban, and B. Sun, “Band gap and wave guiding effect in a quasiperiodic photonic crystal,” Appl. Phys. Lett. **75**, 1848 (1999).
86. S.F. Mingaleev, Y.S. Kivshar, and R.A. Sammut, “Long-range interaction and nonlinear localized modes in photonic crystal waveguides,” Phys. Rev. E **62**, 5777 (2000).
87. F. Lederer, and Y. Silberberg, “Discrete solitons,” Opt. Photon. News **13**, 49 (2002).
88. J.W. Fleischer, M. Segev, N.K. Efremidis, and D.N. Christodoulides, “Observation of two-dimensional discrete solitons in optically induced nonlinear photonic lattices,” Nature **422**, 147 (2003).
89. A. Fratalocchi, G. Assanto, K.A. Brzdakiewicz, and M.A. Karpierz, “All-optical switching and beam steering in tunable waveguide arrays,” Appl. Phys. Lett. **86**, 051112 (2005).
90. B.A. Malomed, “Soliton management in periodic systems,” Springer, New York (2006).
91. F. Lederer, G. I. Stegeman, D. N. Christodoulides, G. Assanto, M. Segev, and Y. Silberberg, “Discrete solitons in optics,” Phys. Rep. **463**, 1 (2008).
92. Y.V. Kartashov, V.A. Vysloukh, and L. Torner, “Soliton shape and mobility control in optical lattices,” Prog. Opt. **52**, 63 (2009).
93. T. Pertsch, U. Peschel, F. Lederer, J. Burghoff, M. Will, S. Nolte, and A. Tünnermann, “Discrete diffraction in two-dimensional arrays of coupled waveguides in silica,” Opt. Lett. **29**, 468 (2004).
94. A. Szameit, D. Blömer, J. Burghoff, T. Schreiber, T. Pertsch, S. Nolte, and A. Tünnermann, “Discrete nonlinear localization in femtosecond laser written waveguides in fused silica,” Opt. Express **13**, 10552 (2005).
95. F. Chen, M. Stepic, C.E. Rüter, D. Runde, D. Kip, V. Shandarov, O. Manela, and M. Segev, “Discrete diffraction and spatial gap solitons in photovoltaic $LiNbO_3$ waveguide arrays,” Opt. Express **13**, 4314 (2005).
96. H.S. Eisenberg, Y. Silberberg, R. Morandotti, A.R. Boyd, and J.S. Aitchison, “Discrete spatial optical solitons in waveguide arrays,” Phys. Rev. Lett. **81**, 3383 (1998).
97. N.K. Efremidis, S. Sears, D.N. Christodoulides, J.W. Fleischer, and M. Segev, “Discrete solitons in photorefractive optically induced photonic lattices,” Phys. Rev. E **66**, 046602 (2002).
98. J.W. Fleischer, T. Carmon, M. Segev, N.K. Efremidis, and D.N. Christodoulides, “Observation of Discrete Solitons in Optically Induced Real Time Waveguide Arrays,” Phys. Rev. Lett. **90**, 023902 (2003).
99. J. Yang and Z.H. Musslimani, “Fundamental and vortex solitons in a two-dimensional optical lattice,” Opt. Lett. **28**, 2094 (2003).
100. B.B. Baizakov, B.A. Malomed, and M. Salerno, “Multidimensional solitons in periodic potentials,” EPL **63**, 642 (2003).

101. H. Martin, E.D. Eugenieva, Z. Chen, and D.N. Christodoulides, “Discrete solitons and soliton-induced dislocations in partially coherent photonic lattices,” Phys. Rev. Lett. **92**, 123902 (2004).
102. D.N. Neshev, T.J. Alexander, E.A. Ostrovskaya, Y.S. Kivshar, H. Martin, I. Makasyuk, and Z. Chen, “Observation of discrete vortex solitons in optically induced photonic lattices,” Phys. Rev. Lett. **92**, 123903 (2004).
103. J.W. Fleischer, G. Bartal, O. Cohen, O. Manela, M. Segev, J. Hudock, and D.N. Christodoulides, “Observation of vortex-ring ‘discrete’ solitons in 2D photonic lattices,” Phys. Rev. Lett. **92**, 123904 (2004).
104. Y.V. Kartashov, A.A. Egorov, L. Torner, and D.N. Christodoulides, “Stable soliton complexes in two-dimensional photonic lattices,” Opt. Lett. **29**, 1918 (2004).
105. R. Fischer, D. Träger, D.N. Neshev, A.A. Sukhorukov, W. Krolikowski, C. Denz, and Y.S. Kivshar, “Reduced-symmetry two-dimensional solitons in photonic lattices,” Phys. Rev. Lett. **96**, 023905 (2006).
106. H. Sakaguchi, and B.A. Malomed, “Matter-wave solitons in nonlinear optical lattices,” Phys. Rev. E **72**, 046610 (2005).
107. Y. Sivan, G. Fibich, and M.I. Weinstein, “Waves in nonlinear lattices: Ultra short optical pulses and Bose-Einstein condensates,” Phys. Rev. Lett. **97**, 193902 (2006).
108. G. Fibich, Y. Sivan, and M.I. Weinstein, “Bound states of nonlinear Schrödinger equations with a periodic nonlinear microstructure,” Physica D **217**, 31 (2006).
109. D.L. Machacek, E.A. Foreman, Q.E. Hoq, P.G. Kevrekidis, A. Saxena, D.J. Frantzeskakis, and A.R. Bishop, “Statics and dynamics of an inhomogeneously nonlinear lattice,” Phys. Rev. E **74**, 036602 (2006).
110. F.Kh. Abdullaev, A. Gammal, M. Salerno, and L. Tomio, “Localized modes of binary mixtures of Bose-Einstein condensates in nonlinear optical lattices,” Phys. Lett. A **77**, 023615 (2008).
111. Y.V. Kartashov, V.A. Vysloukh, and L. Torner, “Soliton modes, stability, and drift in optical lattices with spatially modulated nonlinearity,” Opt. Lett. **33**, 1747 (2008).
112. Y.V. Kartashov, V.A. Vysloukh, and L. Torner, “Power-dependent shaping of vortex solitons in optical lattices with spatially modulated nonlinear refractive index,” Opt. Lett. **33**, 2173 (2008).
113. Y.V. Kartashov, B.A. Malomed, V.A. Vysloukh, and L. Torner, “Two-dimensional solitons in nonlinear lattices,” Opt. Lett. **34**, 770 (2009).
114. N.V. Hung, P. Zin, M. Trippenbach, and B.A. Malomed, “Two-dimensional solitons in media with stripe-shaped nonlinearity modulation,” Phys. Rev. E **82**, 046602 (2010).
115. Y.V. Kartashov, B.A. Malomed, and L. Torner, “Solitons in nonlinear lattices,” Rev. Mod. Phys. **83**, 247 (2011).

116. H. Sakaguchi, and B.A. Malomed, “Two-dimensional solitons in the Gross-Pitaevskii equation with spatially modulated nonlinearity,” Phys. Rev. E **73**, 026601 (2006).
117. P.St.J. Russell, “Photonic crystal fibers,” Science **299**, 358 (2003).
118. A.S. Cerqueira, “Recent progress and novel applications of photonic crystal fibers,” Rep. Prog. Phys. **73**, 024401 (2010).
119. Y. Kominis, and K. Hizanidis, “Power dependent soliton location and stability in complex photonic structures,” Opt. Express **16**, 12124 (2008).
120. H. Sakaguchi, and B.A. Malomed, “Solitons in combined linear and nonlinear lattice potentials,” Phys. Rev. A **81**, 013624 (2010).
121. D.E. Pelinovsky, A.A. Sukhorukov, and Y.S. Kivshar, “Bifurcation and stability of gap solitons in periodic potentials,” Phys. Rev. E **70**, 036618 (2004).
122. H. Saito, and M. Ueda, “Dynamically stabilized bright solitons in a two-dimensional Bose-Einstein condensate,” Phys. Rev. Lett. **90**, 040403 (2003).
123. V.M. Perez-Garcia, and R. Pardo, “Localization phenomena in nonlinear Schrödinger equations with spatially inhomogeneous nonlinearities: theory and applications to Bose-Einstein condensates,” Physica D: Nonlinear Phenomena **238**, 1352 (2009).
124. I. Towers, and B.A. Malomed, “Stable (2+1)-dimensional solitons in a layered medium with sign-alternating Kerr nonlinearity,” J. Opt. Soc. Am. B **19**, 537 (2002).
125. M. Centurion, M.A. Porter, P.G. Kevrekidis, and D. Psaltis, “Nonlinearity management in optics: experiment, theory and simulation,” Phys. Rev. Lett. **97**, 033903 (2006).
126. J. Hudock, P.G. Kevrekidis, B.A. Malomed, and D.N. Christodoulides, “Discrete vector solitons in two-dimensional nonlinear waveguide arrays: Solutions, stability, and dynamics,” Phys. Rev. E **67**, 056618 (2003).
127. Z. Chen, A. Bezryadina, I. Makasyuk, J. Yang, “Observation of two-dimensional lattice vector solitons,” Opt. Lett. **29**, 1656 (2004).
128. Y.V. Kartashov, B.A. Malomed, V.A. Vysloukh, and L. Torner, “Vector solitons in nonlinear lattices,” Opt. Lett. **34**, 3625 (2009).
129. V.A. Brazhnyi, and V.V. Konotop, “Theory of nonlinear matter waves in optical lattices,” Mod. Phys. Lett. B **18**, 627 (2004).
130. J. Hukriede, D. Runde, and D. Kip, “Fabrication and application of holographic Bragg gratings in lithium niobate channel waveguides,” J. Physics D **36**, R1 (2003).
131. K.E. Strecker, G.B. Partridge, A.G. Truscott, and R. G. Hulet, “Bright matter wave solitons in Bose-Einstein condensates,” New J. Phys. **5**, 73 (2003).
132. A. Alexandrescu, and V.M. Perez-Garcia, “Matter-wave solitons supported by dissipation,” Phys. Rev. A **73**, 053610 (2006).
133. M. Vieweg, T. Gissibl, S. Pricking, B.T. Kuhlmey, D.C. Wu, B.J. Eggleton, and H. Giessen, “Ultrafast nonlinear optofluidies in selectively liquid-filled photonic crystal fibers,” Opt. Express **18**, 25232 (2010).

134. T. Gissibl, M. Vieweg, M.M. Vogel, M. Aboud Ahmed, T. Graf, and H. Giessen, “Preparation and characterization of a large mode area liquid-filled photonic crystal fiber: transition from isolated to coupled spatial modes,” Appl. Phys. B **106**, 521 (2012).
135. A. Smerzi, S. Fantoni, S. Giovanazzi, and S.R. Shenoy, “Quantum coherent atomic tunneling between two trapped Bose-Einstein condensates,” Phys. Rev. Lett. **79**, 4950 (1997).
136. M. Albiez, R. Gati, J. Fölling, S. Hunsmann, M. Cristiani, and M.K. Oberhalter, “Direct observation of tunneling and nonlinear self-trapping in a single bosonic Josephson junction,” Phys. Rev. Lett. **95**, 010402 (2005).
137. A. Sigler, and B.A. Malomed, “Solitary pulses in linearly coupled cubic-quintic Ginzburg-Landau equation,” Physica D **212**, 305 (2005).
138. S. Kim, J. Jin, Y.-J. Kim, I.-Y. Park, Y. Kim, and S.-W. Kim, “High-harmonic generation by resonant plasmon field enhancement,” Nature **453**, 757 (2008).
139. M. Matsumoto, A. Hasegawa, Y. Kodama, “Adiabatic amplification of solitons by means of nonlinear amplifying loop mirrors,” Opt. Lett. **19**, 1019 (1994).
140. I. Gabitov, D.D. Holm, B.P. Luce, and A. Mattheus, “Recovery of solitons with nonlinear amplifying loop mirrors,” Opt. Lett. **20**, 2490 (1995).
141. S. Burtsev, D.J. Kaup, and B.A. Malomed, “Optimum reshaping of an optical soliton by a nonlinear amplifier,” J. Opt. Soc. Am. B **13**, 888 (1996).
142. Kh.I. Pushkarov, D.I. Pushkarov, and I.V. Tomov, “Self-action of light beams in nonlinear media: soliton solutions,” Opt. Quantum Electron. **11**, 471 (1979).
143. F. Ye, Y.V. Kartashov, B. Hu, and L. Torner, “Twin-vortex solitons in nonlocal nonlinear media,” Opt. Lett. **35**, 628 (2010).
144. T.J. Alexander, A.S. Desyatnikov, and Y.S. Kivshar, “Multivortex solitons in triangular photonic lattices,” Opt. Lett. **32**, 1293 (2007).
145. O. Katz, Y. Lahini, and Y. Silberberg, “Multiple breakup of high-order spatial solitons,” Opt. Lett. **33**, 2830 (2008).
146. M.J. Connelly, “Semiconductor optical amplifiers,” Dordrecht: Kluwer Academic Publishers (2002).
147. A.S. Desyatnikov, A.A. Sukhorukov, and Y.S. Kivshar, “Azimuthons: spatially modulated vortex solitons,” Phys. Rev. Lett. **95**, 203904 (2005).
148. D.S. Sumida, R.W. Byren, and M. Ushinsky, US Patent No. 2011/0281387 A1 (17 Nov. 2011).
149. A.B. Aceves, C. De Angelis, A.M. Rubenchik, and S.K. Turitsyn, “Multidimensional solitons in fiber arrays,” Opt. Lett. **19**, 329 (1994).
150. D. Mihalache, D. Mazilu, F. Lederer, Y.V. Kartashov, L.-C. Crasovan, and L. Torner, “Stable three-dimensional spatiotemporal solitons in a two-dimensional photonic lattices,” Phys. Rev. E **70**, 055603(R) (2004).

151. D. Mihalache, D. Mazilu, F. Lederer, and Y.S. Kivshar, “Spatiotemporal surface solitons in two-dimensional photonic lattices,” Opt. Lett. **32**, 3173 (2007).
152. Y.J. He, B.A. Malomed, D. Mihalache, B. Liu, H.C. Huang, H. Yang, and H.Z. Wang, “Bound states of the one-, two-, and three-dimensional solitons in complex Ginzburg-Landau equations with a linear potential,” Opt. Lett. **34**, 2976 (2009).
153. J.A. Fülöp, and J. Hebling, “Applications of tilted-pulse-front excitation” in “Recent optical and photonic technologies,” edited by K.Y. Kim INTECH, Croatia (2010).
154. J. Durnin, J.J. Miceli, and J.H. Eberly, “Diffraction-free beams,” Phys. Rev. Lett. **58**, 1499 (1987).
155. J.C. Gutierrez-Vega, M.D. Iturbe-Castillo, G.A. Ramirez, E. Tepichin, R.M. Rodriguez-Dagnino, S. Chavez-Cerda, and G.H.C. New, “Experimental observation of optical Mathieu beams,” Opt. Commun. **195**, 35 (2001).
156. C. Lopez-Mariscal, M.A. Bandres, J.C. Gutierrez-Vega, and S. Chavez-Cerda, “Observation of parabolic nondiffracting optical fields,” Opt. Express **13**, 2364 (2005).
157. S. Lopez-Aguayo, Y.V. Kartashov, V.A. Vysloukh, and L. Torner, “Method to generate complex quasinondiffracting optical lattices,” Phys. Rev. Lett. **105**, 013902 (2010).
158. A.T. Friberg, J. Fagerholm, and M.M. Salomaa, “Space-frequency analysis of nondiffracting pulses,” Opt. Commun. **136**, 207 (1997).
159. M.A. Porras, “Diffraction-free and dispersion-free pulsed beam propagation in dispersive media,” Opt. Lett. **26**, 1364 (2001).
160. S. Longhi, “Spatial-temporal Gauss-Laguerre waves in dispersive media,” Phys. Rev. E **68**, 066612 (2003).
161. M.A. Porras, G.Valiulis, and P. Di Trapani, “Unified description of Bessel X waves with cone dispersion and tilted pulses,” Phys. Rev. E **68**, 016613 (2003).
162. S. Longhi, “Localized subluminal envelope pulses in dispersive media,” Opt. Lett. **29**, 147 (2004).
163. M.A. Porras, and P. Di Trapani, “Localized and stationary light wave modes in dispersive media,” Phys. Rev. E **69**, 066606 (2004).
164. H. Sonajalg, M. Ratsep, and P. Saari, “Demonstration of the Bessel-X pulse propagating with strong lateral and longitudinal localization in a dispersive medium,” Opt. Lett. **22**, 310 (1997).
165. P. Saari, and K. Reivelt, “Evidence of X-shaped propagation-invariant localized light waves,” Phys. Rev. Lett. **79**, 4135 (1997).
166. M. Dallaire, N. McCarthy, and M. Piche, “Spatiotemporal Bessel beams: theory and experiments,” Opt. Express **17**, 18148 (2009).
167. A. Chong, W.H. Renninger, D.N. Christodoulides, and F.W. Wise, “Airy-Bessel wave packets as versatile linear light bullets,” Nature Photonics **4**, 103 (2010).

168. D. Abdollahpour, S. Suntsov, D.G. Papazoglou, and S. Tzortzakis, “Spatiotemporal Airy light bullets in the linear and nonlinear regimes,” Phys. Rev. Lett. **105**, 253901 (2010).

# List of Figures

Figure 2.2. Profiles of solitons centered on (a) cubic and (b) saturable domains. Gray regions indicate saturable domains, while white regions indicate cubic domains. (c) $U$ versus $b$ for solitons residing on cubic domain (curve 1) and on saturable domain (curve 2). (d) $\delta_{\mathrm{r}}$ versus $b$ for solitons centered on saturable domain. In all cases $\rho_{\mathrm{c}}=1$, $\rho_{\mathrm{s}}=1$.

Figure 2.3. Profiles of solitons centered on (a) cubic domain when $\rho_{\mathrm{c}}=1.5$, $\rho_{\mathrm{s}}=1.0$ and (b) saturable domains when $\rho_{\mathrm{c}}=1.0$, $\rho_{\mathrm{s}}=2.0$.

Figure 2.4. (a) $U$ versus $b$ for solitons centered on domain with saturable nonlinearity at $\rho_{\mathrm{s}}=1.5$ (curve 1), $2.0$ (curve 2), and $2.5$ (curve 3). (b) $\delta_{\mathrm{r}}$ versus $b$ for solitons centered on domain with saturable nonlinearity at $\rho_{\mathrm{s}}=1.5$ (curve 1), $2.5$ (curve 2). In (a) and (b) $\rho_{\mathrm{c}}=1.0$. (c) $U$ versus $b$ for solitons centered on domain with cubic nonlinearity at $\rho_{\mathrm{c}}=1.0$ (curve 1) and $1.5$ (curve 2). Circles in (c) separate stable and unstable branches. (d) $\delta_{\mathrm{r}}$ versus $b$ for solitons centered on domain with cubic nonlinearity at $\rho_{\mathrm{s}}=1.5$. In (c) and (d) $\rho_{\mathrm{s}}=1.0$.

Figure 2.5. (a) Decay of solitons centered on saturable domain at $b=2.0$, $\rho_{\mathrm{c}}=1.0$, $\rho_{\mathrm{s}}=2.0$, and (b) stable propagation of soliton centered on cubic domain at $b=2.0$, $\rho_{\mathrm{c}}=1.5$, $\rho_{\mathrm{s}}=1.0$. Field modulus distributions are shown at different distances.

Figure 2.6. Field distributions $w_{1,2}(\eta)$ at $\zeta=0$ in 2D vector solitons with (a), (b) nonlinear and (c), (d) linear lattices acting on the first component only. In all cases, $C=2$, $b_1=3$ are fixed, while $b_2=1$ (a), 9 (b), 0.4 (c), and 2.5 (d). Solitons shown in panels (a), (c) are unstable, while solitons from panels (b), (d) are stable.

Figure 2.7. The total energy flow (a) and power sharing between the two components (b) versus $b_2$ at $b_1=3$ and $C=2$ for the vector soliton with the nonlinear lattice acting on the first component. Panels (c) and (d) show the same, but when the linear lattice acts in the first component. Points correspond to solitons shown in Fig. 2.6.

Figure 2.8. Domains of the stability (“s”) and instability (“u”) for vector solitons with (a) nonlinear and (b) linear lattice acting on the first component in the $(C,b_2)$-plane for $b_1=3$. In both cases the vector solitons exist

Figure 3.5. (a) Profiles of 2D solitons with different topological charges corresponding to $b=-10$, $\nu=5$. (b) Vortices with $m=1$ corresponding to $b=-5,-10,-20$ (curves 1, 2, 3). (c) 1D solitons with different numbers of nodes corresponding to $b=-10$, $\nu=5$. In each panel, the nonlinearity profile is shown by the red curve.

Figure 3.6. The energy flow versus the propagation constant, $b$, for 2D solitons at $\nu=5$ (a), and versus $\nu$ for 2D (b) and 1D (c) solitons at $b=-10$. Red curves in (b) and (c) show the prediction of the Thomas-Fermi approximation.

Figure 3.7. (a) The real part of the perturbation growth rate versus $b$ at $\nu=3.5,4,$ and 5 (curves 1, 2, and 3) for vortices with $m=1$ and perturbation index $n=1$. (b) The largest perturbation growth rate for the vortex with $m=1$ versus $\nu$.

Figure 3.8. (a) A decay of the unstable vortex with $m=1$, $b=-3$, $\nu=3.5$. (b) A decay of the unstable vortex with $m=2$, $b=-20$, $\nu=4$. (c) The stable propagation of vortex with $m=1$, $b=-30$, $\nu=5$ (left, center) and vortex with $m=2$, $b=-15$, $\nu=10$ (right). In all cases, the white noise was added to the input field distributions.

Figure 3.9. (a) The cross section of the photonic crystal fiber, where the core is shown by red and the filled strands are shown by blue. A distribution of the absolute value of the field for fundamental solitons with (b) $b=-1$ and (c) $b=-6$, (d) a dipole soliton with $b=-2$, (e) a quadrupole soliton with $b=-2$, and (f) vortex solitons with topological charge 1 and $b=-1$ or (h) $b=-4$. Panels (g) and (k) show the phase distributions for vortex solitons depicted in (f) and (h), respectively. In all cases $\sigma_c=0$.

Figure 3.10. (a) The energy flow of the fundamental solitons versus the propagation constant at $\sigma_c=0.2$ (curve 1), 0.5 (curve 2), and 1.0 (curve 3). (b, c) The lower cutoff and the corresponding energy flow $U_m=U\left(b=b^{low}\right)$ versus the nonlinearity of the host material. (d) The energy flow of the vortex solitons versus the propagation constant at $\sigma_c=0$ (curve 1) and $\sigma_c=1$ (curve 2).

Figure 3.11. (a) The stable propagation of the perturbed fundamental solitons with $b=-2$ and (b) the vortex soliton with $b=-1$, and (c) a decay of an unstable vortex with $b=-2$ into a stable fundamental soliton. The distributions of the absolute value of the field are shown at the different propagation distances. For the stable vortex soliton, the final phase distribution is also shown. In all cases $\sigma_c=0$.

Figure 4.1. Typical profiles of fundamental symmetric (a) and asymmetric (b) soltions in the focusing medium, and of the symmetric one in the defocusing medium (c) with the single-well nonlinear-absorption profile (4.3) [red curves for $\gamma\left(\eta\right)$], at $p_i = 1.5$, $\gamma_0 = 0.5$.

Figure 4.2. The energy flow (a) and propagation constant (b) versus $p_i$ for symmetric ("fs") and asymmetric ("fa") fundamental solitons in the focusing medium with the single-well nonlinear-absorption profile (4.3) at $\gamma_0 = 0.5$. (c), (d): The same for dipole solitons in the double-well nonlinear-absorption landscape (4.6) at $\gamma_0 = 2.0$. Subscripts "fs", "ds", and "da" denote symmetric dipoles in the focusing and defocusing media, and asymmetric dipoles in the defocusing medium, respectively. Circles in (a) and (b) correspond to the solitons in Figs. 4.1(a) and 4.1 (b), while circles in (c), (d) pertain to the solitons in Figs. 4.4 (a) and (b), respectively.

Figure 4.3. Existence and stability domains in the $\left(\gamma_0, p_i\right)$ plane. (a) The fundamental solitons in the focusing medium with the single-well nonlinear absorption profile (4.3) (the asymmetric solitons exist and are stable at $p_i > p_i^{cr1}$). (b) and (c): Dipole solitons in the double-well absorption profile (4.7), in the focusing and defocusing media, respectively.

Figure 4.4. Examples of symmetric and asymmetric dipole solitons at $p_i = 3.0$ (a) and $p_i = 1.9$ (b), respectively, in the defocusing medium with the double-well nonlinear-absorption landscape (4.5) [red curves for $\gamma\left(\eta\right)$], at $\gamma_0 = 2.0$.

Figure 4.5. The dynamics of dipole solitons in the focusing (a)-(c) and defocusing (d)-(f) media with the double-well nonlinear-loss profile (4.7). (a) Spontaneous transformation of an unstable symmetric dipole into a fundamental soliton at $p_i = 0.8$. (b) Stable propagation of the symmetric dipole at $p_i = 1.8$. (c) The transformation of an unstable symmetric dipole into breather at $p_i = 3.2$. (d, e) The stable propagation of the symmetric and asymmetric dipoles at $p_i = 1.5$ and $p_i = 2.1$, respectively. (f) Spontaneous transformation of an unstable asymmetric dipole into a breather, with the dynamically restored symmetry, at $p_i = 2.23$. All the cases are shown for $\gamma_0 = 3$, with small noise added to the input.

Figure 4.6. The soliton total power $U$ (top left), propagation constant $b$ (top right), and instability growth rates $\delta_r$ (bottom) vs gain coefficient $p$ at $\sigma_5 = 0.1$, $\gamma = 0.05$, $\rho_g = 0.1$. Here and in Fig. 4.7 below, the dashed line corresponds to the completely unstable lower branch, the bold segment represents the stable part of the upper branch, and its unstable continuation is depicted by the thin solid line. Analytical predictions (4.15) and (4.17) are shown by dotted curves (for the upper branch in the top right panel, the approximation amounts to $b = b_{co}$), and vertical dash-dotted lines mark the threshold point as predicted by Eq. (4.16).

Figure 4.7. The total power and propagation constant of the soliton vs the quintic coefficient, $\sigma_5$, at $p = 0.5$, $\gamma = 0.05$, $\rho_g = 0.1$. The horizontal dotted lines represent asymptotic values (4.17), which do not depend on $\sigma_5$.

Figure 4.8. (a) The evolution of a weakly unstable soliton, belonging to the upper branch, into a stable breather, at $\sigma_5 = 0.1$, $\gamma = 0.05$, $\rho_g = 0.1$ and $p = 0.105$. (b) The decay of the localized mode at a larger value of the cubic gain, $p = 0.25$.

Figure 4.9. Typical examples of the solitons, for $\sigma_5 = 0.1$, $\gamma = 0.05$, $\rho_g = 0.1$: (top left panel) a stable soliton belonging to the upper branch, at $p = 0.08$; (bottom left panel) a destabilized soliton from the same branch, at $p = 0.25$; (top right panel) an unstable soliton which belongs to the lower branch, at $p = 0.08$. The bottom right panel displays the attraction basin of the stable soliton excited by the Gaussian input (see text), the bold point showing parameters of the soliton fitted to the Gaussian shape.

Figure 4.10. Stability domains (between the borders) for the solitons at different values of the loss coefficient, $\gamma$, and fixed width of the gain distribution, $\rho_g = 0.1$ (left panel), and at different values of $\rho_g$ and fixed $\gamma = 0.1$ (right panel).

Figure 5.1. Field modulus (top) and phase distributions (bottom) for rotating vortex solitons having (a) one phase singularity at $p_i = 1.7$, (b) two singularities at $p_i = 2.0$, and (c) three singularities at $p_i = 2.8$. In all cases, $\gamma = 2.0$.

Figure 5.2. Dynamics of propagation for rotating vortex solitons having (a) one phase singularity at $p_i = 1.7$, (b) two singularities at $p_i = 2.0$, and

(c) three singularities at $p_i = 2.8$. In all cases, $\gamma = 2.0$, and white noise was added into the input fields.

Figure 5.3. Domains of existence of stable rotating vortex solitons with (a) two and (b) three singularities on the plane $\left(\gamma, p_i\right)$.

Figure 5.4. (a) Instantaneous propagation constant value defined in different points versus propagation distance for rotating vortex with one singularity at $p_i = 1.7$, $\gamma = 2.0$. (b) Energy flow versus $p_i$ for vortex solitons with two or three singularities at $\gamma = 2.0$. Points correspond to solitons shown in Figs. 5.1(b) and 5.1(c). (c) Period of rotation for vortex with three singularities versus $p_i$ at $\gamma = 2.0$. (d) Map of internal energy flows in vortex soliton from Fig. 5.1(c).

Figure 5.5. (top) Field modulus and (bottom) phase distributions for dissipative vortex solitons with two phase dislocations at (a) $\varepsilon = 0.9$, (b) $\varepsilon = 0.7$, and (c) $\varepsilon = 0.5$ and for solitons with three phase dislocations at (d) $\varepsilon = 0.9$, (e) $\varepsilon = 0.7$, and (f) $\varepsilon = 0.5$. In all cases $p_i = 7$ and $\gamma = 2.0$.

Figure 5.6. (a) The separation between outermost phase dislocations for vortex solitons with $m = 2$ and $3$ versus $\varepsilon$. The (b) energy flow and (c) propagation constant of a vortex soltion with $m = 2$ versus $\varepsilon$.

Figure 5.7. (top) Field modulus and (bottom) phase distributions in unconventional azimuthally modulated dissipative vortex solitons with four phase dislocations at (a) $\varepsilon = 0.9$, (b) $\varepsilon = 0.7$, and (c) $\varepsilon = 0.5$ In all cases $p_i = 7$ and $\gamma = 2.0$.

Figure 5.8. (a) Symmetric vortex-antivortex mode at $p_i = 3.7$. (b) Asymmetric vortex-antivortex soliton at $p_i = 5$. (c) Asymmetric vortex-vortex mode at $p_i = 4$. Top row: field modulus distribution, bottom row: phase distributions. In all cases $s = 1.5$.

Figure 5.9. (a) Energy flow of vortex-antivortex soliton versus $p_i$ at $s = 1.5$. (b) Energy flow of vortex-vortex and vortex-antivortex solitons versus $s$ at $p_i = 4$. The branches corresponding to symmetric solitons are shown black, while branches of asymmetric solitons are shown red. (c) Minimal gain required for existence of stable vortex-antivortex solitons versus $s$.

Figure 5.10. Multivortex solitons in gain landscapes with three (a), (b), and four (c) rings. In (a) $p_i = 3$, while in (b), (c) $p_i = 4$. Top row shows field

Figure 7.2. (a) Propagation distance at which peak amplitude of the wave packet from Fig. 7.1 decreases by 10% versus angular spectrum width. (b) Fraction of energy concentrated in the central bright spot versus angular spectrum width.

Figure 7.3. Left, field modulus distribution at the level $0.19\max\left|q_s\right|$ (top row), field modulus distribution at $\eta = 0$ (middle row), and beam spectrum at the level $0.02\max\left|q_k\right|$ (bottom row) for a wave packet composed of two Bessel-like pulsed beams. Center, field modulus distribution at the level $0.19\max\left|q_s\right|$ (top row), field modulus distribution at $\tau = 0$ (middle row), and spectrum at the level $0.14\max\left|q_k\right|$ (bottom row) for a necklacelike wave packet. Right, field modulus distribution at the level $0.17\max\left|q_s\right|$ (top row), field modulus distribution at $\tau = 0$ (middle row), and spectrum at $0.36\max\left|q_k\right|$ (bottom row) for a necklace wave packet with complex spatial distribution.

Figure 7.4. Left, field modulus distribution at the level $0.13\max\left|q_s\right|$ (top row), field modulus distribution at $\tau = 0$ (middle row), and beam spectrum at the level $0.02\max\left|q_k\right|$ (bottom row) for a 'hollow' wave packet. Center, field modulus distribution at the level $0.02\max\left|q_s\right|$ (top row), field modulus distribution at $\eta = 0$ (middle row), and spectrum at the level $0.05\max\left|q_k\right|$ (bottom row) for a spiraling wave packet. Right, field modulus distribution at the level $0.2\max\left|q_s\right|$ (top row), field modulus distribution at $\tau = 0$ (middle row), and spectrum at $0.16\max\left|q_k\right|$ (bottom row) for a spherically periodic wave packet (only several central rings are shown).